A DEVELOPMENT OF A DAMAGE MONITORING SYSTEM USING AN EMBEDDED FIBER BRAGG GRATING SENSORS

MOHD HAFIZI BIN ZOHARI

CHE KU EDDY NIZWAN BIN CHE KU HUSIN

MOHD FAIRUSHAM BIN GHAZALI

DAING MOHAMAD NAFIZ BIN DAING IDRIS

MOHD SHAHRIR BIN MOHD SANI

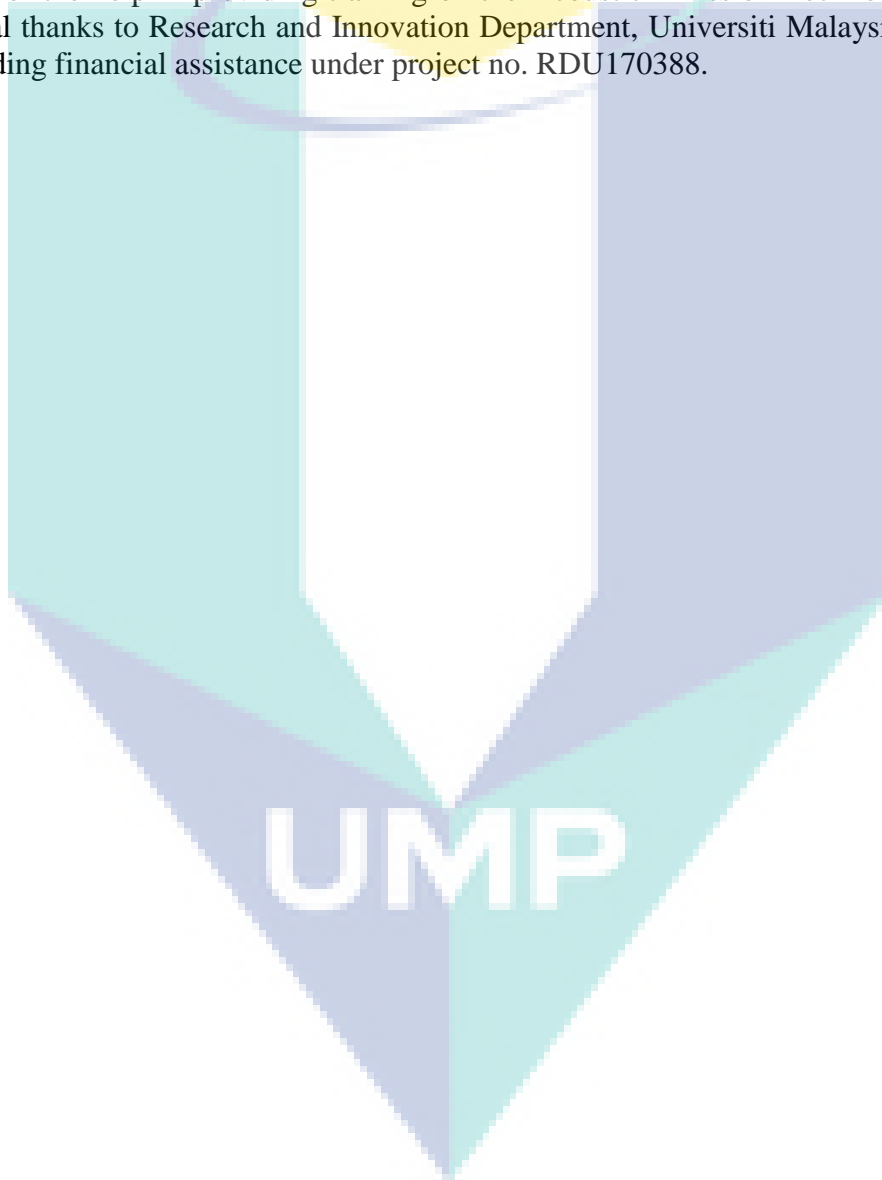**RESEARCH VOTE NO:**

RDU170388

Faculty of Mechanical Engineering

Universiti Malaysia Pahang

2019

ACKNOWLEDGEMENTS

A DEVELOPMENT OF A DAMAGE MONITORING SYSTEM USING AN EMBEDDED FIBER BRAGG GRATING SENSORS

(Keywords: Fibre Bragg grating, structural health monitoring, real-time monitoring)

Glass-fibre reinforced polymer (GFRP) composite materials certainly have the undeniable favour over conventional metallic materials, notably in light weight to high strength ratio. However, these composite materials are prone to sudden catastrophic damage that requires the structural health monitoring (SHM). FBG sensor has shown a great potential in embedding and integrating with the composite materials, performing real-time monitoring of the structural condition. However, the main problems of FBG are the drawbacks in static and dynamic strain sensing monitoring assessment. Error in desired readings due to variations in output voltage and spectrum illustration for static strain interpretation are the drawbacks in static strain sensing. On the other hand, due to the presence of noise in the signal spectrum, the inaccuracy estimation of time of arrival (TOA) through peak detection are the drawback in dynamic strain sensing. Thus, the designation of this research study is to improve the current FBG based real-time monitoring system.

Two specimens of composite plate and composite beam have been fabricated based on hand lay-up lamination method. FBG sensors are embedded in both the structures. For improvement in static strain measurement, the mesh-grid function utilized is capable of meshing the shapes of a structure, and display the deflection of the structure. The voltage normalization algorithm has reduced the output voltage variations from 26 data/minute to 17 data/minute with the elimination of pre-calibration each time before use. For the improvement in dynamic strain sensing, the merging of cross-correlation approach with linear source location technique (CC-LSL) has estimated the impact location close to the actual hit location with the largest relative error at only 2.47 %. From the conclusion of the study, it is truly believed that with this reputable sensing system, it is is one step closer to achieving the key concept of smart structure.

Key researchers: MOHD HAFIZI BIN ZOHARI
CHE KU EDDY NIZWAN BIN CHE KU HUSIN
MOHD FAIRUSHAM BIN GHAZALI
DAING MOHAMAD NAFIZ BIN DAING IDRIS
MOHD SHAHRIR BIN MOHD SANI

Email.   : hafizi@ump.edu.my
Tel. No.   : 0179860752
Vote No. : RDU170388

A DEVELOPMENT OF A DAMAGE MONITORING SYSTEM USING AN EMBEDDED FIBER BRAGG GRATING SENSORS

(Keywords: Fibre Bragg grating, structural health monitoring, real-time monitoring)

Gentian kaca polimer (GFRP) adalah sejenis bahan komposit yang memiliki nisbah kekuatan yang tinggi terhadap keseluruhan berat berbanding dengan bahan logam konvensional. Namun begitu, bahan komposit ini mudah terdedah kepada kerosakan yang mana memerlukan pemantauan keadaan struktur objek tersebut. Penderiaan FBG mempunyai potensi yang tinggi untuk disatukan dengan bahan komposit dalam perlaksanaan permantauan berterusan kondisi struktur objek. Namun begitu, kajian mendapati sistem permantauan berdasarkan FBG dilihat mepunyai beberapa kelemahan dari segi statik dan juga dinamik. Variasi dari keluaran voltan menyebabkan bacaan yang tidak tepat. Kaedah ilustrasi spektrum dalam pentafsiran statik juga dikenalpasti sebagai kelemahan dalam pengukuran statik. Bagi kelemahan dalam pengukuran dinamik, kesukaran dalam perbezaan masa antara dua isyarat menyebabkan anggaran sumber isyarat yang tidak tepat. Justeru, tujuan utama kajian penyelidikan ini adalah untuk meningkatkan serta penambahbaikkan dalam sistem permatauan berdasarkan FBG.

Dua spesimen telah dibentuk iaitu plat komposit dan rasuk komposit yang berasaskan kaedah laminasi. Penderiaan FBG telah diintegrasikan ke dalam kedua-dua spesimen tersebut. Bagi penambahbaikkan dalam permantauan secara statik, kedua-dua specimen tersebut dikenakan beban. Secara hasilnya, fungsi grid jaring digunakan sebagai paparan interaktif yang mewakili struktur objek berkenaan dan akan memaparkan kondisi struktur semasa berlaku pesongan. Algoritma penormalan voltan pula berjaya mengurangkan variasi keluaran voltan dari 26 data/minit kepada 17 data/minit. Bagi penambahbaikkan dalam permantauan secara dinamik pula, kesan penyetempatan dijalankan ke atas rasuk pada tempat tertentu. Secara hasilnya, algoritma CC-LSL mampu membuat anggaran impak secara tepat dengan peratusan kesilapan pada 2.47% dari impak sebenar. Secara kesimpulan, dipercayai bahawa sistem bereputasi ini mampu mencapai konsep utama struktur pintar.

Key researchers: MOHD HAFIZI BIN ZOHARI
CHE KU EDDY NIZWAN BIN CHE KU HUSIN
MOHD FAIRUSHAM BIN GHAZALI
DAING MOHAMAD NAFIZ BIN DAING IDRIS
MOHD SHAHRIR BIN MOHD SANI

Email.   : hafizi@ump.edu.my
Tel. No. : 0179860752
Vote No. : RDU170388

TABLE OF CONTENT

LIST OF TABLES

LIST OF FIGURES

xii

LIST OF SYMBOLS

λ_B	Bragg wavelength
°C	Celcius
$\Delta\lambda_B$	Change of Bragg wavelength
ΔT	Change of temperature
Δt	Change of time
κ	Grating orders
η_{eff}	Grating refractive index
Cg	Group of velocity
Λ_o	Initial grating period
μ	Micro
%	Percent
η_o	Refractive index
Fs	Sampling frequency
ε	Strain
â	Thermal expansion
ξ	Thermo-optic coefficient

LIST OF ABBREVIATIONS

AE	Acoustic emission
ASE	Amplified spontaneous emission
BVID	Barely visible impact damage
CO_2	Carbon dioxide
CFRP	Carbon fibre reinforced plastic
cm	Centimetre
m^3	Cubic metre
dB	Decibel
EMI	Electromagnetic interference
ET	Electromagnetic testing
FP	Fabry-perot
FFT	Fast Fourier Transform
FBG	Fibre Bragg grating
FOS	Fibre optic sensor
FRP	Fibre-reinforced polymer
Ge	Germanium
GFRP	Glass fibre reinforced plastic
g	Gram
GUI	Graphical user interface
Hz	Hertz
InGaAs	Indium-Gallium-Arsenide
JSCE	Japan Society of Civil Engineers
kg	Kilogram
kHz	Kilohertz
km	Kilometre
kPa	Kilopascal
LCCA	Life-Cycle Cost Assessment
MHz	Megahertz
MPa	Megapascal
MEMS	Micro-electromechanical systems
μm	Micro-metre
με	Micro-strain
mm	Millimetre
ms	Millisecond

mV	Millivolts
nm	Nanometer
N	Newton
NOx	Nitrogen oxides
NDE	Non-destructive evaluation
NDT	Non-destructive testing
OSA	Optical spectrum analyser
PD	Photodetector
Pe	Photo-elastic
pm	Picometre
POF	Plastic-based optical fibre
PTFE	Polytetrafluoroethylene
PVDF	Polyvinylidene fluoride
PLC	Programmable logic controller
RT	Radiographic testing
s	Second
SMA	Shape memory alloy
SMP	Shape memory polymer
SNR	Signal to noise ratio
Si	Silicon
SHM	Structural health monitoring
SLD	Superluminescent diode
UT	Ultrasonic testing
UV	Ultraviolet
VT	Visual testing
V	Volts

CHAPTER 1

INTRODUCTION

1.1   Background Study

Fibre-reinforced polymer (FRP) is a composite material of polymer matrix stiffened with fibres. Literally, a composite material is a combination of two or several materials with different properties desired in achieving a new material with specific material properties (Vinson & Sierakowski, 2012). The unique characteristics of composite material have engaged immense number of engineering experts in designing advanced structures. Enormous number of researchers (Kesavan, Ravisankar, Senthil & Farvaze, 2013; Vignesh, Praveen & Prabhu, 2012) working on the composite material have unanimously been on the same view that high strength to weight ratio is the main interest of composite material. Other dominant aspects such as cost, ease of fabrication, corrosion resistance, heat resistance, wear resistance and specific strength are also the attractiveness of composite material (Glisic & Inaudi, 2008; Si & Baier, 2015; Vignesh et al., 2012). Applications of composite materials have been diversely utilized in several major engineering fields, for instance, manufacturing of aircraft in aeronautical application (Mangalgiri, 1999; Raffaella & Donati, 2013), manufacturing of automobile in automotive industry (Papantoniou, Rigas & Alexopoulos, 2011), infrastructures such as wind turbines (Brondsted, Lilholt & Lystrup, 2005; Ciang, Lee & Bang, 2008), and civil engineering works such as dams, bridges, large subway areas, ships and tunnels (Moyo, Brownjohn, Suresh & Tjin, 2005; Shen, Yan, Xu, Tang & Chen, 2015).

From the viewpoint of advantage, composite materials truly have the upper hand over conventional metallic materials. However, a composite material is often associated with several disadvantages such as complication in repairing, deterioration of strength due to vulnerability to heat, immense initial setup cost, delamination or cracks during fabrication, and above all, the failure of reaching the complex criteria of the composite

material (Chandrashekhar & Ganguli, 2016; Kahandawa, Epaarachchi, Wang, Followell & Birt, 2013; Kahandawa, Epaarachchi, Wang & Lau, 2012). Seeing that composite material is prone to unexpected damage, a monitoring of the structural health condition has to be implemented prior to further tremendous deformation that can alter the performance or cause Catastrophic, which is the sudden damage of the structure. For that reason, structural health monitoring (SHM) of composites is a prerequisite in detecting the unforeseen damage of the structure. SHM is a process intended at providing precise and real time information regarding the structural condition and performance. According to Kahandawa, SHM is a process that involves the observation of dynamic response from an arrangement of sensors periodically over time (Kahandawa et al., 2012). Non-destructive testing (NDT) is among the few of inspections that can be utilized for SHM.

Some of the common NDT tests are Visual Testing (VT), Ultrasonic Testing (UT), Thermography, Radiographic Testing (RT), Electromagnetic Testing (ET), Acoustic Emission (AE), Shearography, resistance strain gauges, piezoelectric sensors, micro-electromechanical systems (MEMS) and eddy current sensors (Cai et al., 2012; Iacoviello et al., 2016). However, the size and weight constraints of the systems make NDT inspection difficult to implement and integrate with the structure as a whole (Zhu, Tian, Lu & Zhang, 2011). Therefore, fibre optic sensors, like Fibre Bragg Grating (FBG) sensing, have been regarded as hotspot sensing elements by various researchers in the field of SHM (Jian & Hong, 2009). FBG technology is contemplated as one of the fastest flourishing topics deliberated in the field of fibre optic sensors during the late 20th century (Rao, 1999). Characteristics such as small physical size, immunity to electromagnetic interference, light weight, relative signal stability and wavelength multiplexity have made this sensor the most suitable technology to be implemented in the SHM (Dai, Li, Liu, Asundi & Leng, 2014; Pereira, Frias, Faria, Frazao & Marques, 2013; Zou, Liang & Zeng, 2012).

FBG is a multi-sensing sensor that has the benefits of measuring strain, temperature, pressure, acceleration and displacement. In general, an FBG sensor functions by elongation as it encounters environmental changes. Measurements of strain, pressure and displacement are done by physical elongation. Strain and displacement are measured by surface attachment or embedment of the FBG sensor in a

host material such as composites. The host material is then subjected to physical measurement from the elongation of the optical fibre. For temperature sensing, the environmental temperature will cause the optical fibre to expand in hot temperature, and contract in cold temperature. This phenomenon will cause the grating period to be wider or narrower as the temperature changes. For accelerometer development as shown in Figure 1.1 (W. Zhou, Dong, Ni, Chan & Shum, 2010).
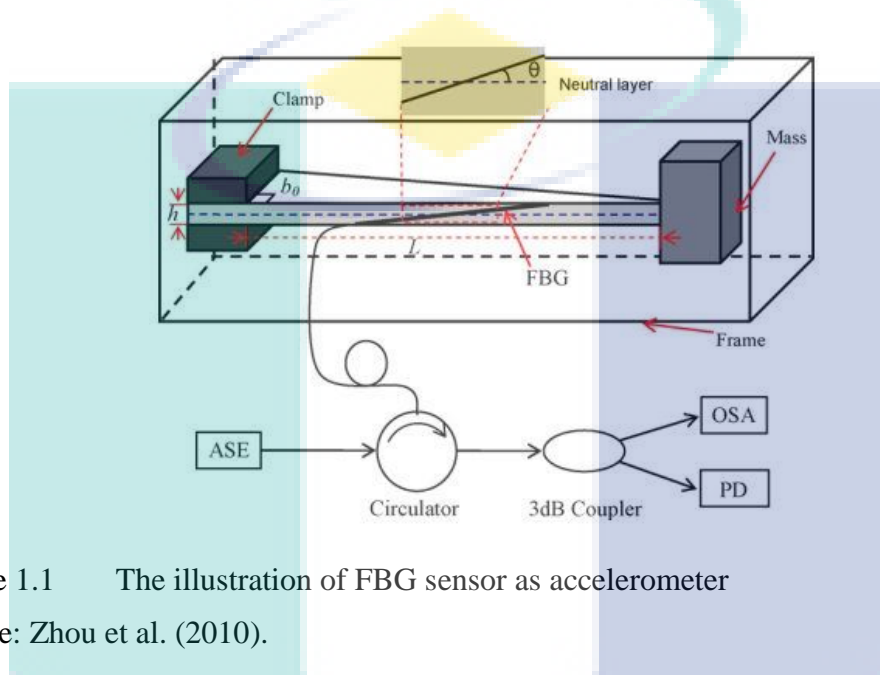
Figure 1.1   The illustration of FBG sensor as accelerometer
Source: Zhou et al. (2010).

The FBG sensor is pasted on a cantilever beam which will result in strain bending as the cantilever beam is loaded with mass. When acoustic emission vibration was induced on the accelerometer, the cantilever beam will vibrate and pull the FBG, resulting in elongation. The FBG sensor was illuminate with amplified spontaneous emission (ASE) through the circulator and the reflected spectrum was viewed from optical spectrum analyser (OSA) and photodetector (PD).

There are two types of interrogation systems, which are power detection method and edge filter detection method (Lee, Jeong, Yin, Ruffin & Yu, 2008). In edge filter detection method, the shift in the FBG spectrum is detected by the use of a spectrally-dependent filter which results in a change in intensity at the detector as shown in Figure 1.2 (Wild & Hinckley, 2010). Here, the sensing and matched FBG was illuminated by the broadband light source through 3 dB coupler. The bandwidth from the matched FBG was slightly broader than the sensing FBG.
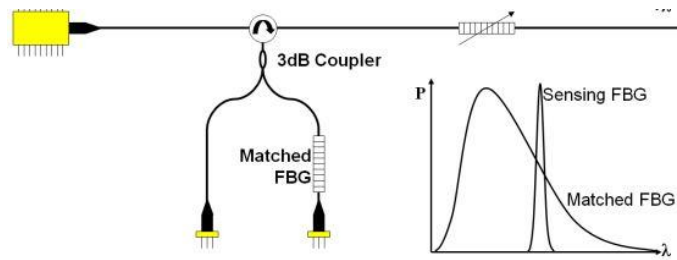
Figure 1.2   The edge filter detection method
Source: Wild et al. (2010).

In power detection method, the shift in the FBG spectrum is detected by using a spectrally-dependent source which results in a change of intensity at the detector (Wild & Hinckley, 2010). There are two types of power detection methods, namely the linear edge source (Lee et al., 2008), and the narrow bandwidth source (Webb et al., 1996). In linear edge source, the bandwidth of the light source is relatively broader than the FBG sensor bandwidth as shown in Figure 1.3(a). In narrow bandwidth source, the bandwidth of the light source is narrower than the FBG sensor bandwidth as shown in Figure 1.3(b). In conclusion, for the interrogation system, the edge filter detection method is the most favoured method in terms of cost and simplicity.

(a)

(b)
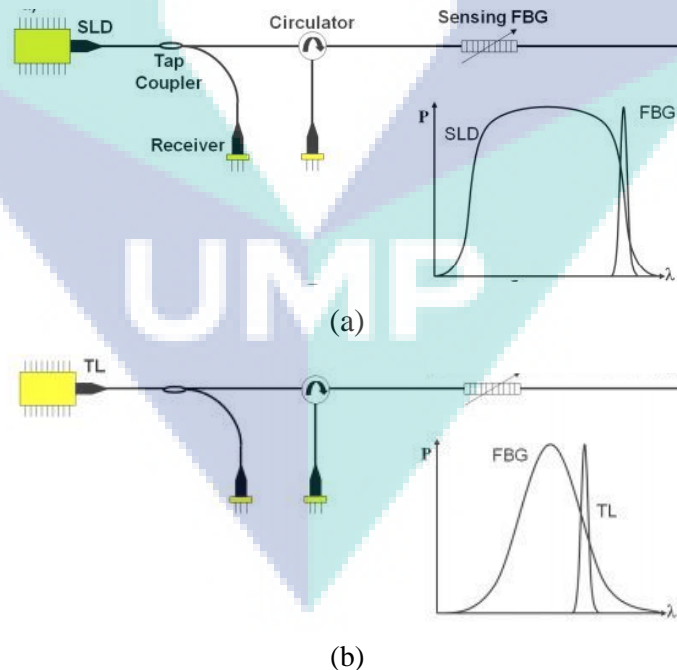
Figure 1.3   The power detection method: (a) Linear edge source (b) Narrow bandwidth source

Source: Wild et al. (2010).

4

Studies and experimentations on strain sensing neither static nor dynamic have been practiced for the last few decades. Establishment of a mature real-time monitoring system that can instantly alert the end user or expert is the intention behind these studies. Distinctive manipulation of interrogation system in obtaining the strain signal and transforming it to a real-time voltage or wavelength spectrum is the most conventional way of practice. Respective complications have been encountered in utilizing this practice, such as inconsistency in voltage readings which generate large variation in readings. Furthermore, the indirect sensing and working principle of the FBG sensor has contributed to the presence of highly uncertain noise in seismic signal, making the source impact localization through time of arrival method, difficult and inaccurate. Thus, the deficiencies and obstacles from the previous research have generated the problem statement of this research study, to determine an effective way to overcome the drawbacks.

1.2   Problem Statement

Assorted studies related to SHM, based on FBG that have been implemented are not limited to laboratory experimental testing, but also practices in real-life engineering structures. However, still, there is a synonymity in most of the studies, which is the lack of readiness level in real-time monitoring system, both for static strain and dynamic strain sensing measurement. In static strain measurement, utilization of edge filter interrogation system is indeed the most economical and cost-effective method among other interrogation systems. However, the interpretation of light signal to the electrical voltage signal from intensity demodulation, utilizing photodetector accounted with voltage inconsistency and variation, resulted in huge error on the desired readings. Pre-calibration has to be carried out each time before operation due to the disparate initial voltage value on a particular day. This complication has been encountered in several studies (Allwood, Wild, Lubansky & Hinckley, 2015; J. Ma et al., 2016; P. Ma, Wang, Ma, Zhou & Liu, 2014). The traditional and conventional way of interpreting the static strain through spectrum illustration (Rodrigues, Cavadas, Felix & Figueiras, 2012; Roveri, Carcaterra & Sestieri, 2015) gives a drawback to the end user where signal experts are required.

In dynamic strain measurement, source location estimation is commonly decoded from the reflected Bragg wavelength by employing high-speed interrogator

(M. Jiang et al., 2015; Lu, Jiang, Sui, Sai & Jia, 2015). The determination of time of arrival from the estimation of seismic signal peak difference is difficult and challenging, due to the presence of uncertain noise, which leads to imprecise impact location estimation. Several algorithms such as autocorrelation (Caucheteur, Chah, Lhommé, Blondel & Mégret, 2004), centroid detection (Askins, Putnam & Friebele, 1995), least square method (Ezbiri, Kanellopoulos & Handerek, 1998) and cross-correlation (C. Huang, Jing, Liu, Zhang & Peng, 2007) can be appointed in intensifying the peak spectra for time of arrival estimation. However, cross-correlation algorithm demonstrates a good performance in suppressing the uncertain noise (W. Huang, Zhang, Zhen, Zhang & Li, 2014; Qingwen, Tokunaga & He, 2011; Wenzhu, Zhen, Zhang, Zhang & Li, 2015).

Thus, such complications and problems have lead to the dispute of whether present static and dynamic monitoring assessment are practical in the development of the smart structure. In general, the main aim of this experimental work is to improve the current real-time FBG monitoring system in static and dynamic strain sensing, with the use of certain functions and improved numerical analyses such as voltage normalization to reference voltage algorithm, cross-correlation with linear source location algorithm, Fast-Fourier transform (FFT) function, and mesh-grid function. All the numerical analyses are fully developed in MATLAB graphical user interface (GUI) and function entirely in real-time, which brings the FBGs real-time monitoring system to a fully mature readiness level.

A brief summarization on how this research study has been narrowed down from a broad scope to find the gap of the research study is illustrated in K-chart in Figure 1.4. The chart first describes about the pros and cons of composite materials. Next, the utilization of several common NDT inspections is clarified. FBG sensors was the most preferred method in SHM of composites. However, critical review of the current real-time FBG based monitoring system shows that it truly needs certain improvement. In general, the experimental work carried out in this research study aims at improving the current FBG real-time monitoring system both in static strain and dynamic strain. The objectives specified and scope fixed for this research study are detailed in the following subtopic.
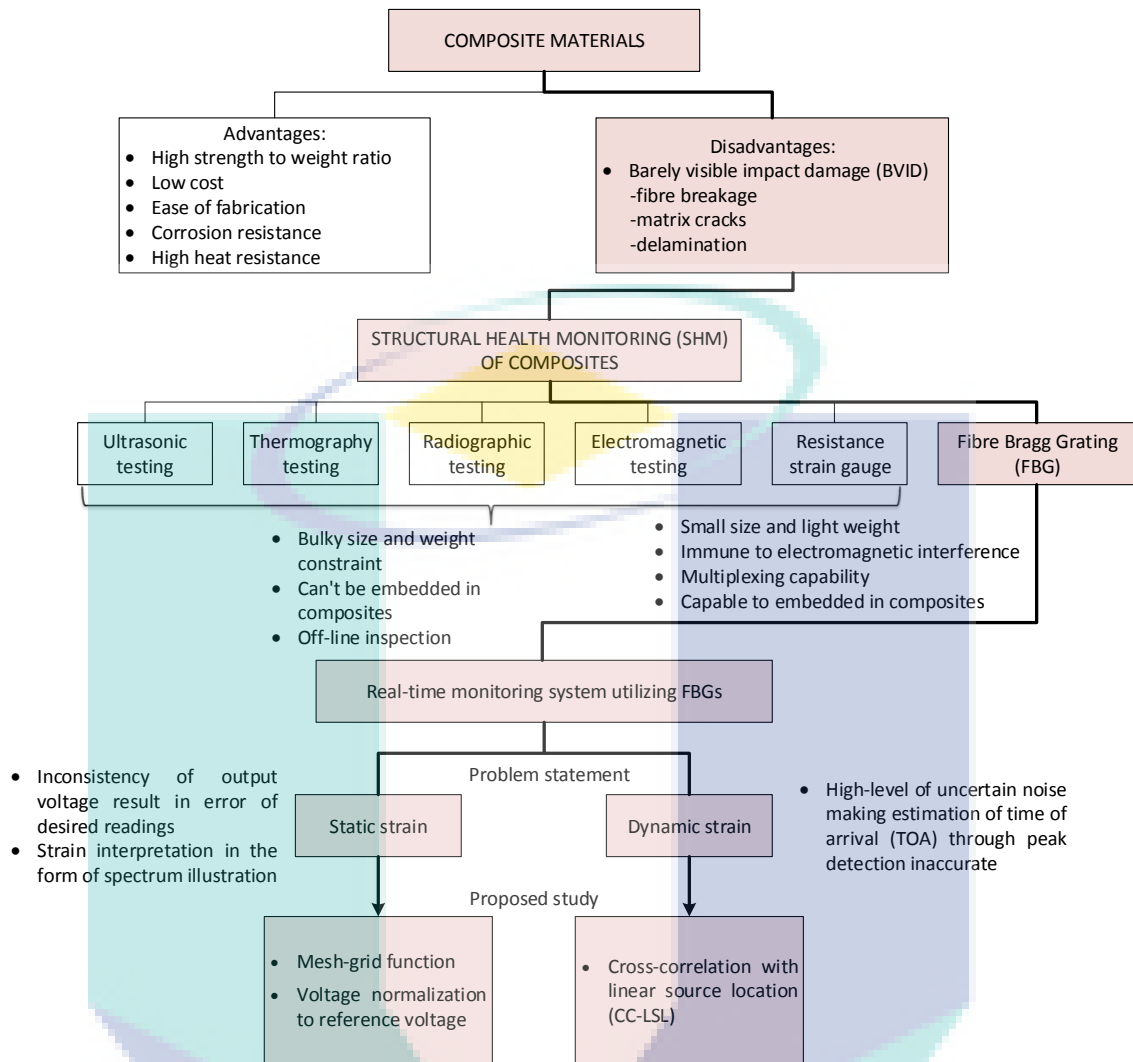
Figure 1.4   K-chart for the narrowing down process of this research study

1.3   Objectives

a. To develop and assess an FBG based static and dynamic interrogation system for real-time composite structure monitoring.

b. To enhance static strain measurement accuracy using mesh-grid function and voltage normalization algorithm.

c. To develop a source location algorithm based on cross-correlation with a linear source location technique for the improvement of dynamic strain sensing.

1.4   Scope

    a. Matched edge-filter interrogation system was implemented for strain performance.

    b. 1550 nm Fibre Bragg Grating (FBG) sensor was adopted with the embedment in hand lay-up fibreglass laminations that were being induced by static and dynamic strain.

    c. Fast Fourier Transform (FFT) function, Mesh-grid function, Cross-correlation with linear source location (CC-LSL) technique and Normalization analysis were implemented in MATLAB real-time graphical user interface (GUI) as a tool to analyze and monitor the strain measurement.

1.5   Significant/Contribution of Study

    a. The improvement in the numerical analysis and mathematical algorithm such as CC-LSL and voltage normalization with the advancement of MATLAB GUI have built up a more mature FBGs real-time monitoring system in terms of both static and dynamic measurement. The static measurement with mesh-grid function can be utilized in monitoring of bridge deflection due to the passing of heavy traffic. This mesh-grid function capable in meshing the shape and size of the bridge and display the deflection in real-time when load from vehicles induced on the bridge. This function also suitable in monitoring of aircraft wings' deflection during take-off moment. On the other hand, the improved impact localization determination for dynamic measurement can be adapted in any linear structure such beam, pipe or rod in estimating for any foreign object falls on the structure.

1.6   Thesis Organization

Chapter 1 which is the introduction of this research study, explains about the background and problem statement of this study. Objectives and scopes in order to

overcome the problem statement are also listed. The last subtopic of this chapter is the significance or contribution of this study.

Chapter 2 which is the literature review, explains about the application of composite materials and their associated problems. The fundamental and working principle are also detailed. Critical review of current real-time FBG monitoring system is also defined.

Chapter 3 is the research methodology, justifying all the experimental procedures as a proof of concept in overcoming the problem statement. The experiments carried out are categorized into two, which are the improvements in terms of static and dynamic strain measurements.

Chapter 4 shows the results of the experimentation. The discussion of the results validates that the findings agreed well with findings from other researches. This has proved that all the proposed solutions are capable of solving the problem statement.

Chapter 5 is the conclusion of this research study. This chapter verifies that all of the objectives stated have been achieved. Future works or recommendations are defined as well.

CHAPTER 2

LITERATURE REVIEW

2.1   Introductory to Composite Material

Composite materials have been outlived since the olden era where in ancient India, reinforcement of clay with short fibre such as husks or straws showed an enhancement in mechanical strength for several hundred years (Balaji & Sasikumar, 2016). A composite material is described as the merging of two or several specific materials with distinctively different physical or chemical properties (Kahandawa, 2012; Reddy, 2004). Beneficial properties can be enhanced by composite materials, including great strength and stiffness with much lower weight than conventional metallic materials such as steel and iron. Resilience to mechanical failures such as wear, and susceptibility to environmental natural process like corrosion make the composite materials retain a higher fatigue life well above the other metallurgical materials. Composites also act as an acoustical insulation that absorbs vibrational impact, aside from their attractive physical properties (Jones, 1998). Due to these improved properties, FRP has been adapted remarkably in various industrial fields (Alfredo et al., 2015). There are two types of the most commonly used fibres, which are the glass fibre and the carbon fibre. Glass fibre consists of immense fine glass fibres from melting the raw material of glass in a reservoir to a specific desired temperature. This molten glass is drawn mechanically under the act of gravity until fine filaments of glass fibres are formed, and instantly wound into a drum (Hull & Clyne, 1996). On the other hand, carbon fibre is much lighter and multiple times stiffer than glass fibre. This is due to the production and composition of the fibre itself, where fine carbon atoms are fused together to form a long chain crystallisation of fibre (Zoltek, 2016).

2.2 Applications and Global Demand of Composite Material

In the last few decades, FRP has become exceptionally recognized in many industrial fields, specifically in civil engineering and aeronautical engineering. From the reported survey carried out by Tony Roberts, who has 40 years of experience in the carbon fibre and advanced composites industry sectors, worldwide transaction of carbon fibre reinforced plastics (CFRP) are predicted to be $16.1 billion in the year 2011, and forecasted to reach $28.2 billion in the year 2015, and $48.7 billion by the year 2020 (Roberts, 2011). The worldwide requirement for carbon fibre tow in the year 2011 is predicted to be 46000 tonnes, and is forecasted to reach 140000 tonnes in the year 2020. Transaction of carbon fibre including small tow and large tow will increase from $1.6 billion in the year 2011 to $4.5 billion in the year 2020. Large tow demand is estimated to grow from 38% of all tow types in the year 2011 to 45% by the year 2020. Global demand of carbon fibre in the year 2011 is 17% in aerospace technology, 67% in wind energy and automotive, and another 16% in sports and goods. Wind energy and automotive will consume 46% of the world's demand by the year 2020 where wind energy market will increase to 54270 tonnes in the year 2020 from 10440 tonnes in the year 2011. Utilization of carbon fibre in aerospace and defence will increase to 18462 tonnes in the year 2020 from 7694 tonnes in the year 2011. In the year 2020, Japan will produce 25%, USA 28%, Europe 28%, China 9%, and others 10% of carbon fibre (Roberts, 2011).

In the automotive industry, composites are used in manufacturing to fulfil the performance and fuel efficiency (Cai et al., 2012). In infrastructures, blades of wind turbines are made of composites in order to improve energy harvest efficiency (Campbell, 2010). High corrosion resistance of composites is greatly accepted in the nautical application. Metal or ceramic matrix composites are used to fabricate brake and engine parts, which are subjected to high temperature. Composite fabrications are also dominant in sports and recreation market (Donaldson & Miracle, 2001). Figure 2.1 shows the potential of carbon fibre reinforced plastics (CFRP), while Figure 2.2 shows the potential of glass fibre reinforced plastic (GFRP) in market approach for the year 2013 (Ramakrishnan, Rajan, Semenova & Farrell, 2016). From the survey, the results signify that there will be a growing demand in aerospace industries in the coming years. The pie chart clearly indicates that carbon fibre is utilized the most in industries such as

aerospace and defence, wind turbine, sports, moulding, automotive, pressure vessels, civil engineering, marine and other industries, while glass fibre is mostly used in sports and leisure, construction, electronics, transport and other industries.
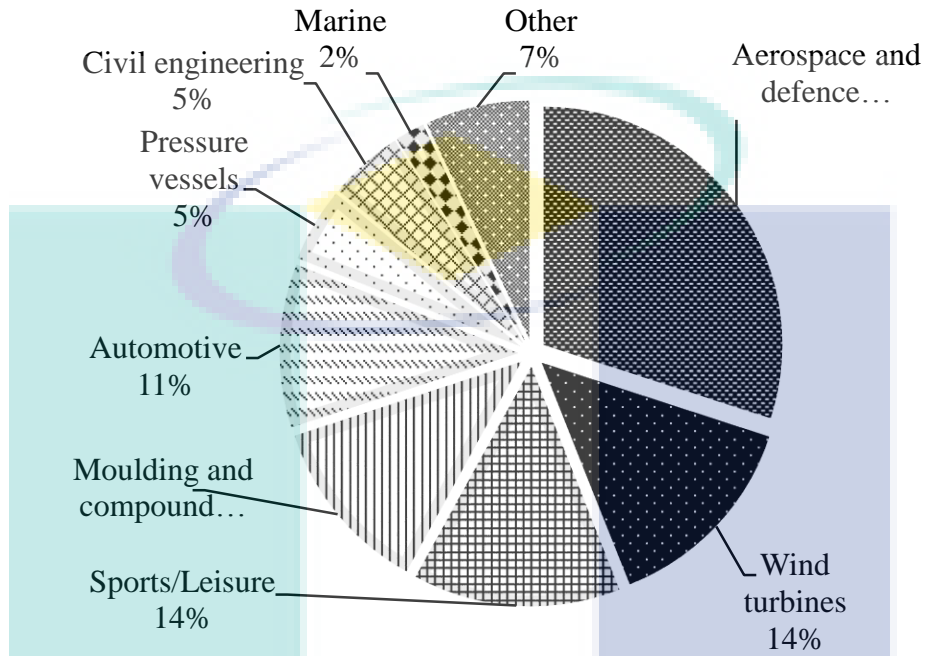
Figure 2.1　　Market research approach for CFRP
Source: Ramakrishnan et al. (2016).
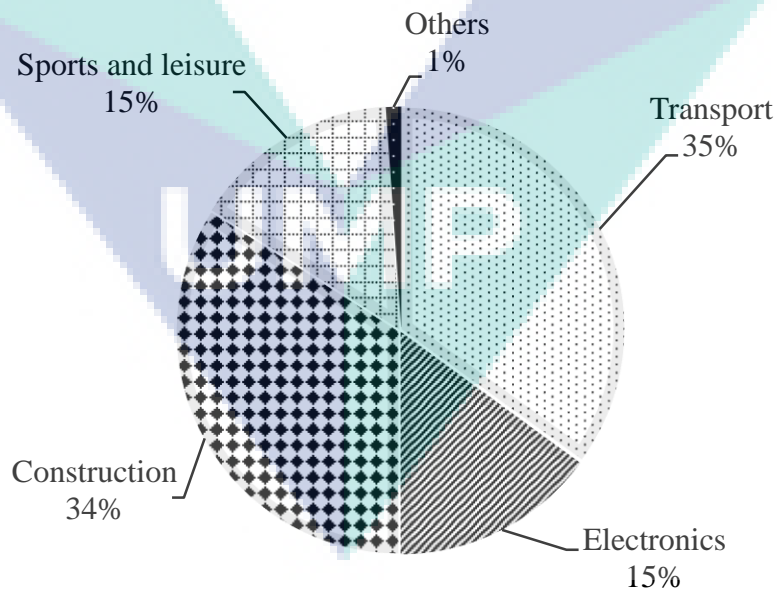
Figure 2.2　　Market research approach for GFRP
Source: Ramakrishnan et al. (2016).

Aerospace and defence majored in the market of carbon fibre with 30 percent usage, while marine applications fared the least with only 2 percent usage. For glass fibre reinforced plastic, construction sector constituted the most market with 34 percent usage, whereas electronics, and sports and leisure constituted 15% each. Civil structures and aeronautical application are the two major industries that exploit the most composites. The details of these two industries are further discussed in the following subtopic.

2.2.1   Composite Material in Civil Engineering

Composites have a successful advancement in civil engineering applications. Steel reinforcement used in construction is known to be vulnerable to corrosion while concrete could crack and chip off due to sulphate invasion (Shehata & Mufti, 2005). Thus, alternative capitalization of insusceptible material in civil engineering has to be implemented in order to overcome the disadvantages of conventional material. Japan which came second after the USA as the largest producer of composites in the world, as explained in Section 2.2, has introduced FRP reinforcement and tendons two decades ago (Hai, Mutsuyoshi, Asamoto & Matsui, 2010). The employment of FRP structures in real-life engineering application has achieved breakthrough significantly in several countries such as Scotland, Denmark, United Kingdom and Switzerland (Bakis et al., 2002; Keller, 2003). Japan is a country fenced by sea, which has caused its civil infrastructures to be severely vulnerable to corrosion. Deicing of ice using salt in snowy region has also led to corrosion in steel members. To overcome this, corrosion resistant material has to turn into account and hence FRP is the most promising solution. Okinawa Road Park bridge was the first all-FRP pedestrian bridge constructed in Japan in the year 2001 as shown in Figure 2.3 (Hai et al., 2010; Uno & Kitayama, 2003).

Figure 2.3   Okinawa road park GFRP bridge

Source: Hai et al. (2010).

In 1997, the first Japan Society of Civil Engineers (JSCE) standard specification has been proclaimed as the guidance for the design of FRP reinforcements, and has been espoused in other countries (Machida & Uomoto, 1997). Other FRP civil structures constructed in Japan are water gate and hydraulic gates at Komagari dam as shown in Figure 2.4.

Figure 2.4   FRP water gate at Komagari dam
Source: Nishizaki (2009).

Application of FRP composite materials in the civil application are not delimited by a whole structure of only FRP itself. The FRP can be adopted as superficially bonded sheets for retrofitting and reconstruction of damaged concrete structures (Lau, 2003; Lau, Yuan, Li, Wu & Chung, 2001). The reported work (Chudoba, Sharei & Scholzen, 2016; Qapo, Dirar & Jemaa, 2016; Truong, Larbi & Limam, 2016; Yehia, Douba, Abdullahi & Farrag, 2016) has brought to a culmination that FRP bonded concrete enhances the mechanical performance of the structure, notably in strength. Based on the Life-Cycle Cost Assessment (LCCA) for FRP structure studies carried out by Itaru Nishizaki (Nishizaki, 2009), several conclusions have been made where FRP costs 50%-100% more than a conventional structure. However, FRP reduces the cost in substructure and installation costs, and the maintenance cost is lower in FRP compared to the conventional structure.

2.2.2   Composite Material in Aeronautical Application

Aircraft industry is one of the industries that employs the most composites in the manufacturing of aeroplanes. Usage of composites in aircraft manufacturing has contributed to several key successes, such as the lightweight and high strength of aircraft body, which reduce the amount of emission and improve the fuel efficiency (Raffaella, 2015). Eurofighter, Typhoon comprises 40% carbon fibre, whereas the

14

proportion by weight of composites in USA fighters rises from 2% in F-15E to 35.2% in F-35/CV. For commercial aircraft such as Boeing 787, which has been produced in the year 2007 to present by the American multinational corporation, The Boeing Company, is composed of 50% composites by weight compared to Boeing 777 produced in the year 1993, which is constituted of only 12 percent composites, and 50 percent aluminium by weight (Raffaella, 2015). Figure 2.5 shows the present exploitation of composites, and other materials used by weight of percentage in the manufacturing of Boeing 787. Due to the priority of aviation in engaging domestic needs, Europe's key stakeholders have established visions for the year 2020, and Flightpath 2050 for the year 2050 (Henke, 2016). The specialized aim has been targeted to be achieved in the year 2020, for instance, CO_2 emissions is to be reduced by 50 %, NOx emissions by 80 %, accident rates by 80 %, and time released to market is to be reduced by half (Busquin, 2001).
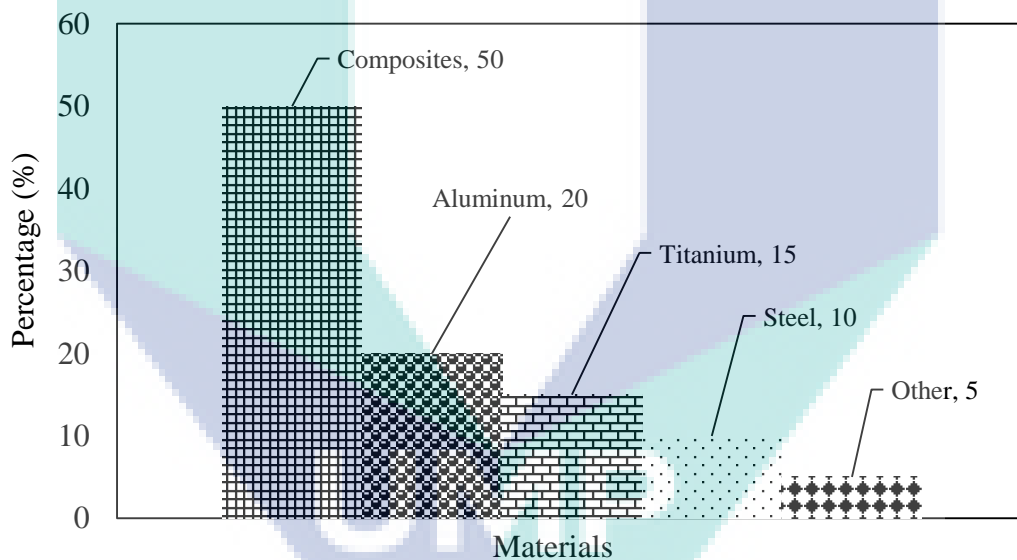
Figure 2.5   Manufacturing of Boeing 787 materials proposition

Source: Raffaella et al. (2015).

2.3   Problems Associated with Composite Material

Composite materials have undeniably gained its reputation specifically in civil engineering and aeronautical industries over conventional isotropic materials. However, despite the advantages, composites are not exempted from complicated defects. These anisotropic or orthotropic composite materials (Balaji & Sasikumar, 2016) are low in toughness, where they are often prone to low-velocity dynamic impacts, that result in

barely visible impact damage (BVID) that are difficult to be analyzed through visual inspection (Baker, 2004). This sudden total dynamic impact load generates more damage than gradually applied static load, where the damage is double the actual load due to inertia effects. Tool drops during service, or strikes from foreign objects are the examples of impact loads that propagate fibre breakage, matrix cracks, and delamination (de Moura & Goncalves, 2004; P. F. Liu, Liao, Jia & Peng, 2016), referred to as BVID that makes possible degradation of the structural integrity(M. Jiang et al., 2015; Rezayat et al., 2016). In general, the four types of failure mechanisms that can be encountered in composites are fibre failure, matrix cracking, buckling and delamination (Orifici, Herszberg & Thomson, 2008).

Fibre failure is where the fibres break due to applied loads. Matrix cracks are cracks or fractures that occur between fibres. Buckling occurs during compression or tension of structure which will not result in failure, however, excessive buckling will cause structural collapse. Delaminations are disengagement between layers of the composite laminate. Environmental effects such as moisture, UV radiation and temperature change can also cause adhesive degradation to the composite material (Fernandes, de Moura & Moreira, 2016). Composites that undergo service are often exposed to raining condition, humid surroundings, or substrates that can penetrate into the composites, and accumulate inside the fibre matrix which degrade the shear strength of the composites. The severity of the degradation depends solely on the amount of moisture absorbed as the composite will undergo dilatational expansion (Ray, 2006). The outer layer of the ply will swell but restrained by the dry inner ply during moisture absorption. However, during moisture desorption, the outer ply will shrink but restrained by the damp inner ply. This condition will result in deterioration of mechanical properties after a long term. UV radiation, on the other hand, will cause pigment loss over prolonged exposure.

2.4   Structural Health Monitoring (SHM)

Searching for an adequate monitoring method of the structural health conditions is crucial to monitor the condition of the composite structure, before any unforeseen damage, or intensification of damage that can lead to Catastrophic behaviour. Assimilation of SHM in structural monitoring utilizes the concept of intelligent structure that can react to the environmental loading. According to the review by

Gilewski et al. (2015), the intelligent structure is the combination of three key concepts, which are smart structure, smart material, and smart system that are functioning as a whole. The topic of the smart structure is comparatively new, as it emerged as a distinct field of applied science in the year 1980 (Anderson & Sater, 2007). Individual authors (Cazzulani, Cinquemani & Comolli, 2012; Zawadzka, 2014) defined the concept of smart structure in their respective ways, particularly on the approach of analyses. The examination of the structure as a whole, or focusing on single specific structural element are the approach of the analyses. Smart structures are structures that possess the ability to detect the changes in the environment. According to the PRNewswire report buyer by Sarah Smith (Smith, 2016), smart structure has a great potential in construction sector, such as bridges, buildings and tunnels where this structure is regarded as one of the best ways in reducing construction costs, improving energy efficiency, increasing the lifespan of a typical structure, and at the same time, adding aesthetic values to the structure.

The smart structure is able to sense and respond, which differentiates it from the conventional structure where traditional structure's function favour in providing strength and load carrying. However, the smart ones are able to transform their shapes, stiffness or damping characteristics in order to minimize deflection and possible damage. Smart materials are materials capable of converting the mechanical, magnetic, electrical and other forms of energy into another forms in a reversible and repeatable process. They are capable of sensing environmental changes, and respond to them by returning to their original shapes. Smart materials are frequently applied as an actuator in smart structures. Examples of smart materials are shape memory alloy (SMA) and shape memory polymer (SMP). Smart systems are systems that constitute of a smart structure, smart material and an advanced data processor. The implementation of smart systems ensures that during normal condition, the structure endures all the loads without stimulation from the smart components. Meanwhile, stimulation from the actuator will restore the structure back to its original position.

The fundamental of the smart structure is the assimilation of sensors, actuators, and control mechanism into a whole (Akhras, 2012). Thus, the FBGs integrated composites presented in this paper falls under the concept of smart structure. The smart system is composed of three constituents, which are sensors, actuators, and control unit

(Gilewski & Zawadzka, 2015). Sensors are responsible for capturing strain signal encountered by the structure, and conveying the signal to the control unit. The control unit is responsible for receiving the strain signal from the sensors, analysing the signal based on the algorithm, and conveying the processed signal to the actuator. Actuators are elements responsible in minimization of structural response. Actuators react by alternating the response condition of the structure, according to the signal computerized by the control unit. This action is capable of reducing the structural damage of the composites. The illustration of the smart system components is shown in Figure 2.6.
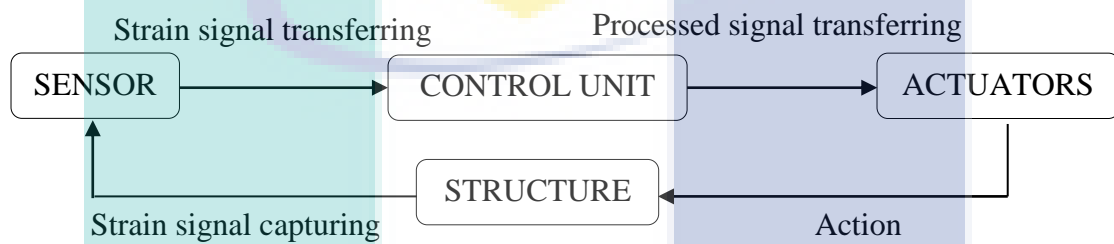
Figure 2.6   Smart system working components
Source: Gilewski et al. (2015).

Thus, adequate inspections that are capable of providing a closer look at defects on composites during SHM must be implemented, which traditionally utilize several common NDT inspections such as visual testing (VT), ultrasonic testing (Deng, Peng, Zhang, Qiu & Xue, 2012), thermography testing (Kroeger, 2014), radiographic testing (Tan, Watanabe & Iwahori, 2011), electromagnetic testing (Seung, Kim, Oh & Kang, 2013), acoustic emission (AE) (Sarasini & Santulli, 2014), shearography testing (Mininni, Gabriele, Lopes & Araujo, 2016), resistance strain gauge (K. Zhou & Wu, 2017), microelectromechanical system (MEMS) (Kavitha, Joseph Daniel & Sumangala, 2016) and fibre optic sensor (Guo, Xiao, Mrad & Yao, 2011).

However, all the above-mentioned NDT inspections retain identical drawbacks, such as the bulky size of the whole system, making it difficult to carry around and integrated with the structure as a whole. All the NDT inspections also indulge more on off-line inspection, which means that defects inspection on the structure is being made in one-shot, rather than providing a continuous on-line monitoring of the structure prior to happening of defects or damages. The hindrance of true strain detection by conventional sensors, such as strain gauge and acoustic emission sensors in structures concealed with FRP sheets, has ripened the conceptualized idea of smart composites,

which function as reinforcements, and at the same time as real-time structural health monitoring of the structure with the embedment of fibre optic sensors (Lau, 2003). Lately, fibre optic sensor (FOS), specifically fibre Bragg grating (FBG) sensor, has spiked the curiosity of enormous number of SHM researchers in replacing the conventional inspection. Details regarding FOS are furthered explained in the following subtopic.

2.5   Introduction to Fibre Optic Sensor (FOS)

Due to the disadvantages of conventional inspections, FOS has been regarded as a hotspot of sensing elements by various researchers in the field of SHM (Zhang & Zhao, 2009). FOS can be classified into three main categories, which are interferometric sensors, grating-based sensors, and distributed sensors as shown in Figure 2.7 (Guo et al., 2011; Raffaella, 2015). All the three types of sensors are differentiated by their sensing principles and capabilities. Under each types of sensors, there are several common sensing concepts with their own distinctive capabilities.
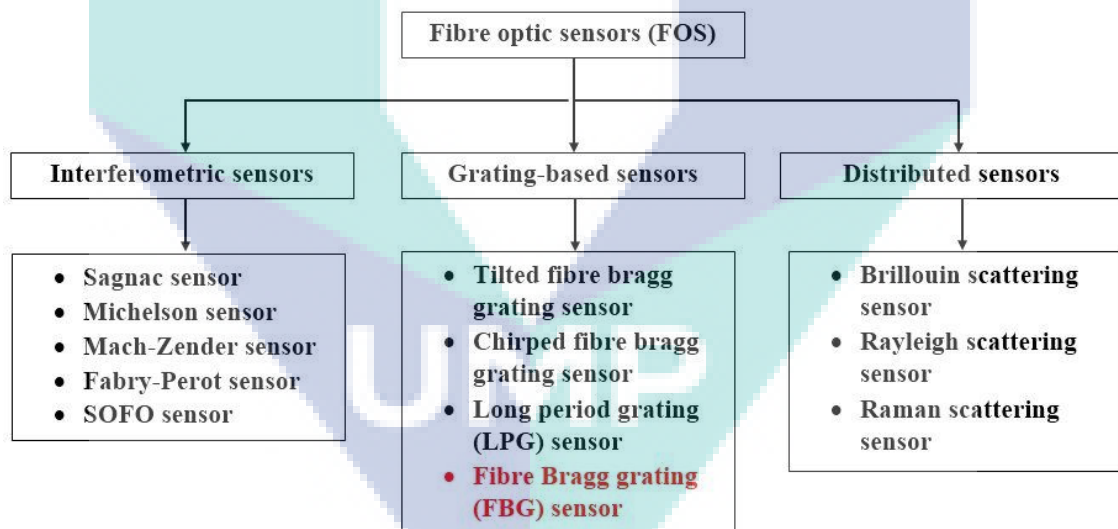
Figure 2.7   Types of FOS sensors
Source: Guo et al.(2011).

For quasi-distributed and distributed measurement, grating based sensors and distributed sensors are the most suitable to be utilized. Interferometric sensors, on the other hand, are suitable for single point measurement (Guo et al., 2011).

In distributed sensors, the optical fibre acts as a sensor where the scattered light along the optical fibre is used to detect the environmental changes. Three types of light are used in this measurement, namely Brillouin scattering, Rayleigh scattering and Raman scattering as shown in Figure 2.8 (Raffaella, 2015). Rayleigh scattering is based on non-propagating density fluctuations, whereas Brillouin and Raman scattering involve frequency shifting.
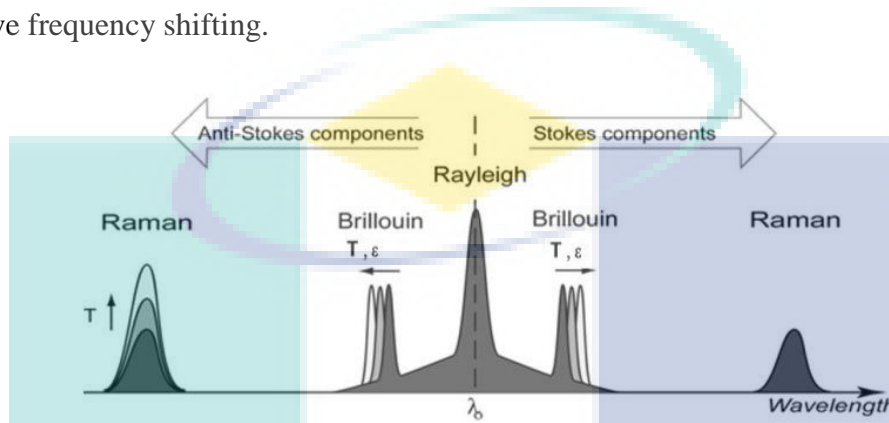
Figure 2.8   The spectrum of the scattering light in distributed sensors
Source: Raffaella (2015).

In general, Rayleigh and Brillouin scattering are used for strain measurement, whereas Raman scattering is used for temperature measurement. For grating based sensors, measurement of strain and temperature are based on the shifting of the reflected Bragg wavelength spectrum. Further explanation of this type of sensors is detailed in the next subtopic.

The working principle of interferometric sensors is through the contrast of optical phases between two light waves of the same frequency (Lee et al., 2012). The light emitted into the optical fibre was split into two, or parts and recombine to form a spectrum for measurement as in Figure 2.9.
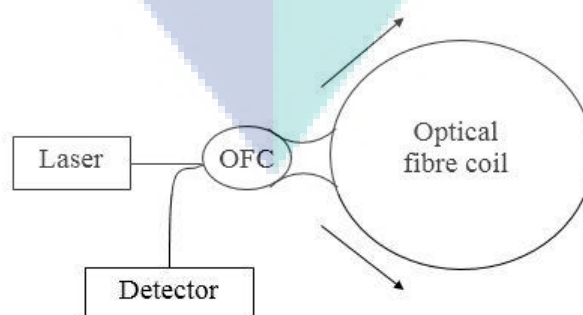
Figure 2.9   The Sagnac interferometric sensor interrogation system
Source: Bahrampour et al. (2012).

20

The system is known as Sagnac interferometric sensor interrogation system, where the light signal from the laser source was split into two paths, and circulate around the optical fibre coil (Bahrampour, Tofighi, Bathaee & Farman, 2012). The combined light signal was finally conveyed into the detector. For refractive temperature (Yuan, Zhou & Wu, 2000) and velocity sensing (Raffaella & Scalise, 2004), Mach-Zender interferometric, Michelson interferometric and Long period grating (LPG) (Lim, Jang, Lee, Kim & Lee, 2004) are the most preferred.

High resolution strain measurement can be achieved with the use of interferometric sensors. Fabry-Perot (FP) interferometric sensors possess the highest resolution in strain sensing at $0.15\mu\varepsilon$ with a measurable range of up to $\pm5000\mu\varepsilon$ compared to the other Interferometric sensors (Raffaella, 2015). FP sensors are formed where the optical fibre was separated by a gap known as aFabry-Perot cavity. A mirror was attached at both ends of the separated optical fibres as shown in Figure 2.10. When strain was exerted on the optical fibre, the spacing between the mirror changes, which result in a change of optical spectrum (National Instruments, 2011).
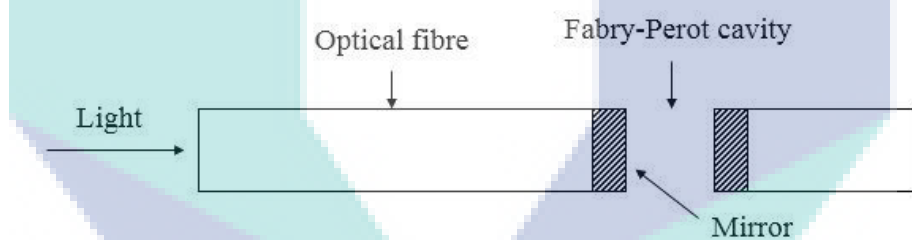
Figure 2.10   The illustration of the Fabry-Perot interferometric sensors
Source: National Instruments (2011).

SOFO sensors which inherit the name from French acronym "Surveillance d'Ouvrages par FibresOptiques" or translated as "structural monitoring by optical fibres" (Cheng & Ni, 2009) are long gauge sensors of up to a centimetre in length with micrometre resolution. The advantages of SOFO sensors are its stability, high precision and temperature resistance. The disadvantages of SOFO are having a low dynamic range which is only up to 1 Hz. All in all, the advantages of Interferometric sensors are the ability to withstand high temperature of up to 250 ºC, and also its small size which gives them the capability to be embedded into the structure without affecting its mechanical properties (Raffaella, 2015). The disadvantage of Interferometric sensors is its low multiplexing capability (Raffaella, 2015).

Among all the FOS, Fibre Bragg grating (FBG) sensors are the most adequate for composite damage detection and monitoring (Cusano, Cutolo & Albert, 2011; Luyckx, Voet, Lammens & Degrieck, 2011). FBGs outperform traditional NDT inspections, by reducing the need of long distance monitoring cables that could suffer from electromagnetic interference (EMI). Its light weight and small physical size enable them to be embedded inside composites that are free from damage due to environmental perturbation, making them stand well above the lifetime of the structures. The embedment of FBGs also enables them to have the same amount of strain at the related location. Its relative signal stability and wavelength multiplexity make it achievable to monitor large surface structure (Chen & Dong, 2012; Y. Li, Liu, Feng & Zhang, 2012; Ren, Jia, Li & Song, 2014). FBGs have been tested out of laboratory curiosity, and mainstreamed into real-life engineering applications where several works successfully (Chan et al., 2006; Moyo et al., 2005; Rodrigues et al., 2012). The fundamental and working principle of FBG is explained in subtopic 2.5.1.

2.5.1 Fundamental of FBG in Strain Sensing

It has been 40 years since the idea of utilizing optical fibres for sensing and measurement first emerged. The Photonic sensor which was based on bifurcated fibre bundles was patented in the mid-1960s. Half of the bundles are used to emit on a surface, and reflection from the surface will be received by the other half of the bundles. After a decade, the first single mode optical fibres was formed with the aspiration that it could be built into interferometers, which could weave its way to engineering benefits (Culshaw & Kersey, 2008). Optical fibre cables are commonly made of silica glass, and are plastic-based. For a glass optical fibre, two types of light mode transmit through the optical fibre, namely multimode and single-mode (MacChesney, 2006). Multimode transmission fibre can be categorized into two categories, which are step index and graded index. Plastic-based optical fibre (POF) is an optical fibre made of a polymer, which serves the same purpose and working principle as glass optical fibre, but at a much lower cost compared to glass optical fibre. The distinctive difference between multimode fibre, single-mode fibre and POF principally lies with the type of materials used in manufacturing, the diameter of the core, the light transmission wavelength and the distance of travel.

In general, a standard telecommunication glass optical fibre of multimode uses a core-cladding diameter of 50µm-125µm, whereas a single-mode optical fibre has a much smaller core-cladding diameter of only 9µm-125µm. Plastic optical fibre has the largest core-cladding diameter of 980µm-1000µm (Mike, Senior & Micrel, 2007). Figure 2.11 illustrates the difference in diameter between multimode, single-mode and POF optical fibre. The single-mode light transmission optical fibre is suitable for long-range applications, such as long-distance telephone communications which can reach up to 100 km long, in replacing the conventional copper wire, whereas multimode light transmission optical fibre is suitable for shorter range application of up to 2 km, such as communications between office buildings or industrial plant (Mike et al., 2007). Plastic optical fibre, on the other hand, is applicable to low speed, short distance operation of only up to 100 m long (S. C. J. Lee, 2009). Plastic optical fibre can be found on In-car entertainment (ICE) or In-vehicle infotainment (IVI) system, such as navigation system, radio, DVD player, bluetooth, and video players. Automotive critical safety application, for instance, airbags utilized POF for function (Mike et al., 2007).
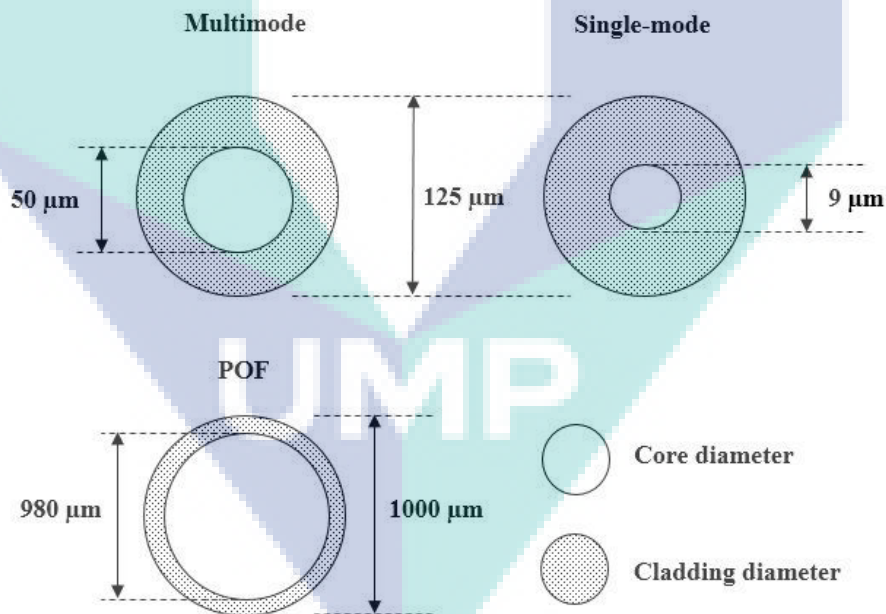
Figure 2.11   Illustration of the multimode, single-mode and POF optical fibre
Source: Mike et al. (2007).

The distinction in distance of light travel is due to the difference of core diameter that results in certain light travels propagation in the optical fibre. A standard optical fibre is made up of three layers, which are the core, cladding and a buffer

coating. The core is the light transmission area, and cladding is a region of the lower refractive index used to provide a reflective region at the core interface, so that light can travel throughout the core. A buffer coating acts as an extra protection to the optical fibre. Multimode optical fibre is made up of large diameter, that permits the light to propagate in multiple modes in the form of zigzag manner as the light signal encounters the cladding. This phenomenon is aroused in step index multimode, which results in the difference of time travel among the mode, known as modal dispersion that hinders the speed of digital pulse signal without overlapping with the zigzag light rays (Saleh & Teich, 2014). In graded-index multimode, the dispersions are diminished by grading the centre of the core region with a high refractive index, and low refractive index value at the cladding. This results in curve light rays that reduce the travelling distance, and generate equivalent time travel of light rays (Saleh & Teich, 2014). Single-mode optical fibre has the smallest core diameter that limits to only one mode of the light ray with negligible dispersion (Saleh & Teich, 2014). Single light pulse travelling in parallel to the core axis developes an ability to travel further. Figure 2.12 below shows all the light mode propagation.
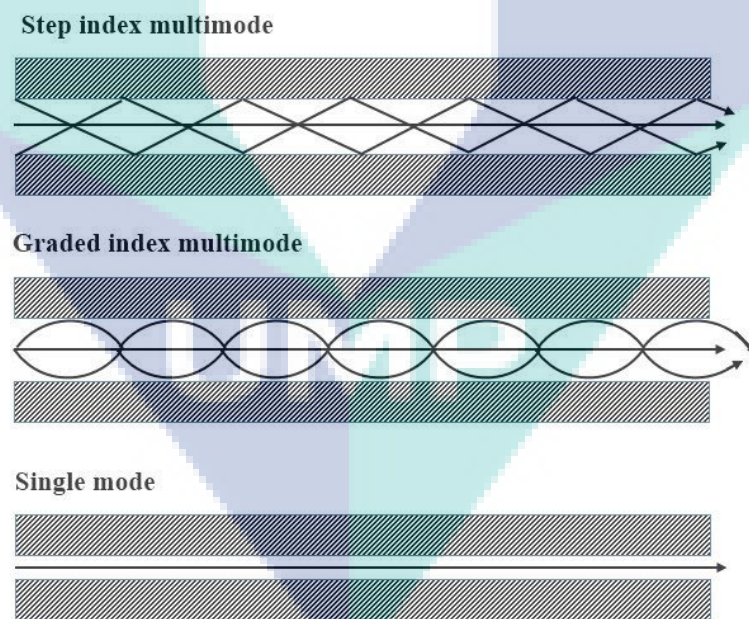
Figure 2.12   Light mode transmission in optical fibre
Source: MacChesney (2006).

There are three prime transmission light wavelengths used in glass optical fibre, which are 850 nm, 1300 nm and 1550 nm respectively. Short wavelength transmission light, such as that of 850 nm has high attenuation coefficient according to the

24

attenuation curve (Jim, 2014) as shown in Figure 2.13, which is suitable for short distance applications.
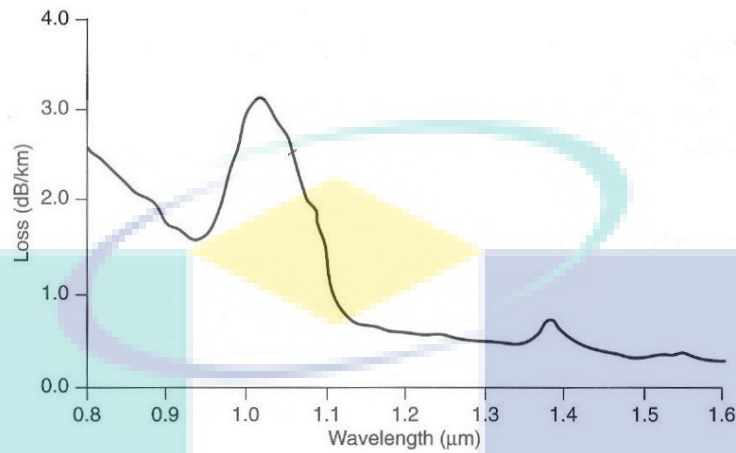
Figure 2.13   Optical fibre attenuation curve
Source: Jim et al.(2014).

The wavelengths of transmission lights at 850 nm and 1300 nm are used to illuminate the multimode optical fibre cable, whereas single-mode optical fibre often operates with 1310 nm and 1550 nm long wavelength, which have the lowest attenuation coefficient. Plastic optical fibre which has the biggest core diameter, has a shorter wavelength than glass optical fibre which is at 650 nm (Hayes & Works, 2002). Table 2.1 shows the specifications of each fibre optic cable.

Table 2.1   The specifications of each optical fibre cable

	Glass optical fibre	Plastic optical fibre
Material used	Silica glass	Polymer
Core-cladding diameter	50 μm - 125 μm (Multimode), 9 μm - 125 μm (Single-mode)	980 μm - 1000μm
Distance travel	up to 2 km (Multimode), up to 100 km (Single-mode)	up to 100 m
Transmission light wavelength	850 nm or 1300 nm (Multimode), 1310 nm or 1550 nm (Single-mode)	650 nm

Source: Hayes et al. (2002).

In order to revolutionize this state-of-the-art standard optical fibre into a strain measuring sensor, the core region of the optical fibre was sculptured with Bragg grating, which is simply known as fibre Bragg grating (FBG) sensor. FBG sensor has been tested and proven to be able to withstand the harsh mechanical and electromagnetic environments, of which the tests were carried out by James et al. in

studying the transient response of gun barrel by utilizing FBG sensors (James, Tatam, Fuller & Crompton, 1999).

1550 nm FBG sensor is most commonly adopted in SHM of composites, which are made up of standard single-mode 125 μm to 230 μm, including cladding and buffer silica glass telecommunication optical fibre. Spatially varied patterns of intense UV laser light which are used to break the optical fibre core and formed gratings. The Bragg grating inscribed on the optical fibre has the purpose of reflecting a specific narrowband of the light signal, depending on the Bragg properties (Yang, 2011). As a broadband light signal was used to illuminate the optical fibre and encounter the Bragg grating, a specific wavelength of the light signal was reflected back from the broadband light signal known as reflected light. The unreflected light signal passes through and over the Bragg grating as transmitted light. This working principle of FBG sensor is illustrated in Figure 2.14.
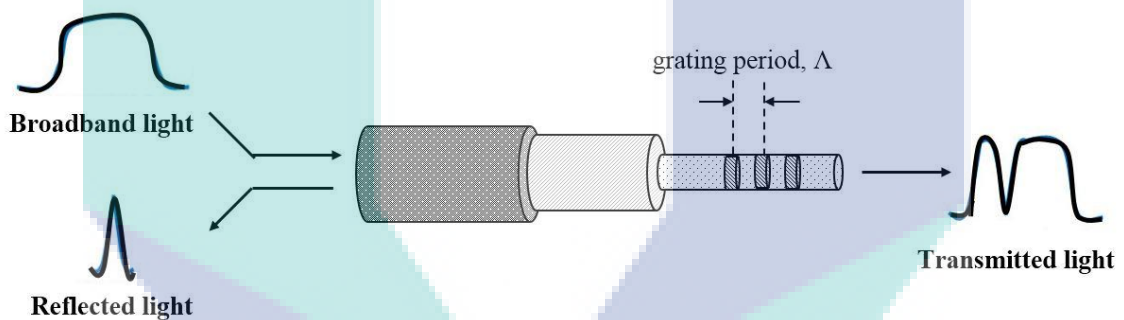
Figure 2.14   The working principle of FBG sensor
Source: National Instruments (2016).

The reflected light spectrum plays a significant role in strain sensing by undergoing left and right shifting as the optical fibre experience tension and compression strain. During the tensioning strain, the gap between the grating periods will be wider, and in contrary when the optical fibre is in compression.

The reflected wavelength from the laser inscribed Bragg grating is known as Bragg wavelength (λ_B) and it can be expressed as (Kahandawa et al., 2013):

$$\lambda_B = 2\eta_o \Lambda_o / \kappa \qquad\qquad 2.1$$

where Λ_o and η_o are the initial grating period, and refractive index before induced strain, respectively, and κ is the grating orders. The Bragg wavelength can also be defined in term of the grating refractive index (η_{eff}) as:

$$\lambda_B = 2\eta_{eff}\Lambda$$

<div align="right">2.2</div>

The Bragg wavelength shifts are also sensitive to the change of temperature. The wavelength shifts in terms of temperature and strain can be denoted as (Majumder, Gangopadhyay, Chakraborty, Dasgupta & Bhattacharya, 2008; Park, Lee, Kwon, Choi & Lee, 2003):

$$\frac{\Delta\lambda}{\lambda_B} = (â + \xi)\Delta T + (1 - \rho_e)\varepsilon$$

<div align="right">2.3</div>

where $\Delta\lambda$ is the change in wavelength, â is the thermal expansion, ξ is the thermo-optic coefficient, ΔT is the change in temperature, ρ_e is the effective photoelastic constant of the fibre, which is 0.22 for a single mode silica optical fibre (Yin, Dai, Karanja & Dai, 2015). The strain, ε is the ratio of change in length, ΔL to original length L, of a body expressed as (Pilkey, 2005):

$$\varepsilon = \frac{\Delta L}{L}$$

<div align="right">2.4</div>

However, for an isolated or controlled temperature sensitive condition, for instance, all of the experimental work of this research study was carried out in a temperature-controlled environment where the change in temperature could be neglected, the expression can be simplified as (Majumder et al., 2008):

$$\frac{\Delta\lambda}{\lambda_B} = (1 - \rho_e)\varepsilon$$

<div align="right">2.5</div>

Optical sensing technology has overwhelmingly well-established electrical sensing technology in several aspects, for instance, electrical noise immunity, sensor configuration and types of mounting as summarized in Table 2.2.

Table 2.2   Summarization of comparison between optical sensing and electrical sensing technology

Technology	Sensor	Electrical noise resistance	Sensor configuration	Sensor mounting
Electrical	Strain gauge	Low	Single point with one sensor/channel	Surface
	Vibrating wire	Moderate	Single point with one sensor/channel	Embeddable
Optical	FBG	Complete	Distributed with multisensory/channel	Surface and embedded

Source: National Instruments (2016).

Two of the most well-established conventional electrical sensing technology are foil gauge or strain gauge, and vibrating sensor (National Instruments, 2016). Strain gauge has a very low level of electrical noise immunity, especially in harsh surroundings. Complication with large surface area makes strain gauge sensor system inaccessible (National Instruments, 2016). The most challenging undertaking of dealing with electrical strain gauge is the retention of voltage drop over long distance wire implementation. Vibrating wire sensor has a moderate level of electrical noise immunity compared to the strain gauge. FBG sensor of optical technology overcomes the drawback of this electrical sensing technology with complete resistance to electrical noise. Furthermore, FBG is a distributed sensor with multisensory per channel, which allows nomination of this sensor in the implementation of complicated geometry, large surface area and long distance applications. FBG sensor is an indirect sensor where a set of equipments, known as the interrogation system, is needed to "liven up" the FBG sensors. Assorted up-to-date, common, and sophisticated interrogation systems with numerous configurations have been developed to make a breakthrough in the optical sensing technology, as the leading sensor in SHM, where the details are explained in the following subtopic.

2.5.2   FBG Interrogation System in Strain Sensing

In order for FBG to function, a working system known as interrogation system is needed to illuminate the FBG sensors. It is a signal transmitter and a receiver system, where the transmitter will transmit the light signal from a light source in the form of wavelength to the FBG sensor, and the reflected light signal from the FBG will be obtained by the receiver such as optical spectrum analyser (OSA) or photodetector (PD)

for the desired measurement. In FBG sensing system, a standard inexpensive telecommunication optical fibre can be utilised as sensing elements. However, the desired measurement of the interrogation system is still in demand in terms of cost and complexity (Raffaella, 2015). FBG sensing element works as an indirect system, which is contrary to the strain gauge and a piezoelectric sensor that are able to transform strain signal to electrical signal directly. Thus, an appropriate interrogation system to render a strain signal to an electrical signal has caught the concern of many researchers to come out with a more relevant interrogation system, as complicated interrogation system will result in higher optical loss and higher cost.

There are two types of interrogation systems, namely power detection and edge filter detection (Wild & Hinckley, 2010). Edge filter detection method utilizes broadband light source such as Superluminescent Diode (SLD), and the change of intensity of the photodetector is due to the shift of the sensor wavelength, matched with an FBG filter (Wild & Hinckley, 2010). For power detection method, the change of intensity at the photodetector is resulted from the shift in the wavelength, detected using a spectrally dependent source. Simply said, power detection interrogation system benefits in dynamic strain detection due to the use of laser type light source such as linear edge source (Lee et al., 2008) and narrow bandwidth source (Webb et al., 1996), whereas edge filter detection utilizes broadband light source and employed a reference FBG to mismatch with the sensing FBG.

Edge-filter or matched-edge filter interrogation system is the most economic and the most simple interrogation system (Tsuda, 2005). Edge filter detection utilizes the broadband light source and employs a reference FBG to mismatch with the sensing FBG as shown in Figure 2.15. As strain is induced, the sensing FBG will shift across the slope of the full-width half maximum (FWHM) of the reference FBG, and result in intensity variation.
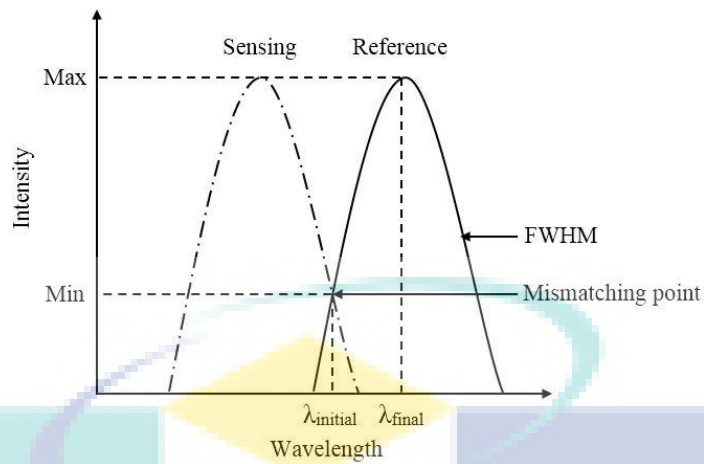
Figure 2.15 The working principle of edge filter detection

Source: Allwood et al. (2015).

A photodetector (PD) is commonly used to read the demodulation shift of the reflected intensity into an analog voltage signal. Figure 2.16 shows the working principle of the edge filter interrogation system, utilizing PD as the signal converter. The wavelength shift of the sensing FBG, labelled as A, will result in an intensity variation when sensing FBG slide across the slope of the reference FBG, labelled as B.
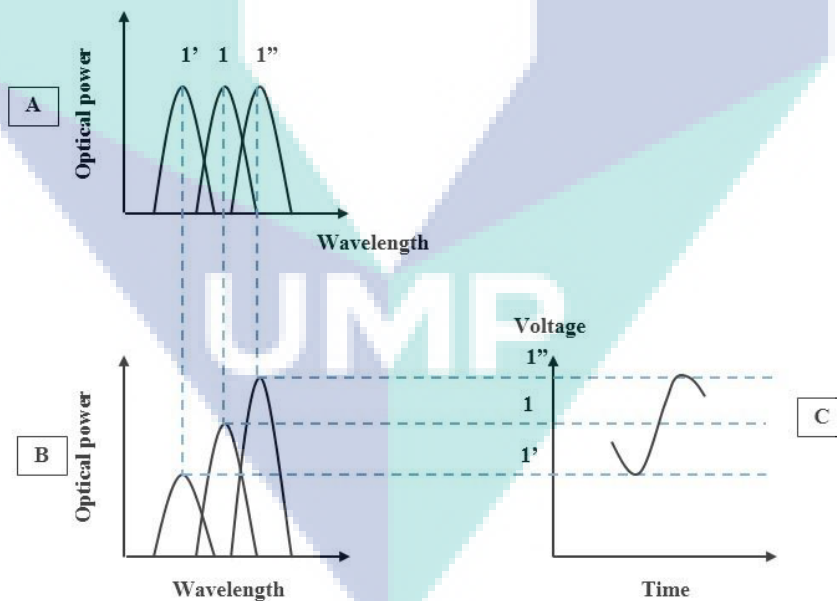
Figure 2.16 The working principle of the edge filter interrogation system utilizing photodetector as signal converter

Source: Hafizi (2014).

As a sequel, the photodetector will transform the intensity variation into a change of analog voltage signal, labelled as C (Hafizi, 2014).

For a clear picture of the working principle of an edge-filter interrogation system, an embedded FBG in a composite plate will undergo strain elongation as a point load is being exerted on the plate, with the condition that the plate is clamp fixed at both ends, as illustrated in Figure 2.17.
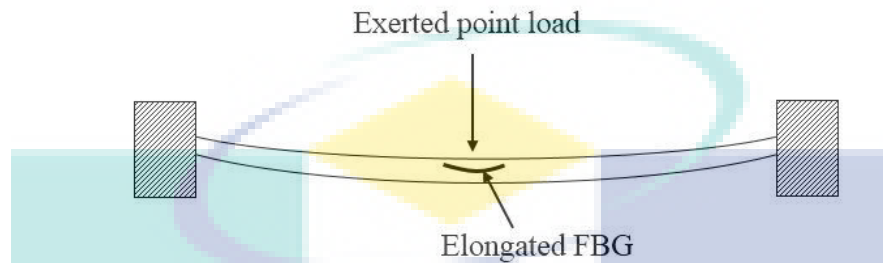
Figure 2.17　Illustration of the elongated embedded FBG due to strain
Source: Hafizi (2014).

This phenomenon will result in left and right shifts of the reflected Bragg wavelength from the FBG sensor. As the reflected Bragg wavelength passes through a reference FBG, the spectrum will undergo up and down shifts as shown in Figure 2.18.
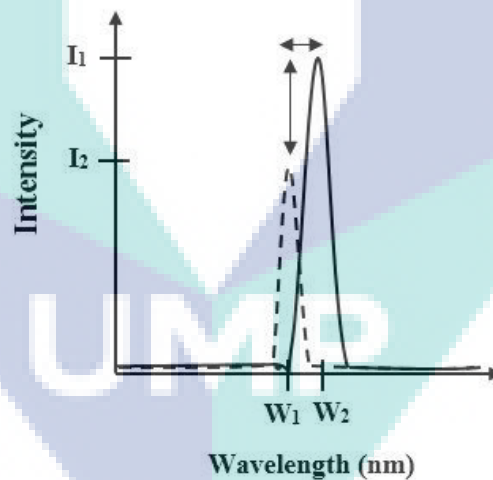
Figure 2.18　Shifting of the reflected Bragg wavelength due to strain
Source: Hafizi (2014).

The up and down shifting of the reflected Bragg wavelength is due to the intensity demodulation after mismatched with the reference FBG or FBG filter, where commonly a photodetector is utilized to convert the intensity demodulation to an electrical voltage signal. Photodetector or photodiode is the signal receiver, of which its obligation is to transform the light signal into electrical signal made of semiconductor materials,

particularly Silicon (Si), Germanium (Ge) and Indium-Gallium-Arsenide (InGaAs) (Cvijetic, 2004). Figure 2.19 shows the light intensity identified by the photodetector indicated in the shaded region.
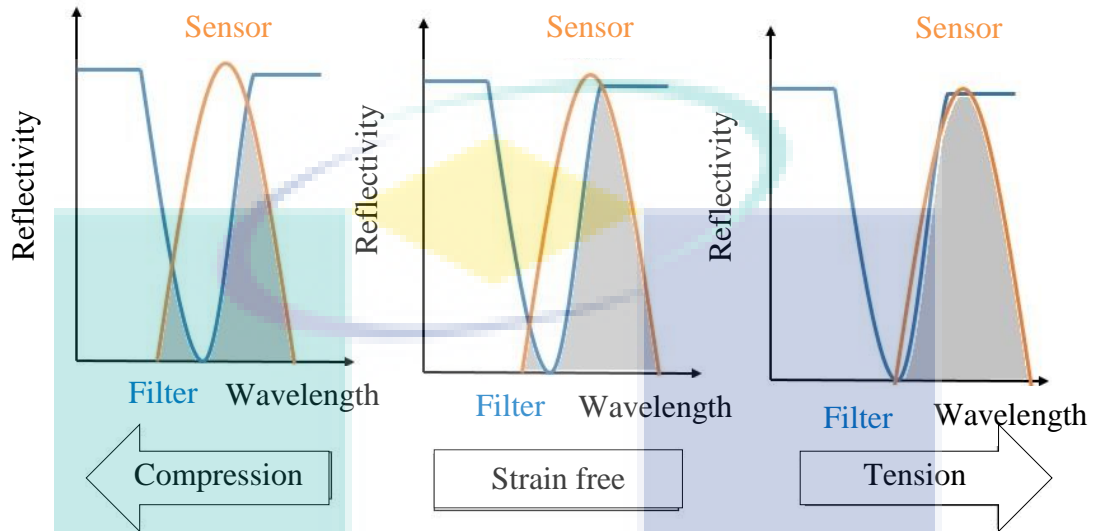
Figure 2.19   Light intensity as in shaded region identified by the photodetector
Source: Tsuda (2005).

The matched-edge filter interrogation system has been utilized in identifying the ultrasound and damage detection in CFRP using FBG sensors (Tsuda, 2005) with the configuration as shown in Figure 2.20.
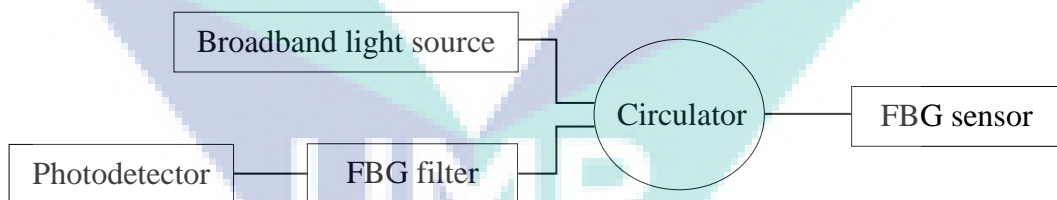
Figure 2.20   Matched-edge filter interrogation system by Hiroshi Tsuda
Source: Tsuda (2005).

The configuration of this system shows promising sensitivity, where the same configuration has been adopted in studying the dynamic sensing of FBGs (Zhang & Zhao, 2009). In this system, the broadband light source radiates light signal across the optical circulator and to the FBG sensor. Gratings on the FBG will reflect the light signal back to the optical circulator, of which its function is to circulate and convey the reflected light signal through the FBG filter and into the photodetector.

However, this configuration is associated with a significant drawback, which is the low power conversion efficiency with small dynamic range and decreased sensitivity due to low demultiplexed of power reflected by the FBG with an interrogation filter (Comanici, Chen, Kung & Wang, 2011). Thus, the optimization of Reflective Semiconductor Optical Amplifier (RSOA), which is a type of laser light source with a narrower bandwidth that is competent in increasing the output power, has been proposed as shown in Figure 2.21.
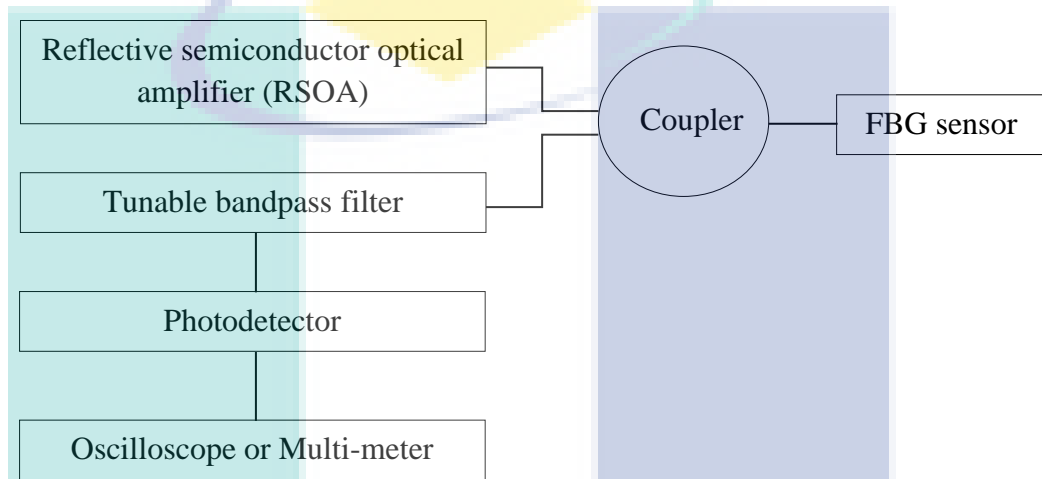
Figure 2.21   Interrogation system developed by Comanici et al
Source: Comanici et al.(2011).

Concurrently, Tsuda (2005) also developed an interrogation system utilizing a tunable laser as a light source in contrasting the sensitivity with the matched edge filter interrogation system for ultrasound and damage detection in CFRP as shown in Figure 2.22, where the tunable laser, which is a narrow bandwidth light source, is set to where the reflectivity of the sensor at strain free is reduced by half.
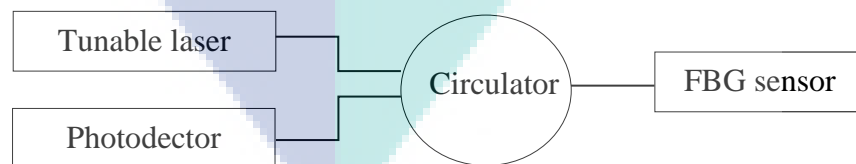
Figure 2.22   Interrogation system utilizing Tunable laser by Hiroshi Tsuda
Source: Tsuda (2005).

From the configuration, the tunable laser emits a narrow-band light signal into the FBG sensor via the circulator. The reflected light signal from the FBG sensor is conveyed to the photodetector without filtering by the FBG filter, which is dissimilar to

the matched-edge filter configuration. In short, the reflected light signal from the FBG sensor directly corresponds to the desired strain measurement.

Remarks from the tunable laser configuration are that higher sensitivity can be achieved due to high optical power utilizing narrow band light source. Apart from that, less optical components have resulted in less optical losses as well. However, the findings conclude that matched-edge filter configuration utilizing broadband light source is enough for practical use in terms of cost compared to tunable laser.

Other works include the use of a tunable Fabry-Perot filter to filter the reflected light signal from FBG sensor, and resulted in achieving a high-frequency measurement (Frieden, Cugnoni, Botsis, Gmur & Coric, 2010). A tunable Fabry-Perot filter is capable of shifting the wavelength by mechanical moving parts (Henderson, Webb, Jackson, Zhang & Bennion, 1999; Kersey, Berkoff & Morey, 1993), and the configuration is shown in Figure 2.23.
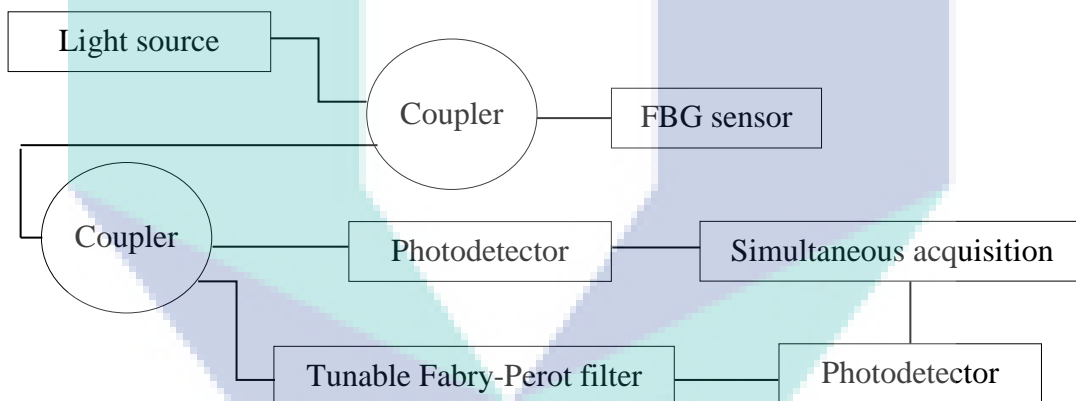
Figure 2.23   Interrogation system developed by Frieden et al
Source: Frieden et al. (2010).

From the configuration, tunable FP filter is used instead of FBG filter. The simultaneous acquisition electronic unit is used to capture the ratio between filtered and unfiltered reflected wavelength from the FBG sensor. Optical tunable filter, which has the same working principle as FP filter, has been utilized to measure dynamic strain using embedded FBG sensor in a composite structure, as shown in Figure 2.24 (Ling, Lau, Cheng & Jin, 2006).

```
┌─────────────────────────────┐          ╭─────────╮    ┌──────────────┐
│ Super luminescent light     │──────────┤ Coupler ├────┤  FBG sensor  │
│ emitting diode (LED)        │          ╰─────────╯    └──────────────┘
└─────────────────────────────┘
┌─────────────────────────────┐
│   Optical tunable filter    │
└─────────────────────────────┘
┌─────────────────────────────┐
│       Photodetector         │
└─────────────────────────────┘
┌─────────────────────────────┐
│      Signal analysis        │
└─────────────────────────────┘
```
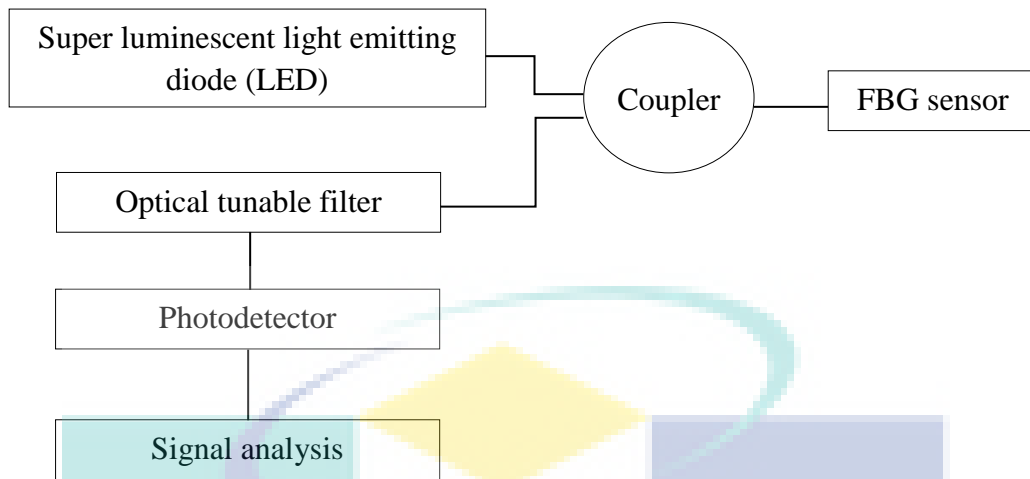
Figure 2.24   Interrogation system developed by Ling et al.

Source: Ling et al. (2006).

2.5.3   Challenges of FBG Embedding in Composite Material

In spite of all the dominance and superiority, embedding an FBG in a composite material truly needs some mastery and skills in dealing with the challenges, particularly the delicacy and fragility of the optical fibre. Composite material fabrication consists of two methods, namely hand layup and pre-preg layup (Ramakrishnan et al., 2013). Hand layup method is the most conventional method, where the fibres are plied-up by stacking it one over another, by applying matrix such as resin in between them. Subsequently, the composite materials undergo the curing process. Curing is the polymerization of the matrix where the matrix evaporates and dries up resulting in harder and tougher composites. After the curing process, the composites are shaped into desired specifications. As opposed to hand layup method, a curing process in pre-preg layup is completed by applying heat or pressure. Bag moulding and autoclave moulding are the examples of vacuum moulding for the curing process. Autoclave curing process involves a temperature range of 120 ºC to 200 ºC, with applied pressure of up to 6.89 kPa (Ramakrishnan et al., 2016) as shown in Figure 2.25.

Figure 2.25   Pre-preg layup method

Source: Ramakrishnan et al. (2016).

FBG embedding is more challenging than surface mounting due to the fragility of the optical fibre. However, this does not mean that FBG sensors are impracticable to be embedded. Several researches (Chung & Kang, 2008; Rodrigues, Felix, Lage & Figueiras, 2010) have authenticated this by embedding special FBG transducer in concrete reinforced composites of civil engineering structure, hence vanquishing the argument on FBG sensors embedment. However, precaution such as pre-strain of the optical fibre has to be ensured (Ramakrishnan et al., 2011). This precaution is to avoid bending fibre that results in reflected wavelength distortion or reduction in optical power. Despite precaution, distortions in reflected wavelengths are yet to be significant due to thermal gradients and non-uniform stresses originating from curing and post-curing process (Alfredo et al., 2015). This can be illustrated in a study where 12 FBG sensors were embedded in carbon fibre-reinforced automotive control arm, where the locations were labelled as OF_1 and OF_2 as shown in Figure 2.26.

(a)

(b)
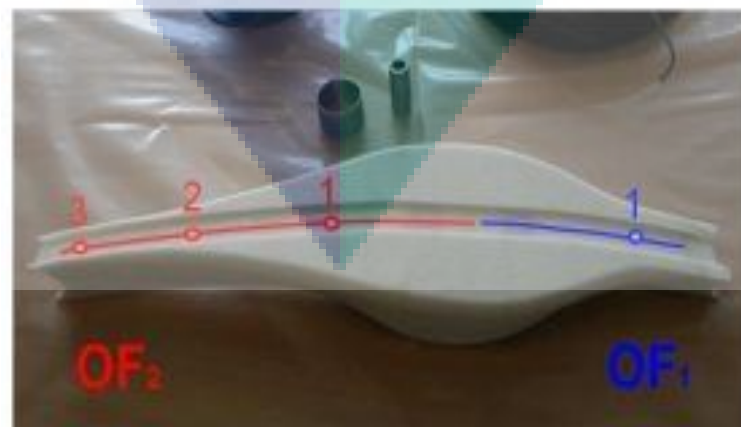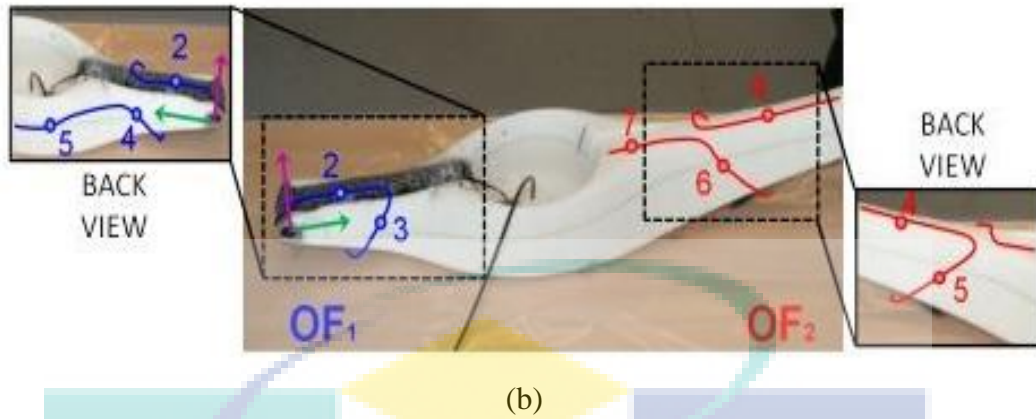
Figure 2.26   Location of the FBG embedment: (a) Front view (b) Back view
Source: Alfredo et al. (2015).

The location, OF_1 was the surface pasted with 12 FBGs, while location, OF_2 was the surface pasted with 7 FBGs. The component was left to be cured at 40 °C temperature at the pressure of 0.5 MPa, and post-cured in an oven for 48 hours at a temperature of 50 °C. The reflected wavelengths from all the FBG sensors were examined, as shown in Figure 2.27, where the wavelengths before embedding were denoted in black, and the orange colour were the wavelengths after embedding.

(a)   (b)
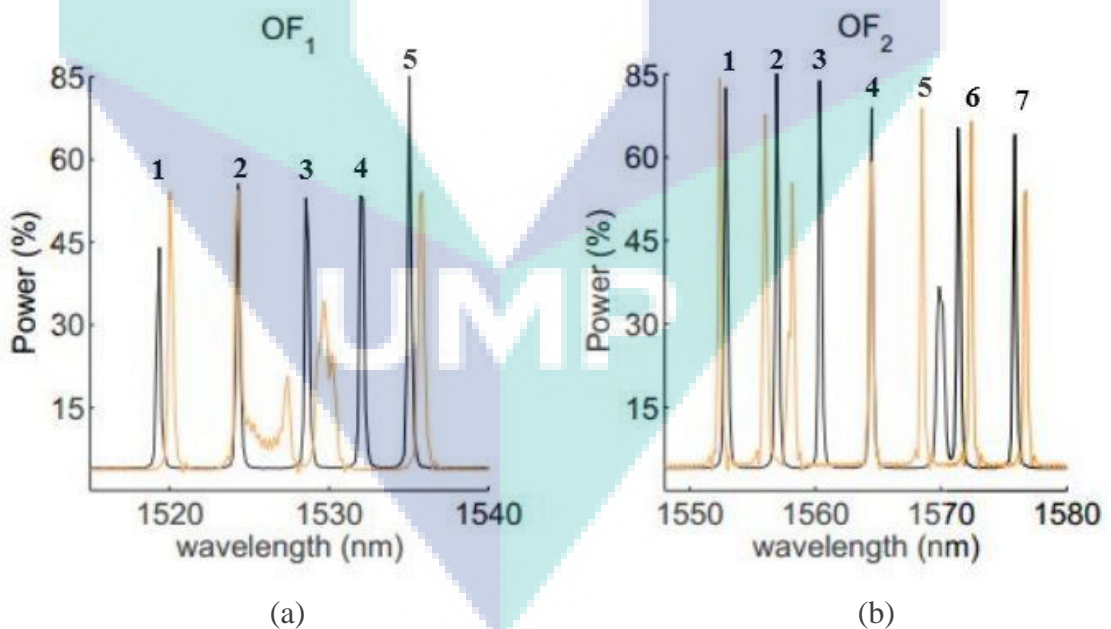
Figure 2.27   Comparison of the reflected wavelength for: (a) OF_1 and (b) OF_2
Source: Alfredo et al. (2015).

From the reflected wavelengths, it was concluded that the third and fourth FBG sensors of OF_1 were distorted due to the resin curing. Significant optical power reduction was

noted on the third FBG, implying that non-uniform stress distribution was acting along the optical fibre. Wavelength peak splitting in the fourth FBG signified the existence of transverse stresses, such as pressure resulted from the curing process. However, other circumstances such as reflectivity of the gratings, splice loss of optical fibre, and power splitter due to the use of coupler could also contribute to the reduction of output optical power (Ling et al., 2006).

Another challenge in FBG embedding is the proper precaution and forethought needed, as careful handling is truly essential due to the ease of breaking of FBG sensor. The ingress and egress of the optical fibre must be safeguarded and secured from any environmental perturbation, as these critical locations are prone to fibre breakage due to the sharp pressure gradient. The most simple and straightforward practice is by sliding the bare optical fibre into a Teflon tube, also known as polytetrafluoroethylene (PTFE) or polyvinylidene fluoride (PVDF), as shown in Figure 2.28 (Kinet et al., 2014).
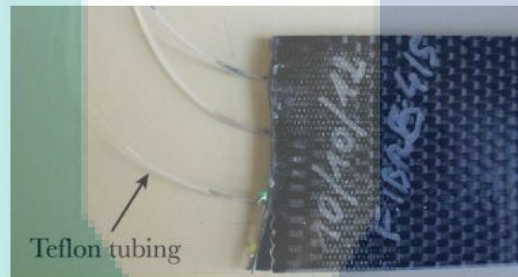
Figure 2.28   Insertion of bare optical fibre in Teflon tube
Source: Kinet et al. (2014).

Another method to strengthen the FBG sensor is by surface mounting to a metal sheath for additional reinforcement (Raffaella, Donati, Troiani & Proli, 2014). One of the promising methods is by embedding the FBG sensor alongside the connector, at the egress of the optical fibre, into the composite (Ramakrishnan et al., 2016), as shown in Figure 2.29. However, such method has a shortcoming, as the composites will become brittle and devastating away at the edge.

The complication and difficulties in trimming and cutting the ingress and egress of the optical fibre can be another challenge without the proper organization of the embedded optical fibre, where the egress of the embedded FBG is positioned at the edge of the composite.

Figure 2.29   Embedded connector inside the composite together with optical fibre
Source: Ramakrishnan et al. (2016).

The inconvenience and the large size interrogation system make this a hinder in implementing the optical fibre sensors. Thus, a smaller size portable working system is needed to make this structural health monitoring system possible to be implemented without any constraint. Due to this awareness, a small size, compact and lightweight all-in-one transmitter and receiver interrogation unit, with the a dimension of only 160 mm x 116 mm x 35 mm, and a weight of 520 g has been invented as shown in Figure 2.30 (Bram et al., 2012). The interrogation system is more advanced than the conventional interrogation system, with fully wireless transmission over a smartphone or tablet, communicating via RS232/Bluetooth connection to a graphical user interface Android platform.

Front view   Side view
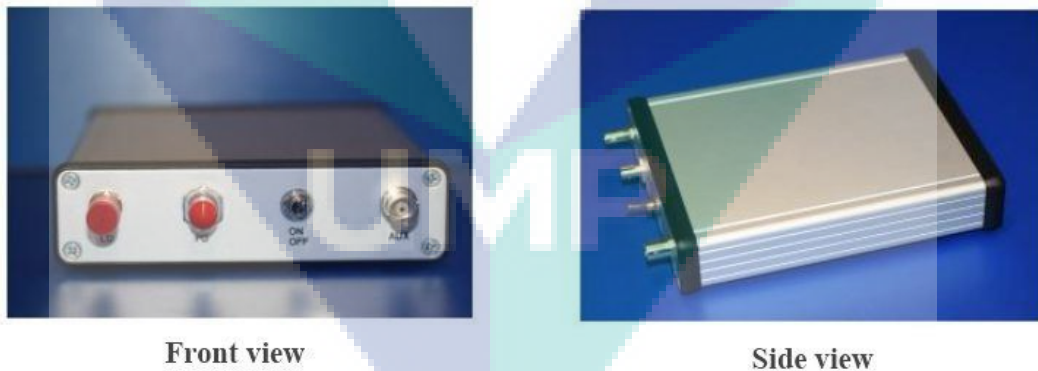
Figure 2.30   Ultra small interrogation system unit
Source: Bram et al. (2012).

2.6   FBG Based Real-Time Monitoring System

From the justification of previous topics, no doubt that FBG has the upper hand over conventional sensors and has become a trend in SHM of not only in composite but also in other structure as well. Enormous impressive real-time monitoring system

39

utilizing FBG sensor has caught the intention of this study to further apprehend about the monitoring system both for static and dynamic strain in leading to the establishment of the smart structure. However, from the critical review of reported work, much endeavour is still needed to bring the FBGs real-time monitoring system to a fully mature readiness level. In this topic, several drawbacks from the reported work have been criticizedin an appropriate way and proposed solutions are being enclosed regarded as opportunities in developing for a more robust FBG based real-time monitoring system.

2.6.1 Static Strain Sensing Real-Time Monitoring System

The adoption of FBG in SHM of real-life engineering structures carved its history in Northern Portugal, when rehabilitation was carried out on centenary metallic bridge known as Eiffel Bridge (Rodrigues et al., 2012). During the rehabilitation, the top and bottom chords of the bridge were load tested with 30.2 tonne road vehicles and a 121 tonne locomotive train. The positions of the mounted FBGs on the bridge's chords are shown in Figure 2.31.
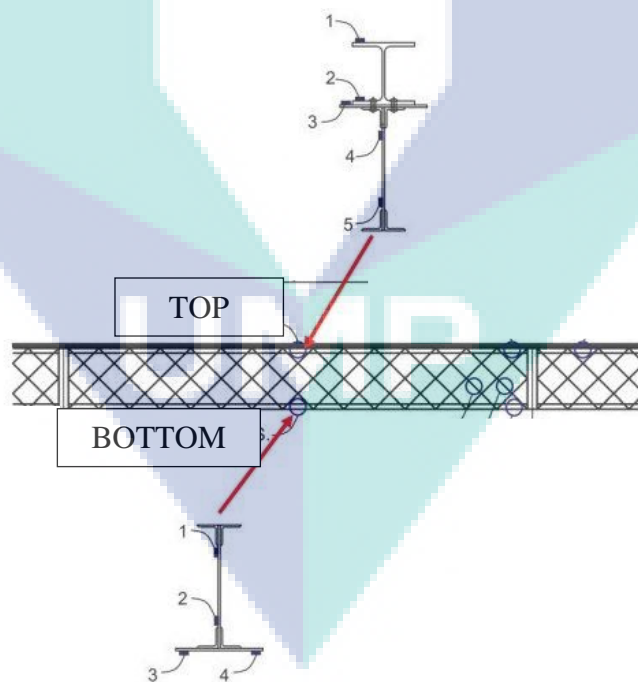
Figure 2.31   FBGs positioning on the top and bottom chords of the bridge
Source: Rodrigues et al. (2012).

From the results of the strain signals captured by the top and bottom FBGs, as shown in Figure 2.32, the signals revealed very convincing results of the structural condition, whether it was in tension or compression.
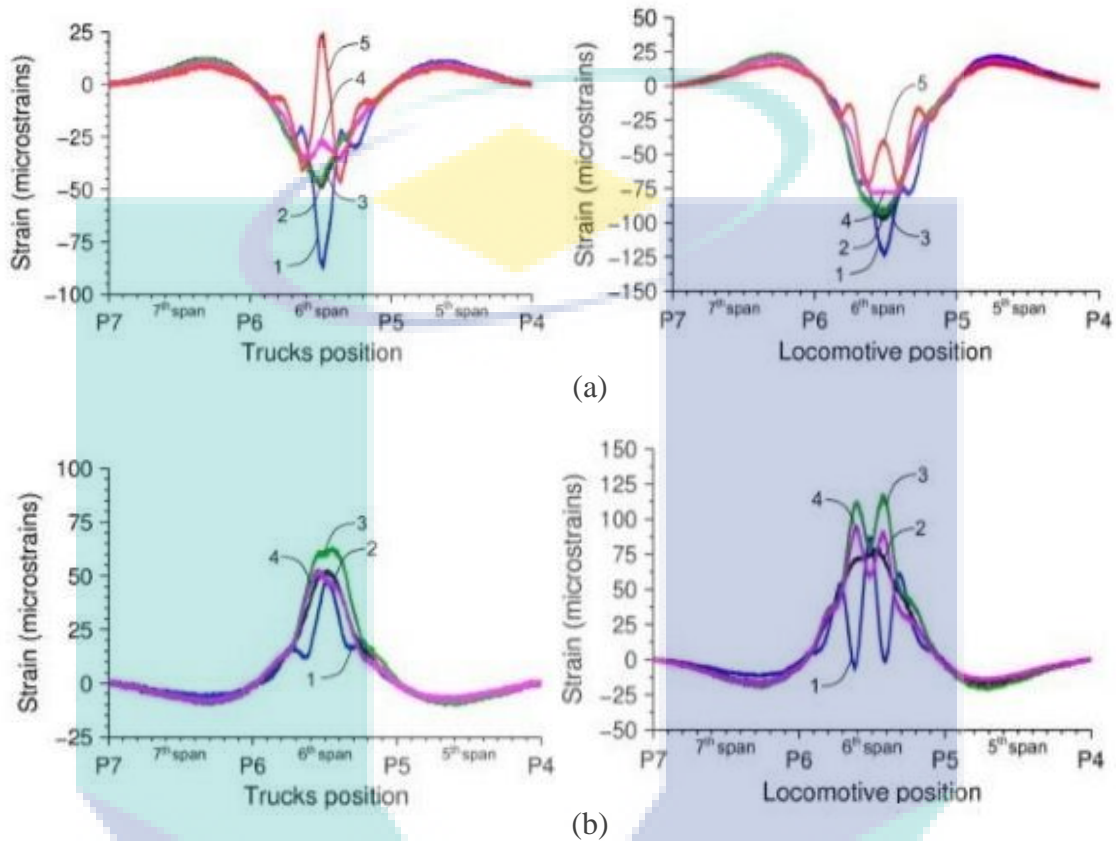
Figure 2.32   Spectrums of FBGs from the load test of trucks and locomotive for (a) Top position (b) Bottom position of the bridge's chord

Source: Rodrigues et al. (2012).

Strain signal for the top position of the bridge's chord showed a negative magnitude of strain, which implied that the structure was under compression. On the other hand, FBGs that were mounted at the bottom of the chord showed a positive strain magnitude which signified that the structure was under tension (Rodrigues et al., 2012).

The potential of FBG in SHM monitoring is not limited to bridge monitoring. Recently, a field test was performed by mounting more than 50 FBGs along 1.5 km underground rail track in Milan metropolitan area(Roveri et al., 2015). The main objective was to investigate the deformation of the railway, and the wear condition of the wheel-rail contact. The test was performed by monitoring the car-passenger train, type MNG M1 "Meneghino", for a period of six months. Figure 2.33 below shows the

results of a six-car passenger train passing through the railway. A one-car passenger train consisted of four axles, thus, from the strain signals, four peaks represented a train, while each peak constituted of one axle of the train.
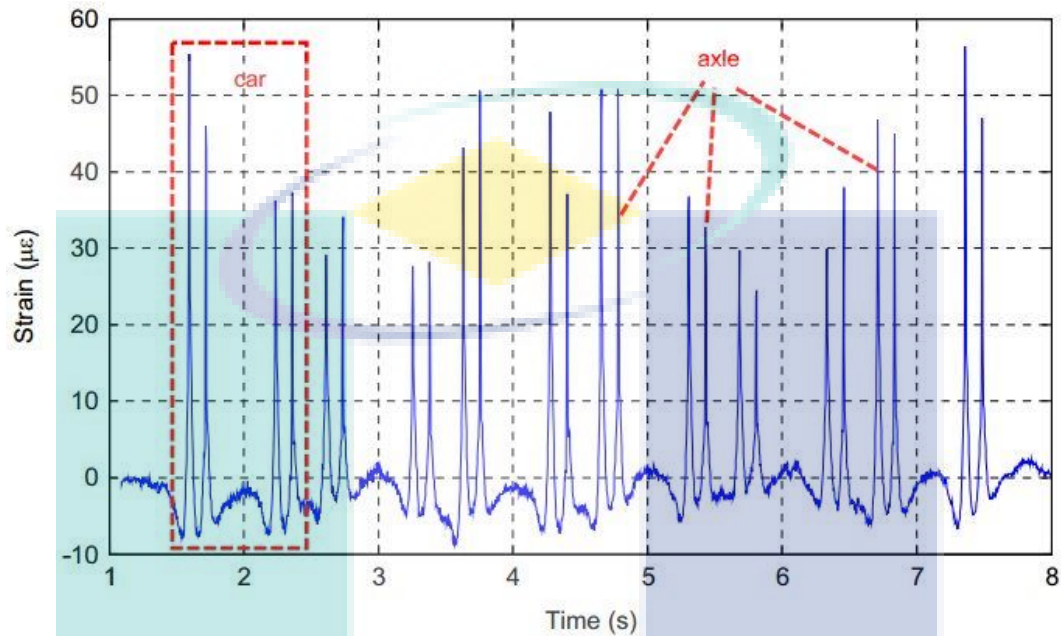
Figure 2.33   Results of a six car-passenger train passes the railway
Source: Roveri et al. (2015).

However, the strain information in the presentation of spectrums requires interpretation from a signal expert in evaluating the structure condition remains as drawbacks for a non-expert end user to self-examine the structure condition. Such spectrum presentation has been a conventional way that is being practiced by other researchers, such as the monitoring of Hong Kong's Tsing Ma bridge (Chan et al., 2006), concrete beam (Moyo et al., 2005), Leziria Bridge in Portugal (Rodrigues et al., 2010), and Luiz I bridge in Portugal (Costa & Figueiras, 2012b). Other researchers studying on the real-time monitoring in railway has also implemented the same method, such as the monitoring of railway in Spain (Filograno et al., 2012) and Trezoi bridge railway in Portugal (Costa & Figueiras, 2012a). The confusion which can lead to error in the desired readings, and the absence of interactive way such as virtual artificial display of the structure, can be brushed-up by implementing the MATLAB graphical user interface (GUI) mesh-grid function.
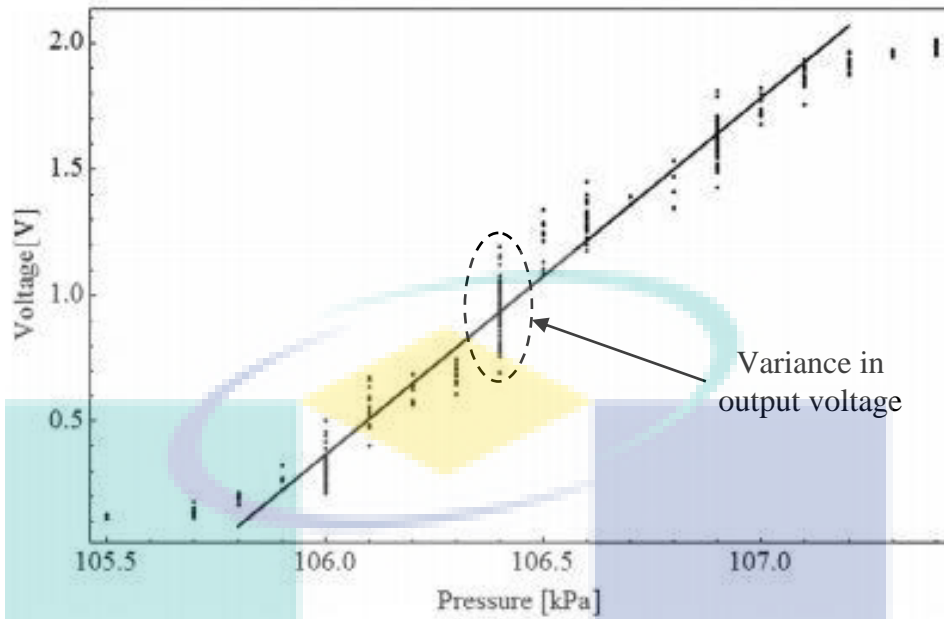
Figure 2.34   Inconsistency of output voltage
Source: Allwood et al. (2015).

Another main challenge in static strain sensing is the inconsistency of output voltage, due to the utilization of photodetector to convert the wavelength intensity demodulation to an electrical voltage signal. This complication has been encountered in several studies (Allwood et al., 2015; J. Ma et al., 2016; P. Ma et al., 2014). The adoption of the edge filter detection interrogation system, in a study onan FBG mounted rubber diaphragm pressure transducer, showed a significant variation of the output voltage, as illustrated in Figure 2.34, which could lead to errors in the desired readings during calibration. High power from the light source can be one of the root causes that results in distorted reflected wavelength, and the formation of unwanted wavelengths presented in the spectrum. Unwanted wavelengths will cause wrong mismatching condition, whereas distorted wavelength with a non-linear edge will produce inconsistency of intensity shift, as the sensing FBG slides across the reference FBG. All these phenomena eventually contribute to the output voltage inconsistency. MATLAB GUI coded with output voltage normalization to reduce the variation in output voltage will be the proposed problem-solver. Normalization analysis has been implemented by the researchers primarily in the field of social science (Ioffe & Szegedy, 2015; Pelz, Molly, Bagby & Sears, 2008; Sboner et al., 2009; Wang & Wei, 2016), which is a technique of designing and redesigning to scale down a redundant database (Stephens, Plew & Jones, 2008), which can be expressed as:

$$V_{norm} = \frac{V_s}{V_r}$$
2.6

where V_{norm} is the ratio voltage normalization of strain voltage, V_s is the voltage reading from the FBG sensor which is subjected to strain. Reference voltage, V_r is the initial voltage from the light source. Substitution of V_{norm} into the calibrated linearity equation can be simplified as:

$$\frac{V_s}{V_r} = m_{avg}\chi + c_{avg}$$
2.7

where m_{avg} is the average gradient of the calibration curve, χ is the independent variable, which is the load induced. The y-intercept of the calibration curve is denoted as c_{avg}.

2.6.2 Dynamic Strain Sensing Real-Time Monitoring System

The examples of dynamic strain sensing are, notably, impact test and natural frequency determination of the structure. Impact, for instance, strikes from the foreign object and tool drops during service are sudden, and the total impact load generates more damage than the gradual discrete static loading, due to the inertia effects that double the actual load. Thus, accurate, reliable and consistent, instant real-time impact localization monitoring system has to be developed. An accurate and reliable monitoring system can improve the damage inspection, which is limited to only a certain specific area, and reduce the time of inspection and maintenance cost. Recently, an NIR-FBG has been utilized in SHM of composites as an alternative to 1550 nm FBG, in monitoring the impact localization on the thin laminated composite plate (Hafizi, Epaarachchi & Lau, 2015). Two impacts were hit at two different locations, which resulted in time delay in one of the sensor's signals, as shown in Figure 2.35. The estimated time delay was substituted in linear source location algorithm for impact location estimation.
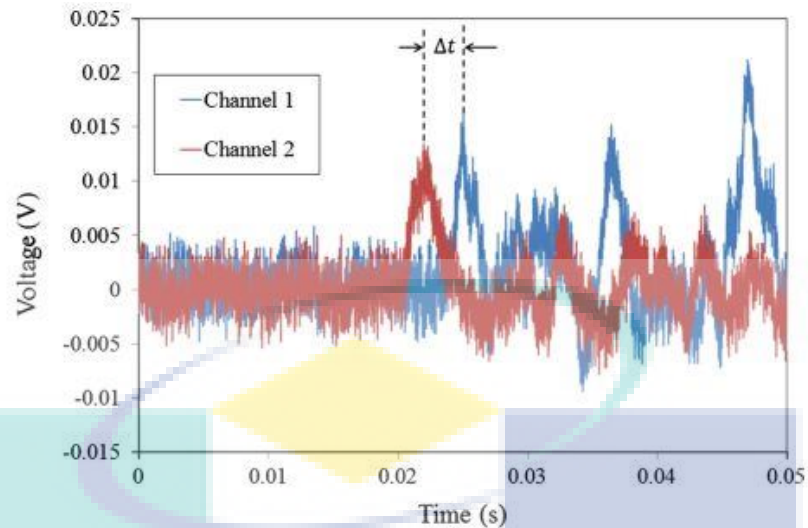
Figure 2.35   Time delay between two FBG signals

Source: Hafizi et al. (2015).

However, the use of bulky size digital storage oscilloscope, as shown in Figure 2.36, for signals logging and post-processing process made the monitoring system time-consuming, non-instant and inefficient for the idealized concept of smart structure.
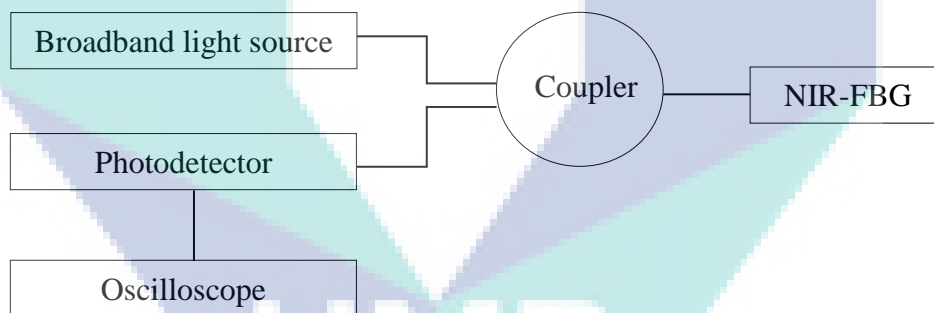
Figure 2.36   Digital oscilloscope used for signal logging process

Source: Hafizi et al. (2015).

Other researchers (Frieden, Cugnoni, Botsis & Gmur, 2012; Fu, Liu, Lau & Leng, 2014) have utilized this expensive signal precision device as well, in impact determination. Another main issue is the presence of high-level noise, resulting in the submergence of significant raw impact signals' peak spectrum, as shown in Figure 2.35, making the estimation of the time of arrival through peak detection, difficult and inaccurate. Several advanced algorithms have been developed for impact localization such as the intelligent artificial neural network (ANN) (Ribeiro, Possetti, Fabris & Muller, 2013), multiple signal classification (MUSIC) (Mingshun Jiang et al., 2016),

wavelet analysis with applied elastodynamics (S. K. Lee & Park, 2011), Kalman filter (Moon, Lee, Shin & Lee, 2011), hyperbolic curve algorithm (Fu et al., 2014) and triangulation method (Kirkby, de Oliveira, Michaud & Manson, 2011).

However, large data sets are required for the estimation process, which was labelled as a shortcoming for these algorithms. Usually, most of the impact localizations are determined through correlation of reflected Bragg wavelength, where expensive high-speed interrogation systems are used in capturing the spectrum (M. Jiang et al., 2015; Lu et al., 2015). Reflected Bragg wavelength is utilized for correlation in impact determination due to its low level of uncertain noise compared raw impact voltage signal. However, cross-correlation algorithm can be implemented in reducing the uncertain noise of raw impact voltage signal, which is then used for correlaten for the time of arrival estimation. The explanations about the cross-correlation approach and practice in FBGs sensing system are being detailed in the subtopic below.

2.6.2.1   Cross-Correlation Approach with Linear Source Location Technique

The impact induced on a structure will result in seismic raw impact signal arriving at a particular time when captured by a distributed sensor. This difference in time of arrival can be obtained by calculating the peak differences of both the peak spectra. Several algorithm can be utilized to obtain the time of arrival, such as autocorrelation algorithm (Caucheteur et al., 2004), centroid detection algorithm (CDA) (Askins et al., 1995), least square method (LSQ) (Ezbiri et al., 1998) and cross-correlation algorithm (C. Huang et al., 2007). Among these algorithms, cross-correlation approach demonstrats a good performance in suppressing uncertain noise (W. Huang et al., 2014; Qingwen et al., 2011; Wenzhu et al., 2015). Cross-correlation algorithm functions by searching for the maximum peak of the two signals, and estimates the time delay (Ianniello, 1982; Sun, Jia, Du & Fu, 2016). The mathematical model of the samples domain signals captured by both the FBGs $x_0(s)$ and $x_1(s)$ can be expressed as (Ianniello, 1982):

$$x_0\,(s) = z\,(s) + n_1\,(s) \qquad\qquad 2.8$$

$$x_1\,(s) = z\,(s\text{-}D) + n_2\,(s) \qquad\qquad 2.9$$

where $z(s)$ is the significant signal uncorrelated with noise, $n_1(s)$ and $n_2(s)$. Cross-correlation of both the signals, Rx_0x_1 with mathematical expectation, M over the argument τ for samples delay, D can be expressed as (Ianniello, 1982):

$$Rx_0x_1(\tau) = M[x_0(s)x_1(s\text{-}\tau)] \qquad 2.10$$

Windowed cross-correlation was then computed to estimate the difference of the two spectrums to determine the samples delay, D by intergration given by (Ianniello, 1982):

$$Rx_0x_1(\tau) = \frac{1}{S-\tau}\int_{\tau}^{S} x_0(s)\, x_1(s-\tau)ds \qquad 2.11$$

where s is the window's size which is the observation interval, and in the condition that estimation of D by maximizing equation 2.10 over τ. Sampling period, T_s which is the time between two sampling points has to be determined, since the delay is in samples difference, D where it is the inverse of the sampling frequency, F_s, expressed as:

$$F_s = \frac{1}{T_s} \qquad 2.12$$

The time difference, $\varDelta t$ in terms of the sampling period, T_s and samples difference, D can be modelled as:

$$T_s = \frac{\varDelta t}{D} \qquad 2.13$$

Substituting equation 2.12 into equation 2.13 yields the time difference, $\varDelta t$, defined as:

$$\varDelta t = \frac{D}{F_s} \qquad 2.14$$

The cross-correlation algorithm has been testified successfully in monitoring the water traffic at Hudson river, United States (Fillinger, Sutin & Sedunov, 2009). The authors utilized several hydrophones in capturing the acoustic signal noise produced by the vessels. Due to the contrasting distance of propagation, the underwater acoustic signal reached the hydrophones at different time delay. The estimation of the delay was further performed through cross-correlation algorithm, as shown in Figure 2.37. From the

illustration, cross-correlation algorithm suppressed the noise and amplified the two peaks for time delay estimation.
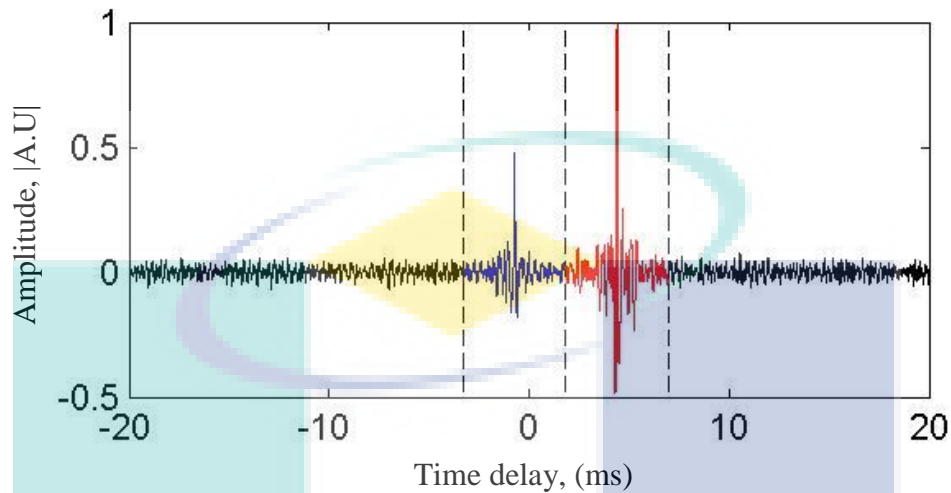
Figure 2.37   The cross-correlation algorithm from two different vessels
Source: Fillinger et al. (2009).

Other than that, the cross-correlation algorithm has been applied excessively in medical field, particularly ultrasonic imaging for time difference estimation (Walker & Trahey, 1995). In the field of FBGs, cross-correlation algorithm has been commonly adopted to estimate the time delay of Bragg wavelength shift between the sensing and the reference FBG (Bao, Yuan, Dong, Song & Xue, 2013; Lamberti, Vanlanduit, De Pauw & Berghmans, 2014; Takashima, Asanuma & Niitsuma, 2004). Recently, cross-correlation has been utilized in estimating the frequency difference between two demodulated signals, for monitoring the crustal deformation (Q. Liu, He & Tokunaga, 2015) Thus, with the evidence of previous recent works, it has been shown that cross-correlation algorithm has adequate capability in estimating the time difference between two demodulated signals.

From the estimated time difference of the two signals, linear source location technique can be used for impact estimation. This technique is an acoustic emission (AE) method used to determine the time arrival of AE waves received at two sensors, provided that the impact is within or between the two sensors (Aljets, Chong, Wilcox & Holford, 2010), as illustrated in Figure 2.38.
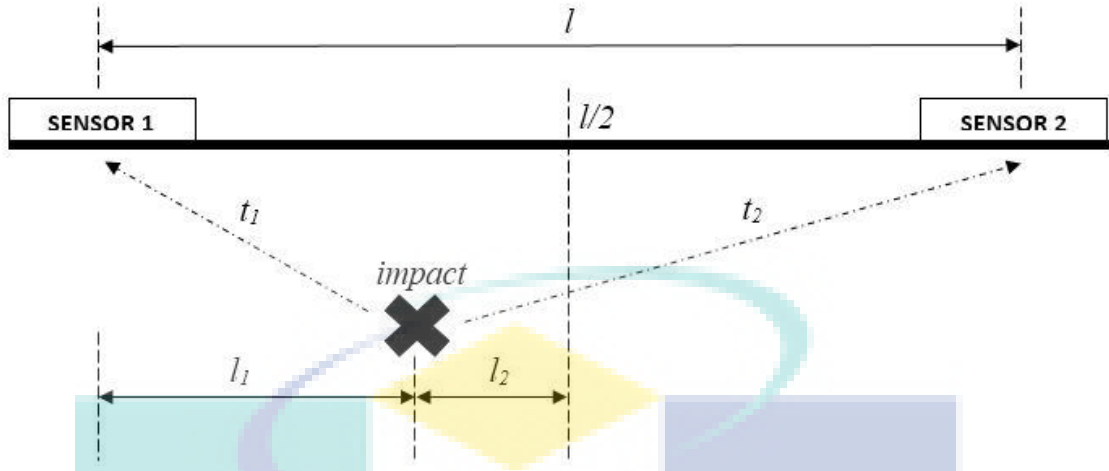
Figure 2.38   Illustration of linear source location technique for impact detection
Source: Khan et al. (2014).

The signal with the highest amplitude, or the signal of the first arrival indicates that it is the nearest impact induced to that sensor, which can be formulated as (Khan, Sunichi & Hasan, 2014):

$$l_2 = \frac{1}{2}(t_1 - t_2).C_g = \frac{1}{2} \Delta t.C_g \qquad\qquad 2.15$$

$$l_1 = \frac{1}{2} l - l_2 = \frac{1}{2} (l - \Delta t.C_g) \qquad\qquad 2.16$$

where l is the distance between two sensors, l_1 and t_1 is the distance and time from the nearest sensor while l_2 and t_2 is the distance and time from the second sensor, and C_g is the group velocity of the waves. CC-LSL can be obtained by substituting equation 2.14 into equation 2.16 to determine the impact, l_1, finalized as (Khan et al., 2014):

$$l_1 = \frac{1}{2} (l - \frac{D\,(s)}{F_s}.C_g) \qquad\qquad 2.17$$

Thus, CC-LSL which functions entirely in real-time, will definitely improve the current dynamic strain sensing monitoring system for impact detection. The relative percentage of error with respect to the total length of the structure, L can be can be expressed as (Hafizi et al., 2015):

$$Relative\ error\ (\%) = \frac{(I_E + L) - (I_A + L)}{I_A + L} \qquad\qquad 2.18$$

49

where I_E is the estimated impact distance, and I_A is the actual impact distance. Another essential determination in dynamic strain sensing is the natural frequency of the structure itself. Failure of a structure is not wholly due to fatigue damage, but also due to the approach of the excitation frequency on the natural frequency of the structure (Ling et al., 2006), for instance, the impact of earthquakes on civil structures. Thus, the natural frequency mode of a structure must be determined instantly in real-time.

Structures undergo dynamic vibration have always associated with complex conditions. Therefore, finite element theoretical analysis have to be performed in order to determine the condition of the structure. Natural frequency determination are one of the significant analysis. Gu et al. (2001) proposed a meshless local Petrov-Galerkin (MPLG) method in analyzing the free and force vibration of a cantilever beam. The proposed method are compared with commercial FEM software, Abaqus and node-by-node meshless method. As a results, the proposed meshless method for analysis are more flexible in determining free and forced vibration analysis (Gu & Liu, 2001). In another study by Kim et al. (2003), the authors performed an FEA analysis on three bridges with Abaqus as a validation with the frequencies captured by accelerometer. The intention of this study is to determine the effect of vehicle's mass on the vibration of the bridge (Kim, Jung, Kim, Kwon & Feng, 2003). Brown (1997) has performed a study by comparing the Nastran and Abaqus FEA software in performing frequency analysis for turbine engine. As a results, Abaqus are more economical, consistent and accurate for frequency analysis as compared to Nastran (Brown, 1997).

2.7   Chapter Summary

The advantages of composite material have truly been towering over the conventional metallic material, especially the great strength of the material with much lesser weight than the conventional material. Industries such as civil structures, aerospace engineering, automotive industries, and sports utilities have been emerging in the use of composite, with the rate increasing greatly from year to year. The forecasted demand of the composite was predicted to reach 140000 tonnes in the year 2020, with the transaction of $48.7 billion sales, making the United States and Europe the biggest countries in producing composite material, followed by Japan. However, this proclamation does not make composite material a durable material that is invulnerable to any damages. Composites have low toughness due to their anisotropic properties,

which can lead to sudden catastrophic damage. The knowledge of this danger has triggered researchers mainly in SHM to find an adequate inspection method or sensor that is capable of detecting the flaw in the composite structure.

In the late 20th century, the development of optical fibre technology has caught the attention of various SHM researchers, to develop an optical fibre sensor that is capable of being embedded in composite structures and provides an in-situ online monitoring system. Since then, FBG optical fibre sensor has great dominance over traditional inspection methods, such as ultrasonic testing, thermography, radiographic testing, AE inspection, and electrical strain gauge sensor. In order for this optical fibre sensor to function, working systems known as interrogation systems are needed, which come in various configurations and involve utilization of certain components. Out of all methods, the edge filter detection method is the most simple and economic method.

Despite the advantages, a critical review found current monitoring system utilizing FBG sensor to be associated with several drawbacks, both in static and dynamic strain sensing which was identified to be the gap of this research. The lack of interactive way in representing the strain deformation of the structure could lead to confusion and error in interpretation, as signals in the form of spectrums limit the monitoring to only signal processing experts. MATLAB GUI with mesh-grid function, as a virtual artificial display of the structure for real-time deformation monitoring, is the proposed solution for this drawback. On the other hand, the ratio voltage normalization algorithm is proposed to solve the inconsistency of output voltage, as photodetector was utilized for light signal conversion to electrical strain signal. For the improvement of the dynamic strain monitoring system, the CC-LSL algorithm has been developed for better impact localization estimation. FFT has also been entailed in determining the natural frequency of the structure.

CHAPTER 3

METHODOLOGY

3.1   Organization of the Experimental Planning

After the gap of this research study has been determined, several solutions consisting of certain functions and algorithms have been proposed. Thus, experimentation based on the proposed solutions have been carried out to test the hypothesis in order to overcome the obstacles of the current real-time monitoring system. In general, two specimens had been fabricated. One specimen was in the form of a plate that could be used to represent the structural body of a bridge or the wings of an aircraft. On the other hand, an industrial dimension size of GFRP beam was fabricated in order to prove that the proposed real-time monitoring system could be applied in composite structures regardless of size and shape. The specimens then underwent two experimental analysis namely static strain and dynamic strain. For static strain experimentation, the specimens were applied with gradually increasing discrete load, starting with no load to a maximum of 50 N. MATLAB GUI inlay with mesh-grid function was used to observe the real-time deformation of the specimens at the increment of every 10 N loadings. Next, with the same experimental procedure, a voltage normalization algorithm was inserted into the GUI monitoring system, and the change of voltage with the desired load induced values was recorded in the hypothesis that the variation of output voltage had been reduced, making the estimation close to the desired load induced without any pre-calibration. For the dynamic strain experimentation, the specimen was induced with impact test at two different points, labelled as impact A and impact B. Cross-correlation with linear source location algorithm was coded in MATLAB GUI, in the hypothesis that the estimated hit would be close to the actual hit, with the percentage of error of less than 10 %. A set of impacts was hit at point C to excite the whole natural frequency of the structure. The

natural frequency captured by the FBG sensor was validated with commercial acoustic emission (AE) sensor and theoretical Abaqus simulation. All the data validation was expected to fall within the acceptable range of percentage of error, which is less than 10 %. For a brief review of the overall experimental procedure, a flow chart representing the summarization of the experimental steps is illustrated in Figure 3.1.
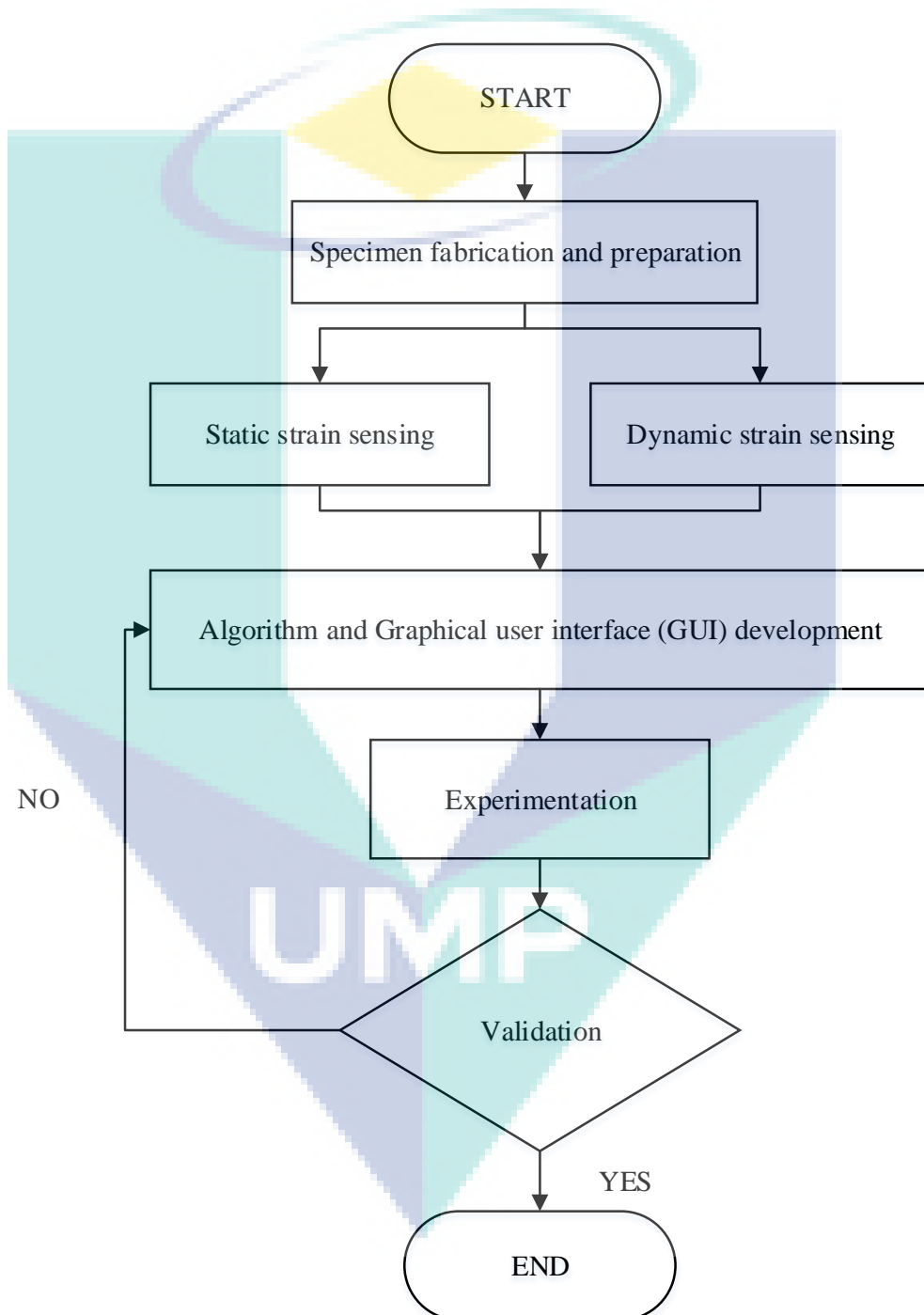
Figure 3.1   Flow chart of the overall experimental procedure

3.2   List of Components and Equipment Adopted

As explained in the earlier chapter, FBG is an indirect sensor which needs a set of hardware components and equipments to function. Low-cost edge filter interrogation had been utilized throughout the whole experimentation, which relay components such as light source, optical circulator, optical coupler, splitter, photodetector, optical spectrum analyzer and data acquisition system. The specifications and details of working principles for each components are explained in subtopics below.

3.2.1   Light Source

The light source is a transmitting device used to emit a certain wavelength of light to illuminate the FBG sensor. Throughout the whole experimentation, amplified spontaneous emission (ASE) broadband light source was adopted as shown in Figure 3.2.

Figure 3.2   Amplified Spontaneous Emission (ASE) light source
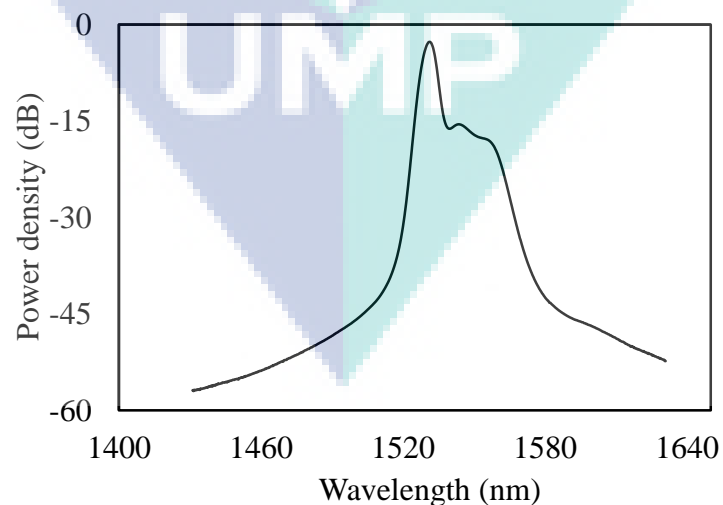
Figure 3.3   Operating wavelength range of the light source

The small size source with a dimension of only 10 cm x 7 cm x 2 cm (length x width x height), emits a broadband light signal in the wavelength range of 1431 nm to 1631 nm, as shown in Figure 3.3. The light signal has a centre wavelength of 1531 nm, recorded at a low-pass filter video bandwidth (VBW) of 1000 Hz and a resolution of 0.2 nm. Table 3.1 shows the specifications of the light source.

Table 3.1   Specifications of the ASE light source

Parameters	Specification
Type	Amplified Spontaneous Emission (ASE) broadband light
Dimension (length x width x height)	10 cm x 7 cm x 2 cm
Wavelength range	1431 nm - 1631 nm
Centre wavelength	1531 nm

3.2.2   Optical Circulator

An optical circulator is used to separate and channel the light signal from one port to another port. 3-port (15-PICIR-3-SCL-1) optical circulator operating at 1550 nm as shown in Figure 3.4 was used in this experimental work. Light emitted from the port 1 (red) is conveyed into port 2 (blue) which is connected to FBG sensor. Reflected Bragg wavelength from the FBG sensor is circulated into port 3 (white) which is connected to the photodetector, OSA or any spectrum analyzer signal precision device. Insertion loss which is the loss of signal power due to insertion such as poor connectors or plugs is 0.79 dB from port 1 to port 2 and 0.71 dB from port 2 to port 3. Polarization dependent loss (PDL) which is the measure between peaks difference expressed as maximum and minimum loss in decibels are 0.04 dB from port 1 to port 2 and 0.03 dB from port 3 to port 4. Return loss which is the loss of the signal reflected back to the device is 55 dB. Handling power of the circulator is 500 mW with a range of operating temperature at 0 ºC to 70 ºC. Full specifications of the optical circulator are shown in Table 3.2.

Figure 3.4   3-port optical circulator

Table 3.2   Specifications of the optical circulator

Parameters	Specification
Operating wavelength	1550 nm
Number of port	3
Insertion loss	0.79 dB (port 1 to port 2)
	0.71 dB (port 2 to port 3)
PDL	0.04 dB (port 1 to port 2)
	0.03 dB (port 2 to port 3)
Return loss	55 dB
Power handling	500 mW
Fibre length	0.5 m
Type of connector	FC/PC
Operating temperature	0-70 ºC

3.2.3   Optical Coupler

The optical coupler is used to split the single input light source transmitter into multiple output receivers. A 2 x 2, 4-port optical coupler (CS-5250-S115-03) single mode fibre cable was used in this experimental work as shown in Figure 3.5. The total length of the fibre was 1.5 m with a diameter of 250 μm, operating at 1550 nm wavelength. The coupling ratio of the two output ports is 50.95 % and 49.05 % respectively, with the insertion loss of 3.06 dB and 3.22 dB at each port. The specifications of this optical coupler are shown in Table 3.3.

Figure 3.5   2x2, 4-port optical coupler

Table 3.3   Specifications of the optical coupler

Parameters	Specification
Operating wavelength	1550 nm
Number of port	4
Fibre length	1.5 m
Fibre diameter	250 μm
Fibre type	SMF-28
Coupling ratio	50.95 % (port 3)
	49.05 % (port 4)
Insertion loss	3.06 dB (port 3)
	3.22 dB (port 4)

3.2.4 Optical Splitter

The optical splitter is a device with the same function as optical coupler, which is to divide the single input channel into multiple output channels. A 1550 nm, 1 x 8 optical splitter (OFC-CPIxN-034C) was used in this experimental research study, as shown in Figure 3.6. The hardware device consists of 1 input channel for connection to light source, and 8 output channels for connections to FBG sensors. The maximum insertion loss of the device is 10.2 dB with polarization dependent loss (PDL) of 0.55 dB. Table 3.4 shows the specifications of the optical splitter.

Figure 3.6   1 x 8 optical splitter

Table 3.4   Specifications of the optical splitter

Parameters	Specification
Operating wavelength	1550 nm
Number of input port	1
Number of output port	8
Max. Insertion loss	10.2 dB
PDL	0.55 dB

3.2.5 Photodiode or Photodetector (PD)

A photodiode or photodetector (PD) is a small device which consists of a p-n junction to convert the light photons into currents to be read by any data acquisition device. Since the experiment fully utilized single mode 1550 nm long wavelength of light source, Thorlabs InGaAs PDA10CS-EC photodetector was used in this experimental work, as shown in Figure 3.7. The photodetector has a signal to noise ratio (SNR) setting of 0 to 70 dB, with an output connection through a Bayonet Neill-Concelam (BNC) cable. The fast sensing speed with low dark current noise, and operating temperature of 0 to 40 ºC make the PD suitable for dynamic sensing as well

as static sensing measurement. The specifications of photodetector are shown in Table 3.5.
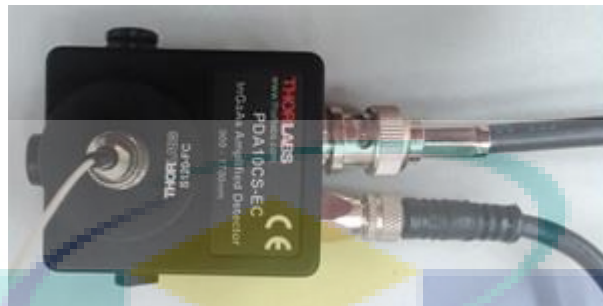
Figure 3.7   Thorlabs InGaAs photodetector

Table 3.5   Specifications of Thorlabs InGaAs photodetector

Parameters	Specification
Material	InGaAs
Wavelength range	900 nm to 1700 nm
Peak wavelength	1550 nm
SNR setting	0 - 70 dB
Sensing speed	High
Dark current	Low
Operating temperature	0 to 40 ºC
Output connection	BNC cable

3.2.6   Optical Spectrum Analyzer (OSA)

Optical spectrum analyzer, or commonly acronymed as OSA, is a precision instrument used to measure the power intensity of the optical signal over a specific range of wavelength. Bayspec (FBGA-F-1525-1565-FP) optical spectrum analyzer was used in this experimentation as shown in Figure 3.8. The OSA operates at a C-band wavelength range of 1525 nm to 1565 nm, with the wavelength accuracy of ±30 pm, and display spectral resolution of ±1 pm. The total dimension of the component is only 96 mm x 68 mm x 15.8 mm (length x width x height), connected via USB cable for output data, utilizing BaySpec Sense 2020 operating software with a sensing speed up to 0.2 kHz. The specifications of OSA is shown in Table 3.6.

Figure 3.8   Bayspec optical spectrum analyzer (OSA)

Table 3.6   Specifications of Bayspec optical spectrum analyzer

Parameters	Specification
Wavelength range	1525 nm - 1565 nm
Wavelength accuracy	$\pm$ 30 pm
Display spectral resolution	$\pm$ 1 pm
Sensing speed	0.2 kHz
Output connection	USB cable
Operating software	BaySpec Sense 2020

3.2.7   National Instruments NI-9234 Data Acquisition Device

Data acquisition device is needed to acquire variable data from the photodetector. In this experimentation, the National Instruments model NI-9234 data acquisition device, as shown in Figure 3.9, was used in data attaining and recording. The device has a maximum of 4 channels, with a connection to BNC cable, and each channel has a maximum sampling rate of 51.2 kHz. Both AC and DC coupling are available on this device, making it suitable for static and dynamic measurement with 24-bit resolution at an operating temperature of -40ºC to 70ºC. The maximum operating power of this device is $\pm$ 5V. Table 3.7 summarizes the specifications of the data acquisition device.

Figure 3.9   National Instruments NI-9234 data acquisition device

Table 3.7   Specifications of National Instruments NI-9234 data acquisition device

Parameters	Specification
Number of channels	4
Type of coupling	AC/DC
Maximum sampling rate	51.2 kHz
Resolution	24-bit
Operating temperature	-40ºC to 70ºC
Operating power	±5V
Output connection	BNC cable

3.2.8   Acoustic Emission (AE) Broadband Sensor

Acoustic emission (AE) broadband sensor (Score Dunegan SE2MEG-P) which is a commercial sensor, as shown in Figure 3.10, was used for data validation with FBG sensor. AE sensor has the working principle of detecting the irreversible changes of a structure through wave propagation. The sensor has a good sensitivity of up to 2 MHz, with a small physical dimension of 12.5 mm x 13.8 mm (diameter x height), and weighs only up to 7 grams. Besides, the sensor also has a huge range of operating temperature, from -50ºC to 100ºC. Table 3.8 shows the specifications of the sensor.

Figure 3.10   Acoustic emission (AE) broadband sensor

Table 3.8   Specifications of the acoustic emission (AE) sensor

Parameters	Specification
Diameter	12.5 mm
Height	13.8 mm
Weight	7 grams
Sensitivity	2 MHz
Operating temperature	- 50 ºC to 100 ºC

3.3   Specimens Fabrication

A total of two specimens have been fabricated, which are a composite plate and a GFRP composite beam. The composite plate consists of a ten layer woven fibreglass, as shown in Figure 3.11(a). The ten piece fibreglass was cut into a dimension of 40 cm

x 40 cm (length x width), and laminated with a hand lay-up method using glycidyl (GL) epoxy, and hardener as a resin with a ratio of 2:1, as shown in Figure 3.11(b). The sample was left to cure at room temperature, and Figure 3.12 shows the cured composite plate with a thickness of 0.8 cm.

(a)   (b)
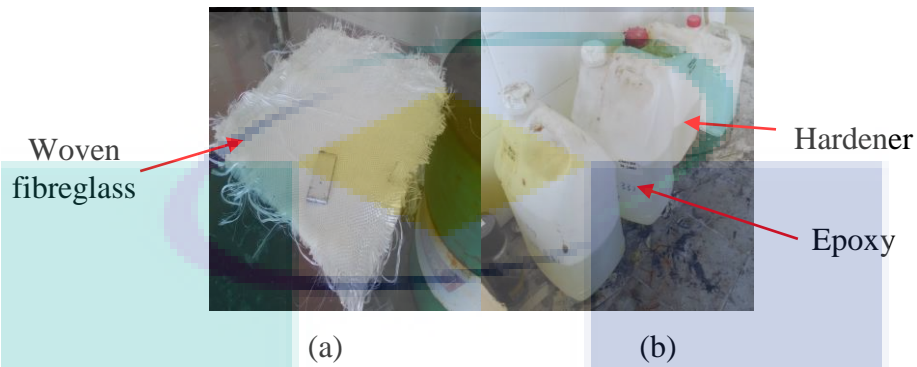
Figure 3.11   Specimen fabrication materials: (a) Woven fibreglass (b) Epoxy and hardener as resin

Figure 3.12   Cured sample of the composite plate

A single 1544.850 nm FBG sensor with 99.9 % reflectivity was embedded inside the composite between the 9th and the 10th layer, and was positioned at the centre of the plate. Table 3.9 shows the physical properties of the composite plate.

Table 3.9   Physical properties of the composite plate

Physical properties	
Mass	1981.5 g
Length	40 cm
Width	40 cm
Thickness	0.8 cm
FBG wavelength	1544.850 nm

For the composite beam, an industrial dimension GFRP beam obtained from Zhengzhou Yalong Pultrex Composites Co., Ltd (en.ylfrp.com) was fabricated with the same method as the composite plate. First, a 120 cm x 90 cm polystyrene foam board, as shown in Figure 3.13(a), was cut into the desired dimension of the beam, which was

100cm x 6.5cm x 3.1cm x 0.4cm (length x width x height x thickness) to form a mould, as shown in Figure 3.13(b). A woven fibreglass was cut into a dimension of 100cm x 100cm (length x width), as shown in Figure 3.14(a), and was wrapped around the mould until the desired thickness of 0.4 cm was achieved. Figure 3.14(b) shows the cured specimen of the beam.

(a)   (b)

Figure 3.13   Mould forming process: (a) Polystyrene foam (b) Mould of the beam

(a)

(b)
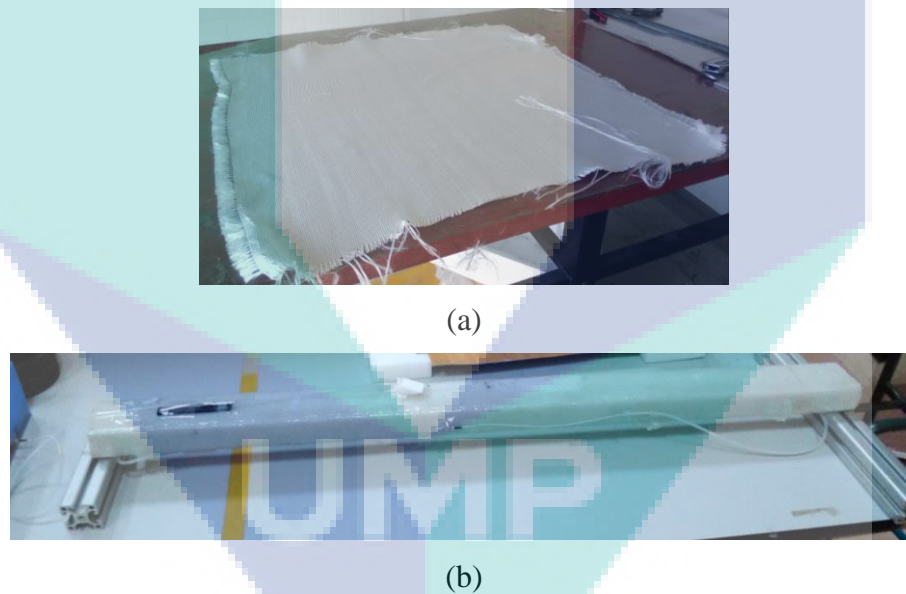
Figure 3.14   Composite beam fabrication: (a) Woven fibreglass (b) Cured sample of the GFRP beam

Two FBGs, where one of them with the wavelength of 1550.441 nm was embedded inside the composite, 19.5 cm away from the edge of the beam, and was positioned at the top of the beam. The second FBG with the wavelength of 1550.219 nm was positioned 30 cm away from the first FBG. The physical properties of the GFRP beam are shown in Table 3.10. Both of the specimens have the obtained mechanical

properties as shown in Table 3.11 which is within the standard range of mechanical properties as stated in composite materials handbook (Lubin, 2013).

Table 3.10   Physical properties of the GFRP beam

Physical properties	
Mass	1158.5 g
Width	6.5 cm
Height	3.1 cm
Thickness	0.4 cm
Length	100 cm
FBG 1 wavelength	1550.441 nm
FBG 2 wavelength	1550.219 nm

Table 3.11   Mechanical properties of both the specimens

Mechanical properties	
Exx = Eyy	417 MPa
Ezz	43 MPa
Vyx = Vxy	0.075
Vyz = Vxz	0.4693
Gxy	27 MPa
Gyz = Gzx	12 MPa
ρ	1100 kg/m^3

3.4   Overall Static Strain Sensitivity Test Experimental Set-Up

Overall static strain sensitivity was performed in order to determine the gradual static sensitivity of the single mode silica glass with 1550 nm optical fibre sensor used in this experimental study. This experiment was also carried out to determine the limit and the maximum capability of the FBG sensor for static strain measurement, before further experimentation was performed. The FBG sensor with a wavelength of 1545.839 nm was surface pasted on a flat dog-bone aluminium tensile specimen. The specimen had an overall length of 200 mm, a gauge length of 75 mm, a width of 13 mm, and a total thickness of 3 mm, as shown in Figure 3.15. The specimen, with a surface attached FBG sensor, underwent tensile elongation test with an Instron 3369 that has a maximum applied force of up to 50 kN.

Figure 3.16 shows the experimental set-up where the specimen was subjected to gradually increased loading until a point where the specimen broke. The strain elongation of the specimen, and applied loading were recorded for further analysis.

Single FBG interrogation system with the utilization of OSA was used to record the reflected Bragg wavelength.
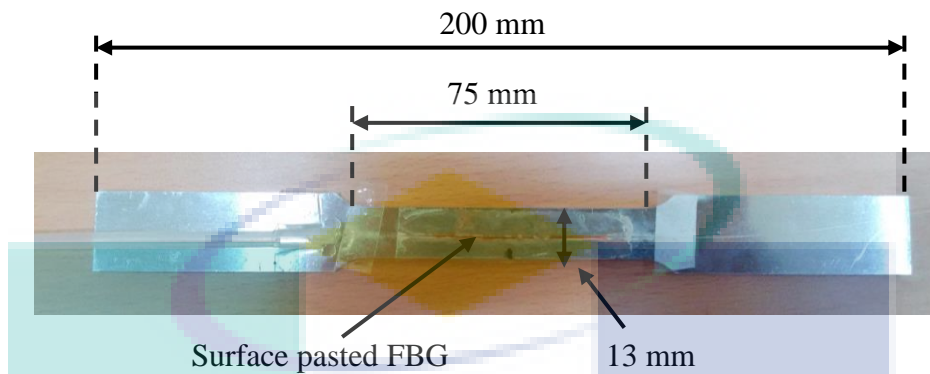
Figure 3.15   The dog-bone aluminium tensile specimen with surface pasted FBG sensor

(a)   (b)
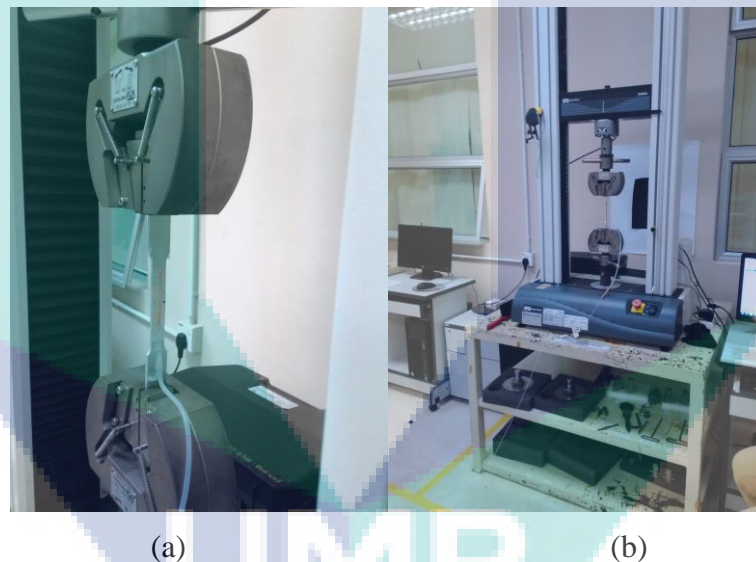
Figure 3.16   The overall static strain sensitivity experimental set-up: (a) Gripping of the specimen on the machine (b) The Instron 3369 50 kN tensile test machine

3.5   Static Strain Sensing Experimental Set-Up

For improvement on the static strain sensing monitoring system, mesh-grid function and voltage normalization algorithm experimentation were carried out. Both the plate and beam underwent the mesh-grid experimentation. The composite plate was clamp fixed at four edges between two tables, with a weight support stand being positioned in the middle of the plate for consistent and equivalent weight distribution, as shown in Figure 3.17 (a). A 10 N load and a 20 N load, as shown in Figure 3.17 (b), were induced on the composite plate, starting from no load to a maximum of 50 N.

Weight support stand   Clamped fixed   20 N   10 N

(a)   (b)
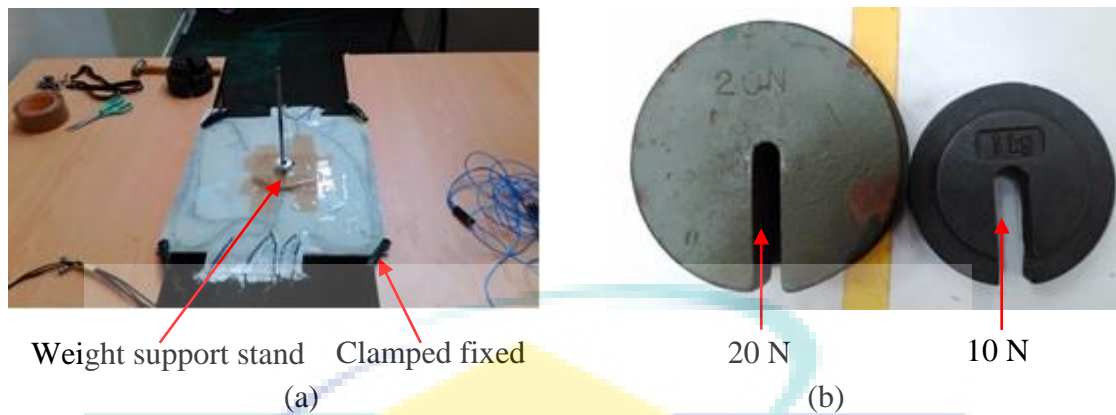
Figure 3.17   Experimental set-up: (a) Fixed edges of the composite plate, and position of the weight support stand (b) Loads of 10 N and 20 N

MATLAB GUI real-time monitoring system programmed with mesh-grid function, with a scaling of -10 to 10 in x and y-axis, and 0 to -100 in z-axis of artificial sample elements with four fixed edges represented the virtual display of the plate. The full display of the GUI and the coding can be referred in Appendix A. The change in voltage readings, and the estimated weights detected by the plate were recorded. The virtual deflection of the plate was observed based on the change of voltage reading. This mesh-grid function has also been experimented on the GFRP beam with the same experimental procedure in order to prove that the proposed monitoring system was capable to function regardless of size and shape. The two ends of the beam were clamp fixed between two tables, and the same weight support stand was positioned at the centre of the beam for equal weight distribution, as shown in Figure 3.18.

Weight
support   Clamp
stand   fixed
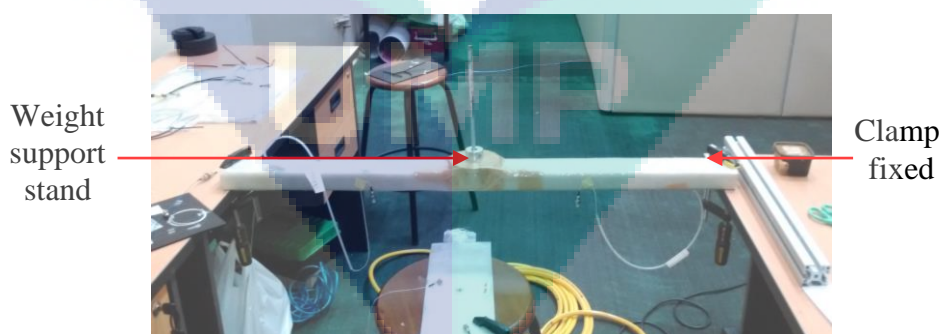
Figure 3.18   Fixture of the beam and placement of the weight support stand on the beam

Mesh-grid function with the scaling of -10 to 10 in the x-axis direction, -2 to 2 in the y-axis direction, and 0 to -50 in the z-axis direction. The change of voltage, estimated weight, and virtual deflection on the beam was recorded. Low-cost edge-filter interrogation system with the utilization of photodetector was used in this

experimentation. For voltage normalization experimentation, the same composite plate was utilized, with the same set-up and experimental procedure. However, several configurations of interrogation system were experimentally performed to demonstrate that the root of the voltage variations was due to high power light source.

The first configuration performed was to demonstrate that the utilization of different optical components could result in wavelength distortion, and the formation of unwanted wavelengths from the reflected Bragg wavelength of the sensing FBG, when viewed from the OSA. Here, there were three different configurations of the optical components, which were utilization of optical circulator, labelled as SET A, 50:50 intensity ratio optical coupler, labelled as SET B, and 1:8 intensity ratio optical splitter, labelled as SET C as shown in Figure 3.19. The reflected peak Bragg wavelength shifts of the sensing FBG were observed and recorded with the increment of every 10 N load.
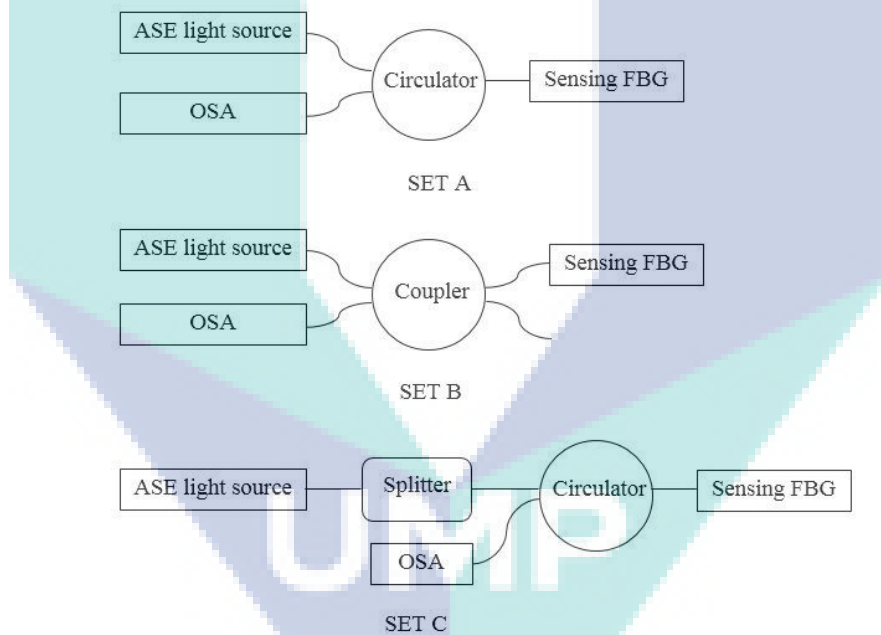
Figure 3.19   The experimental set-up interrogation system configurations

Next, the edge filter interrogation system configuration was carried out. Although edge filter interrogation system has been reported in the early 00's, the fluctuation of output voltages due to direct measurement without normalization in utilizing the photodetector as signal conversion, made this low-cost interrogation system non-stable and non-robust. The configuration shown in Figure 3.20 was adopted.
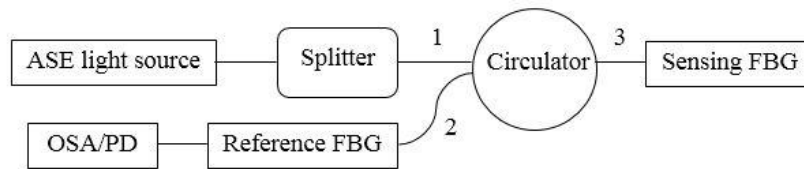
Figure 3.20   The configuration of edge filter detection interrogation system

The wavelength spectrums between sensing and reference FBG, reflected mismatched wavelength, peak wavelength and intensity shifts were viewed from the OSA and recorded. Next, with the same configuration, PD was utilized and five repetitions of voltage response against applied load were recorded. Then, calibration was formulated by averaging the five linearity curves without the voltage normalization algorithm, and the output voltage variations with the estimated load were recorded by using the MATLAB GUI real-time monitoring system. After that, voltage normalization algorithm was implemented on the averaging calibration linearity equation, and the output voltage variations with an accuracy of the estimated load were recorded. The voltage normalization GUI real-time monitoring system and the coding can be referred in Appendix B.

3.6   Overall Dynamic Strain Sensitivity Test Experimental Set-Up

Overall dynamic strain sensitivity was also performed to determine the maximum capability of the FBG sensor as a dynamic strain sensing device. For this experimental setup, an eight layer hand lay-up composite plate with a total thickness of 0.8 cm and a dimension of 90 cm x 13 cm (length x width) was fabricated, with a surface attached 1544.122 nm FBG sensor at a distance of 15 cm away from the edge of the composite plate. A shaker connected to McIntosh MC LA-500 power amplifier was attached to the centre of the plate to excite the plate with certain natural frequency. The knob of the gain was set to 20% of the overall maximum performance. NCH tone generator software, that generated a constant continuous sine wave with the increment of every 100 Hz, was used to drive the shaker. The plate was clamp fixed at four edges with G-clamp, as illustrated in Figure 3.21, and the intensity demodulation interrogation system with the reference FBG of 1544.733 nm, as shown in Figure 3.20, was used to capture the frequency spectrum of the plate, up to a point where the frequency spectrum captured by the FBG did not show any signal.
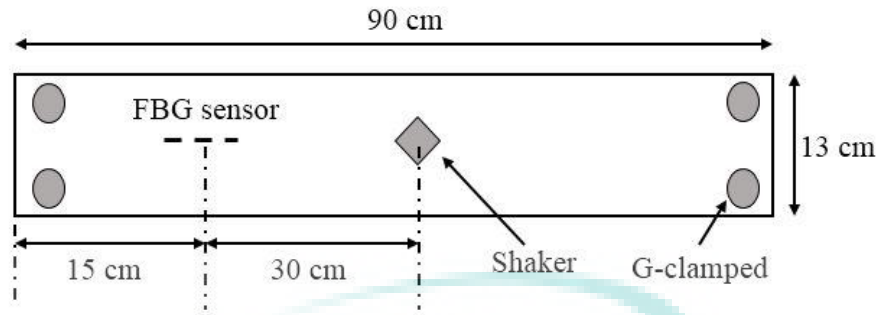
Figure 3.21   The experimental set-up for the overall dynamic strain sensitivity performance

At the meantime, Abaqus FEA analysis was carried out to determine the resonance frequency, which is the excitation frequency approaching natural frequency of the plate itself. The composite plate was created in 2-D lamina composite type with a layer by layer thickness of 0.08 cm each for a total of 10 layers. The mechanical properties, as in Table 3.11, was inserted, whereas Figure 3.22(a) shows the translational and rotational fixed boundary conditions (U1=U2=U3=0) of the composite plate, and Figure 3.22 (b) shows the meshing element with mesh global size of 0.04 mm on the composite plate.

(a)   (b)
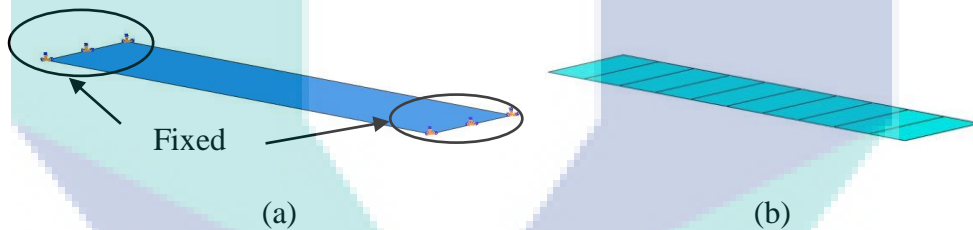
Figure 3.22   Abaqus FEA simulation for the dynamic sensitivity test: (a) Fixed boundary conditions of the composite plate (b) Meshing of the composite plate for analysis

Linear perturbation with independent instances was set for the meshing process. To excite the natural frequency of the plate, a load with pressure magnitude of -1 was apply throughout the surface of the plate and the vibration was set to vibrate from base state.

3.7   Dynamic Strain Sensing Experimental Set-Up

For dynamic strain sensing experimentation, impact localization utilizing CC-LSL algorithm and excitation of the structure's natural frequency was carried out. The GFRP composite beam was used for the impact localization where both ends were clamp fixed. Figure 3.23 shows the schematic illustration of the whole system, where FBG 1 with the wavelength of 1550.44 nm was filtered with the reference FBG of

1550.42 nm, whereas FBG 2 with the wavelength of 1550.22 nm was filtered with the reference FBG of 1549.20 nm.
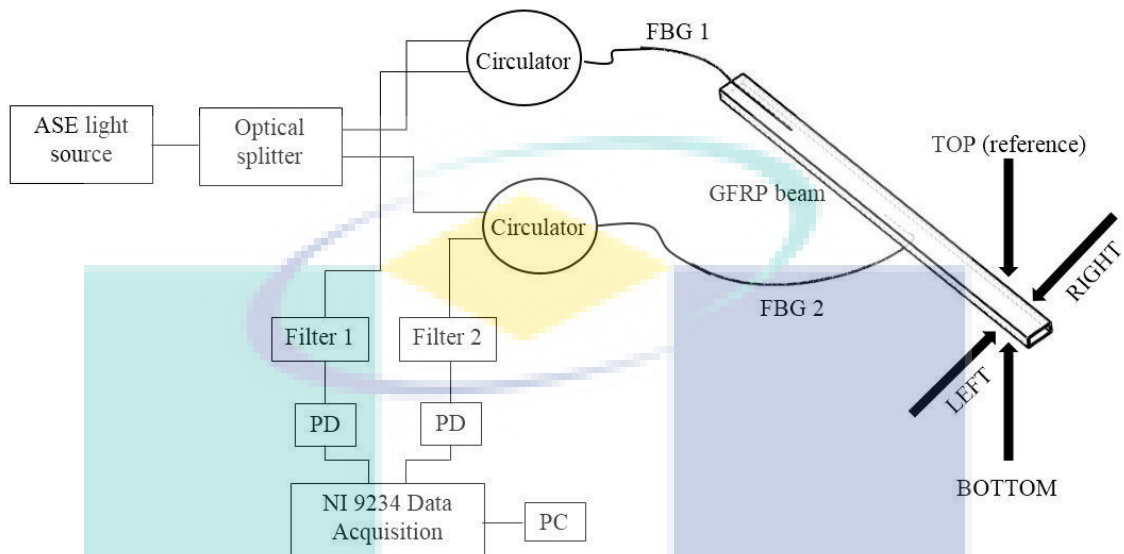
Figure 3.23   The schematic illustration of the impact localization interrogation system

One FBG was embedded on the top surface of the beam, whereas the other FBG was embedded on the bottom surface of the beam. The top and bottom embedment of the FBG was to investigate the effectiveness and capability of the peak detection by cross-correlation in the contrasting wave propagation. All four sides (top, bottom, left, and right) of the beam was induced with impact hits to demonstrate the accuracy of the proposed method. The impact was induced by using a hard flat chisel. A set of impact for 30 trials was hit at point A, B and C of the top surface. Points D, E, F, G, H and I was induced at the left and right sides of the beam. Next, points J, K and L at the bottom surface were hit by inverting the beam making FBG 2 as the reference sensor. Impact for points at left and right sides of the beam remained unchanged. Table 3.12 summarized the impact points for better illustration.

Table 3.12   The summarization of the impact points induced on the beam

Reference sensor	Surface	Impact location point	Frequency determination point
FBG 1	Top	A, B	C
	Left	D, E	F
	Right	G, H	I
FBG 2	Bottom	J, K	L
	Left	D, E	F
	Right	G, H	I

Impact at points A, B and C was hit at a distance of 28.5 cm, 46.5 cm and 77 cm away, measured from the edge of the beam. This impact distance was maintain unchanged for points at the left, right and bottom of the beam. For impact localization, the impact points must be executed within the embedment of the two sensors. This is to develop a disparate TOA between the two captured signals. Thus, point A was hit 9 cm close to the right of FBG 1 and point B was hit 3 cm close to the left of FBG 2. Point D, E, G, H, J, and K was hit at the same location within the two sensors. Figure 3.24 illustrate the impact locations induced on the beam.

(a)

(b)
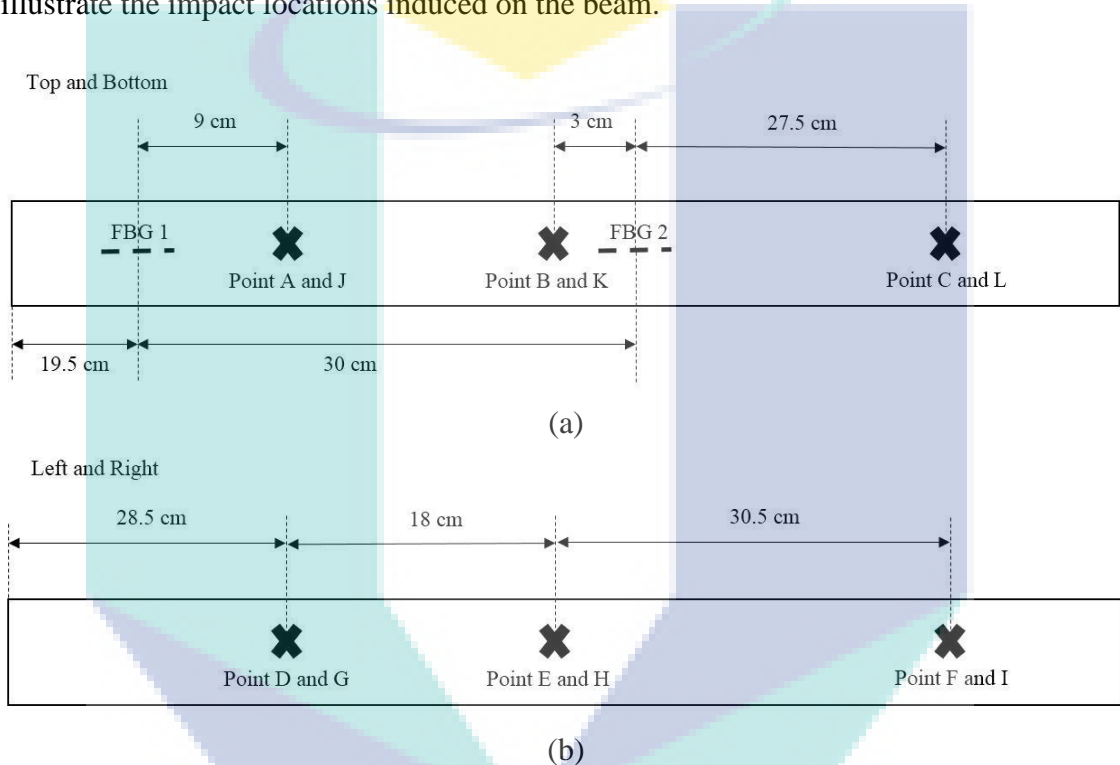
Figure 3.24   The impact locations for: (a) Top and bottom (b) Left and right sides of the beam

The impact signals received by both sensors were denoted as x_i with $i = 0$ and 1. The delay of the signals would occur in one of the sensors due to difference in impact distance. Both of the signals were then peak cross-correlated and maximized over τ. The cross-correlated signals were then integrated and squared for sample shifts until the peak was detected. The time difference was then obtained by dividing the sample difference by sampling frequency, F_s. This time, the difference was substituted into the linear source location algorithm for impact location estimation. MATLAB GUI impact localization real-time monitoring system with a sampling frequency, F_s of 5000 Hz, and a window size of 2000 samples was used to record the impact estimation, as shown in

Appendix C. Figure 3.25 shows the flow chart of the CC-LSL algorithm in GUI monitoring system.
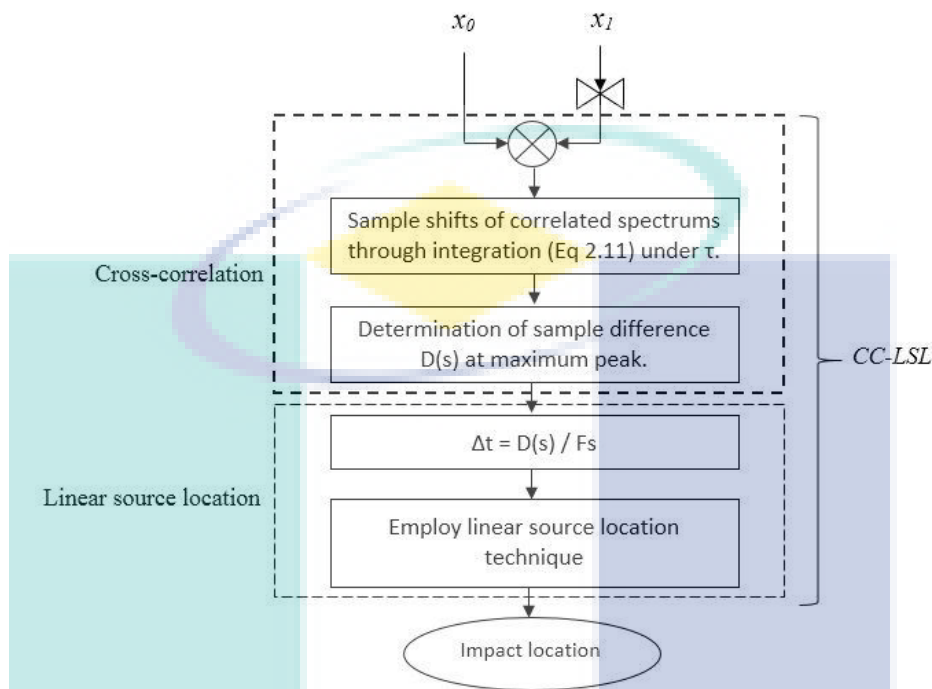
Figure 3.25   The flow chart of the CC-LSL algorithm in GUI monitoring system

For the excitation of natural frequency, the same fixture and system's configuration was implemented. The frequency determination points (C, F, I, and L) was hit far away from both the sensors placement. This is to evaluate the capability of the embedded sensor in capturing frequency spectrum that are far away from the source. FBG 1 was assigned to capture the natural frequency spectrum. For validation, an acoustic emission (AE) sensor was surface attached to the beam in the same position as FBG 1, as shown in Figure 3.26.
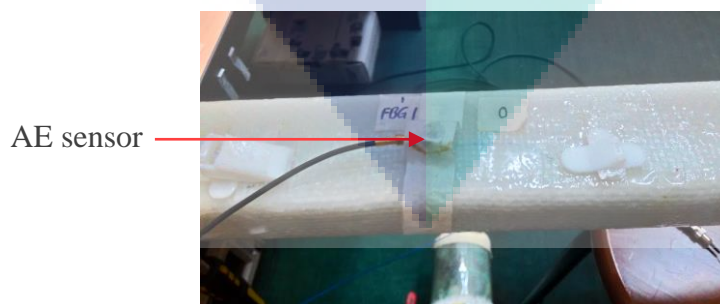
Figure 3.26   Surface mounting of the AE sensor for data validation with FBG sensor

In Abaqus FEA simulation, a 2-D deformable beam was created with the desired dimension. The mechanical properties as shown in Table 3.11 was inserted in

the analysis. The translational and rotational fixed boundary conditions (U1=U2=U3=0) of the beam are shown in Figure 3.27(a), whereas Figure 3.27(b) shows the meshing of the beam with instance global seed of 0.1 mm for analysis.
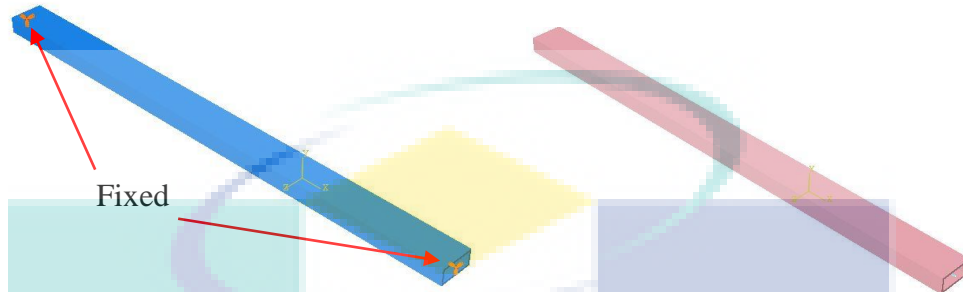
Figure 3.27   Abaqus FEA simulation: (a) Fixed boundary conditions of the beam (b) Meshing of the beam for analysis

The simulated natural frequency was set to be obtained for a maximum of 1000 Hz. MATLAB GUI with Fast Fourier Transform (FFT) function was split into two windows, where a sampling frequency, F_s of 1000 Hz was set for the first window to capture frequency range from 0 to 500 Hz, while a sampling frequency, F_s of 2000 Hz was set for the second window to capture frequency range from 600 to 1000 Hz. This was also to preserve the resolutions of all the natural frequency modes, especially the natural frequency for the first mode. Natural frequency excitation had also been carried out for the composite plate. The composite plate was clamp fixed at four edges, with an AE sensor surface attached in the same position as the embedded FBG sensor, as shown in Figure 3.28 (a). A set of impacts with 30 trials was hit at 15 cm away from the placement of both sensors, as shown in Figure 3.28 (b).

| (a) | (b) |
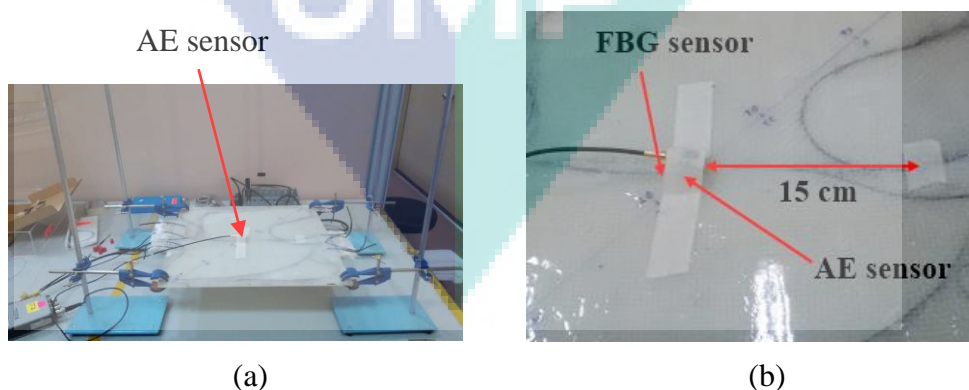
Figure 3.28   Natural frequency excitation experimental set-up: (a) Fixture of the composite plate with surface attached AE sensor (b) A set of impacts was hit 15 cm away from both the sensor placement

In Abaqus FEA analysis, composite plate was created in 2-D lamina composite type with a layer by layer thickness of 0.08 cm each for a total of 10 layers. The mechanical properties as shown in Table 3.11 was inserted with the translational and rotational fixed boundary conditions (U1=U2=U3=0) at the four edges, as shown in Figure 3.29(a). Figure 3.29(b) shows the meshing of the composite plate with instance global size of 0.04 mm. A linear perturbation with independent instances was set for the meshing process. To excite the natural frequency of the plate, a load with pressure magnitude of -1 was apply throughout the surface of the plate and the vibration was set to vibrate from base state.

The frequency to be obtained was set to a maximum of 500 Hz. MATLAB GUI with FFT function and a sampling frequency, F_s of 1000 Hz was coded to capture the natural frequency for both the FBG and AE sensors simultaneously in real-time.

Fixed

(a)   (b)
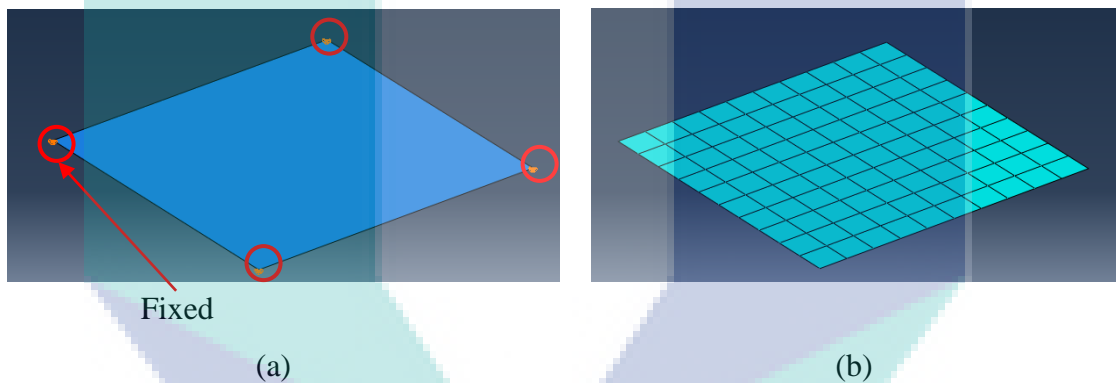
Figure 3.29   Abaqus FEA simulation: (a) Fixed boundary conditions of the composite plate (b) Meshing of the composite plate for analysis

The natural frequencies obtained from FBG and AE sensors (experimental results) were compared with the simulation results from Abaqus FEA analysis (theoretical results) for validation. The coding GUI real-time monitoring system with FFT function for the composite plate can be referred in Appendix D.

3.8   Chapter Summary

The planning of the overall experimental procedure was presented in the flow chart in Figure 3.1. Several components commonly utilized in this experimental work, such as 20 mW of ASE broadband light source, optical circulator, optical coupler, optical splitter, photodetector, OSA, data acquisition system and AE sensor were briefly explained with listed specifications. An introduction to the MATLAB GUI real-time

monitoring system for retrieving data and information was emphasized as well. For the improvement in the static strain monitoring system, both composite plate and GFRP composite beam were clamp fixed at the edges, and being subjected to loadings, starting from no load to a maximum of 50 N. MATLAB GUI with mesh-grid function real-time monitoring system was applied to monitor the deflections of the specimens in the artificial virtual display. Another amendment in the static strain monitoring system was the minimization of the output voltage variations. For this experimentation, the same composite plate with the same fixture and experimental procedure was monitored for the variations in the output voltages. MATLAB GUI with voltage normalization algorithm and without normalization was implemented for comparison of the recorded output voltages.

Overall static and dynamic sensitivity tests were initially performed to determine the sensitivity and maximum capability of the FBG sensor before proceeding to the experimental testing. For improvement in the dynamic strain sensing monitoring system, the GFRP composite was clamp fixed at both ends between two tables, and was induced with a set of impacts with 30 trials at two different locations, labelled as point A and point B. MATLAB GUI with CC-LSL was utilized for the accuracy of impact estimation. Another set of impact with 30 trials was induced at point C for excitation of the structure's natural frequency. An AE sensor was surface attached at the same position as FBG 1 for experimental data validation. Theoretical simulation analysis utilizing Abaqus FEA was carried out as well for comparison, where the mechanical properties presented in Table 3.11 was inserted. The excitation of natural frequency was carried out on the composite plate as well. The composite plate was clamp fixed at the end of the four edges, with the same boundary conditions set in Abaqus FEA. An AE sensor was surface mounted in the same position as the embedded FBG, and a set of impacts with 30 trials was induced at a distance of 15 cm away from both the sensor placements. Experimental results from the FBG and AE sensors captured by the MATLAB GUI real-time monitoring system was validated with Abaqus FEA theoretical simulation.

CHAPTER 4

RESULTS AND DISCUSSION

4.1   Overall Static Strain Sensitivity Test Experimental Results

The sensitivity value of the FBG sensor for static strain measurement reported in this study is in the unit of picometre (pm) against microstrain (με), which is the Bragg wavelength shift corresponding to the optical fibre strain elongation. This standardized unit for static measurement permits comparison with other sensors and setups. The change of wavelength or Bragg wavelength shift ($\Delta\lambda$) were calculated from equation 2.5. Figure 4.1 shows the line graph of Bragg wavelength shift against strain for the tensile elongated FBG sensor, which recorded the overall sensitivity as 1.21 pm/με. The sensitivity obtained correlates well with the findings by other researchers (Kinet et al., 2014; L. Li, Zhang, Liu, Guo & Zhu, 2014), where the strain sensitivity of a 1550 nm FBG sensor ranged from 1.17 pm/με to 1.20 pm/με. The wavelength change per strain induced exhibited a linear correlation coefficient, R^2 of 1.
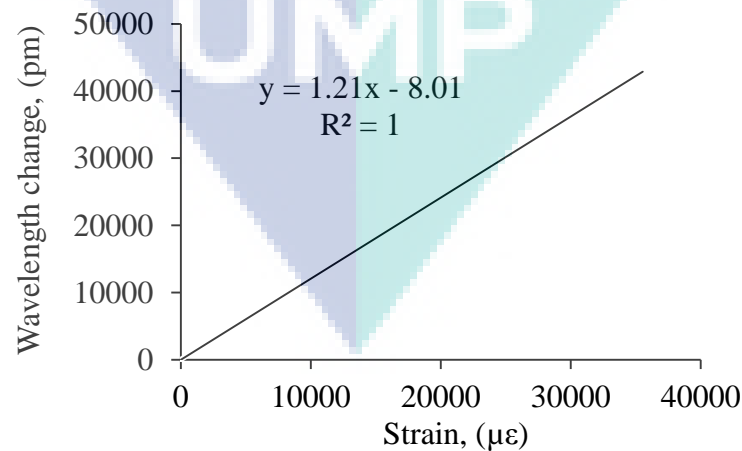
Figure 4.1   The static sensitivity graph of the FBG sensor

Figure 4.2 shows the line graph of the reflected wavelength from the FBG sensor against the extension of the body specimen. The reflected Bragg wavelength at the initial no strain condition was recorded at 1545.84 nm, and continuously shifted to a maximum of 1547.92 nm, at the maximum extension of 2.67 mm across steady extension, at an average of 0.08 mm to a point where the optical fibre ruptured. As a justification, the optical fibre was very brittle with high modulus of elasticity, that it could only be stretched to a maximum length of 2.67 mm, where it finally ruptured. Another conclusion that can be made from the shift of the reflected wavelength against the extension is that the optical fibre underwent tension elongation.
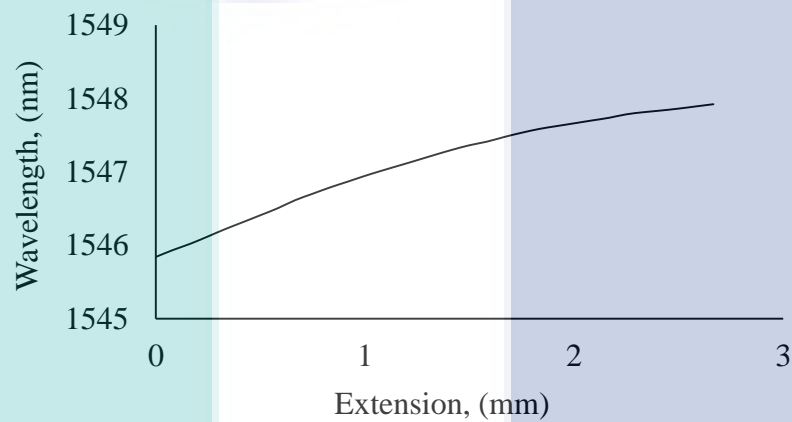
Figure 4.2 The line graph of reflected Bragg wavelength against extension
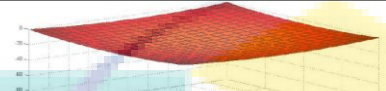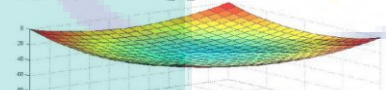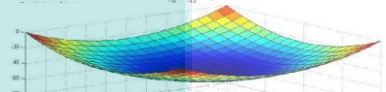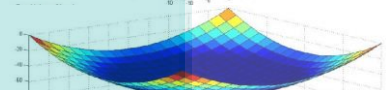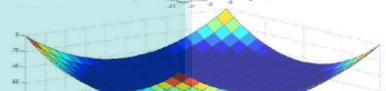
4.2 Static Strain Sensing Experimental Results

Table 4.1 summarizes the results of the static strain sensing mesh-grid function for composite plate, while Table 4.2 summarizes the results for GFRP beam. For composite plate, the voltage change increased by 0.075 V for every 10 N increment of loading. At 10 N loaded condition, the voltage reading was recorded at 3.61 V, and the maximum voltage reading was 3.91 V, recorded at the highest loading of 50 N. The linearity equation shown in Figure 4.3, with the sensitivity of 7.8 mV/N and a correlation coefficient value, R^2 of 0.9902 in predicting the estimated loads.

For GFRP beam, the minimum voltage was recorded at a value of 4.74 V during 10 N loaded initial condition, as expected. As the load induced started to increase with an increment of 10 N, a significant linearity of voltage increase against the load induced was recorded. The linearity equation, as shown in Figure 4.4, with a sensitivity of 4.4

mV/N and correlation coefficient value, R^2 of 0.9877, estimated the load induced with a percentage error less than 10 %.

Table 4.1   The summarized results of static strain mesh-grid function for composite plate

Load induced (N)	MATLAB GUI	Voltage (V)	Load estimated (N)	Percentage error (%)
10		3.61	10.34	3.40
20		3.70	21.32	6.60
30		3.78	31.76	5.87
40		3.86	42.15	5.38
50		3.91	48.52	2.96

$$y = 0.0078x + 3.529$$
$$R^2 = 0.9902$$
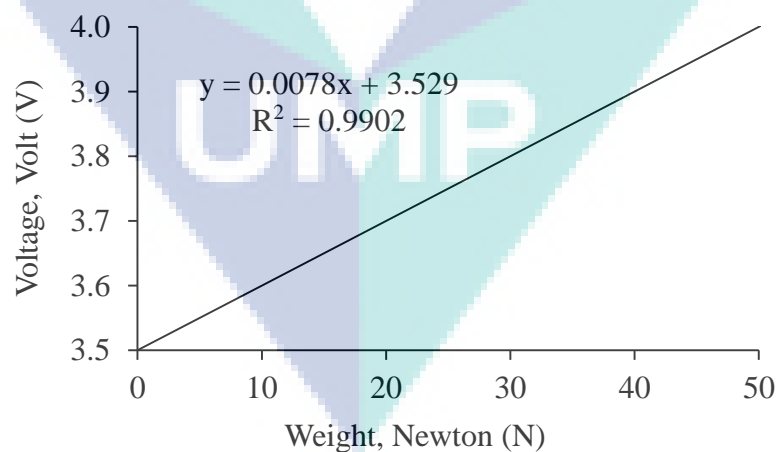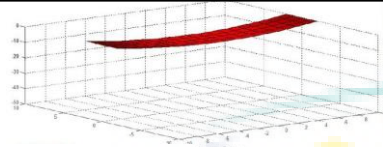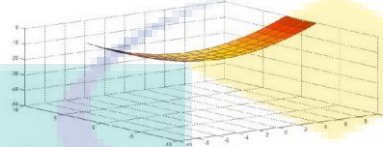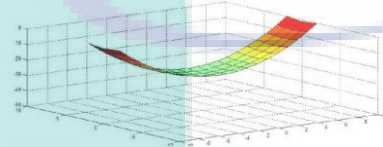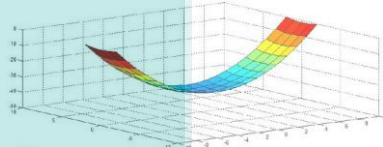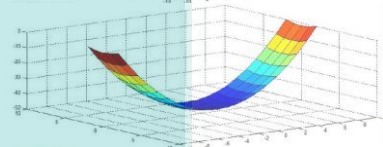
Figure 4.3   Linearity response of voltage difference against load induced for composite plate mesh-grid function

Table 4.2   The summarized results of static strain mesh-grid function for GFRP beam

Load induced (N)	MATLAB GUI	Voltage (V)	Load estimated (N)	Percentage error (%)
10		4.74	10.39	3.90
20		4.78	19.48	2.60
30		4.82	28.57	4.77
40		4.86	37.66	5.85
50		4.93	53.57	7.14

$$y = 0.0044x + 4.6943$$
$$R^2 = 0.9877$$
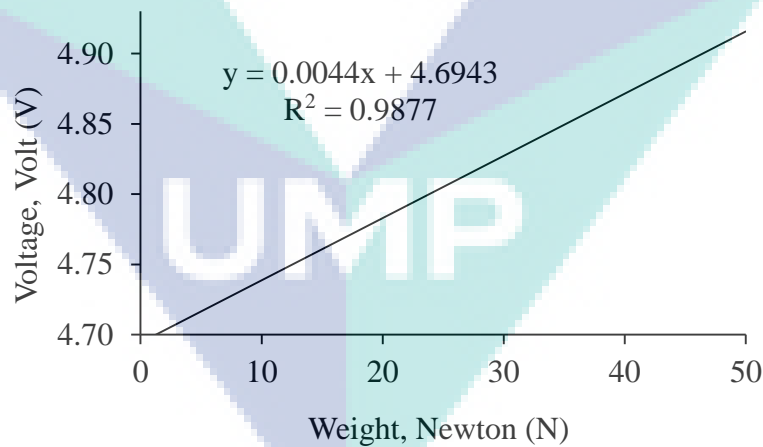
Figure 4.4   Linearity response of voltage difference against load induced for GFRP beam mesh-grid function

From the observation of the artificial virtual display on the structure conditions for both specimens, a slightly flat condition was exhibited at 10 N load, which implied that both specimens experienced weak strain in the 10 N load condition. As the load began to induce, the displays for both specimens started to deflect slightly, and sank the

most at 50 N loading, which verified that the structure experienced the most strain at the maximum load.

The displayed colour at the centre of the structural condition transformed from red to blue, signifying that strain was experienced the most at the centre, where the load was applied. From both of the artificial virtual display results, it is verified that the mesh-grid function is applicable to any structures regardless of shape and size. This function is definitely the alternative way to represent the real-time deflection of the structure, instead of using the spectrum.

For the improved method utilizing voltage normalization algorithm, Figure 4.5 shows the interpreted, reflected wavelengths of the sensing FBG in no load condition, from SET A, SET B and SET C optical components, as shown in Figure 3.19. From the results of all the reflected spectrums, optical component SET A which utilized circulator resulted in multiple unwanted wavelengths, as shown in Figure 4.5 (a). Four unwanted wavelengths with peak splitting were recorded at 1543.48 nm, 1544.08 nm, 1544.75 nm, and 1545.27 nm respectively. SET A showed the highest intensity, while 10.78% of the intensity was reduced when a coupler was utilized in SET B. The reflected wavelength was reduced to only two wavelengths, recorded at 1544.06 nm and 1544.86 nm, as shown in Figure 4.5 (b). SET C optical component revealed an ideal, single reflected Bragg wavelength, as shown in Figure 4.5 (c), with the value recorded at 1544.85 nm, and 66.47% of the intensity was reduced, compared to SET A.

From the overlaid graphs shown in Figure 4.5(d), different power intensities were obtained for different utilization of optical components. This is due to the working principles of the components themselves. The purpose of optical circulator was to circulate the full power, high optical intensity in one direction, from the light source to the FBG sensor. Thus, high power intensity was obtained in SET A optical component, which resulted in unwanted wavelengths due to this working principle. A 50:50 optical coupler which was utilized in SET B, functioned by splitting the light signal into two equally divided outputs with 50% each. However, only 10.78% of the intensity was scaled down in this experimentation due to the high power of the ASE light source. A splitter has the same function as an optical coupler. In this 1:8 splitter, the input signal was equally divided into eight output signals, which resulted in 66.4% power reduction, and an ideal reflected Bragg wavelength was attained.

(a)

(b)

(c)

80
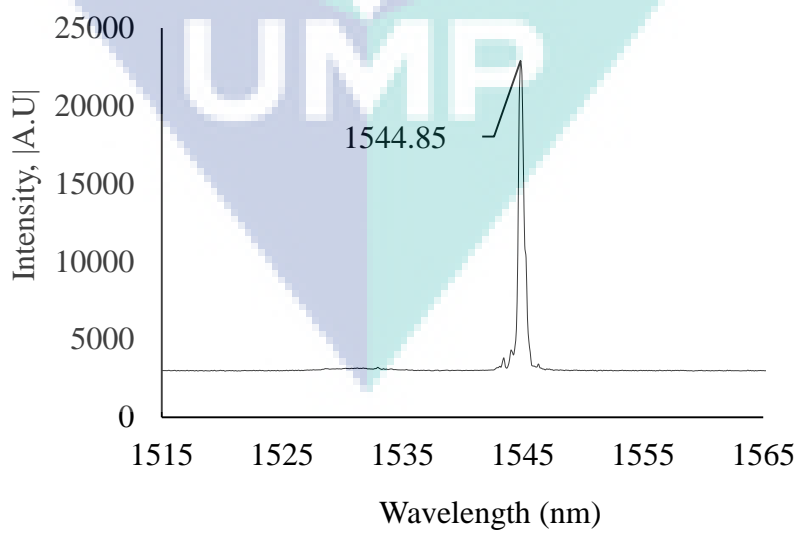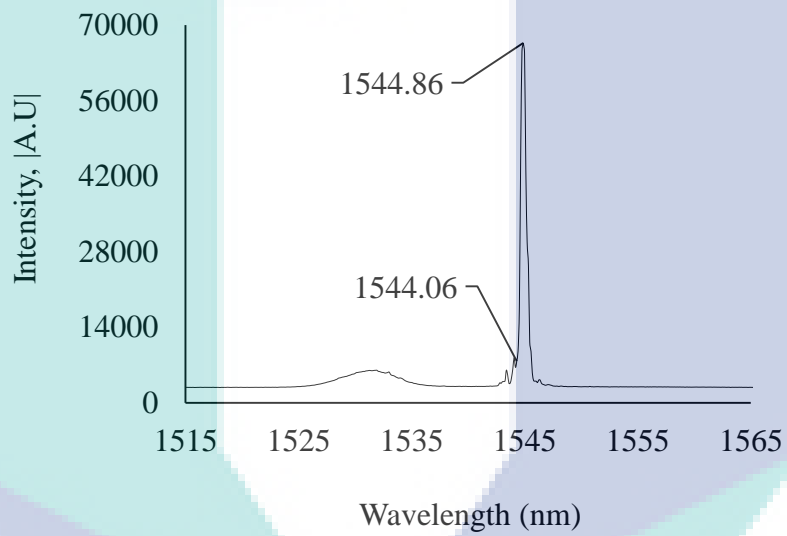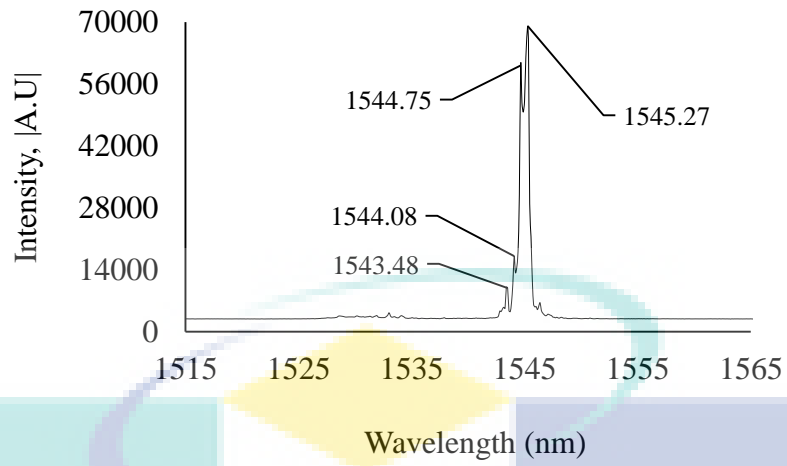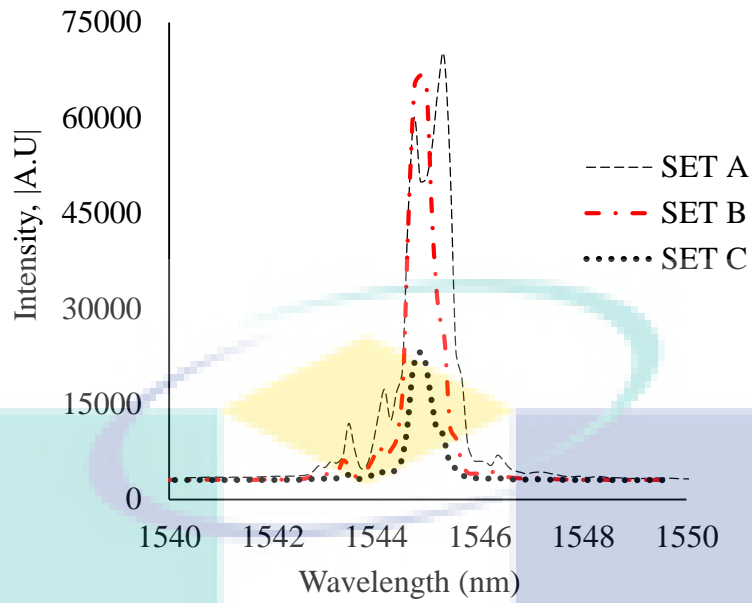
(d)

Figure 4.5   Reflected wavelengths of the sensing FBG from optical components: (a) SET A, (b) SET B, (c) SET C and (d) Overlay of all the optical components

The recorded peak wavelength shifts for all the optical components set across from loadings of 0 N to 50 N was shown in Figure 4.6, where the solid line represents the line of best fit for all the data points.
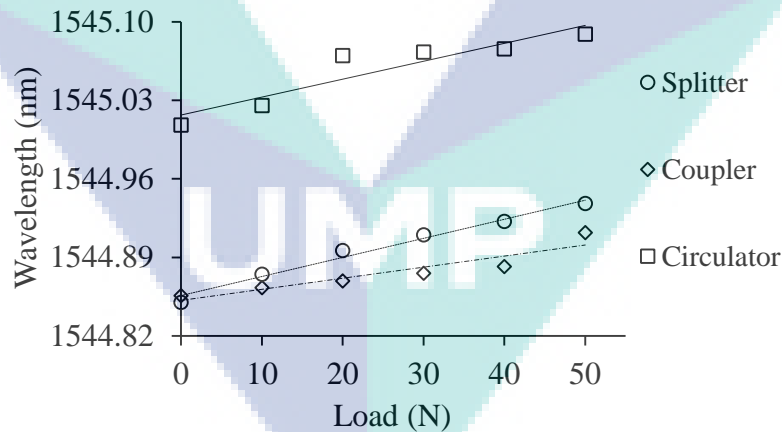
Figure 4.6   The reflected peak wavelength shifts for all the optical components across loadings of 0N to 50 N

The peak wavelength shift against load induced shows a linear correlation, where splitter configuration gave the highest sensitivity which was recorded at 0.0017 nm/N, followed by circulator and coupler which were recorded at 0.0016 nm/N and 0.001 nm/N, respectively. The peak wavelength shift for the optical circulator was determined by averaging the two split peaks.

The results shown in Figure 4.5 and Figure 4.6 obviously indicated that the splitter configuration was capable of reducing the unwanted wavelengths by reducing the power intensity, which indirectly eliminated the possible noise during the mismatching with reference FBG. Thus, the splitter configuration had been made use of throughout the experimentation, where Figure 4.7 shows the simplified Gaussian Bragg wavelength shift across the 50 N loadings. For the ease of illustration, the Gaussian shift has been offset by 0.1 nm/N, and the increase in the line's weight corresponds to the increase in loadings. The shapes of the Gaussian wavelengths are consistent with the linear shifts across the increasing loads. The embedded FBG sensor underwent tension-elongation each time the load was applied due to the shift of the Bragg wavelength towards the right.
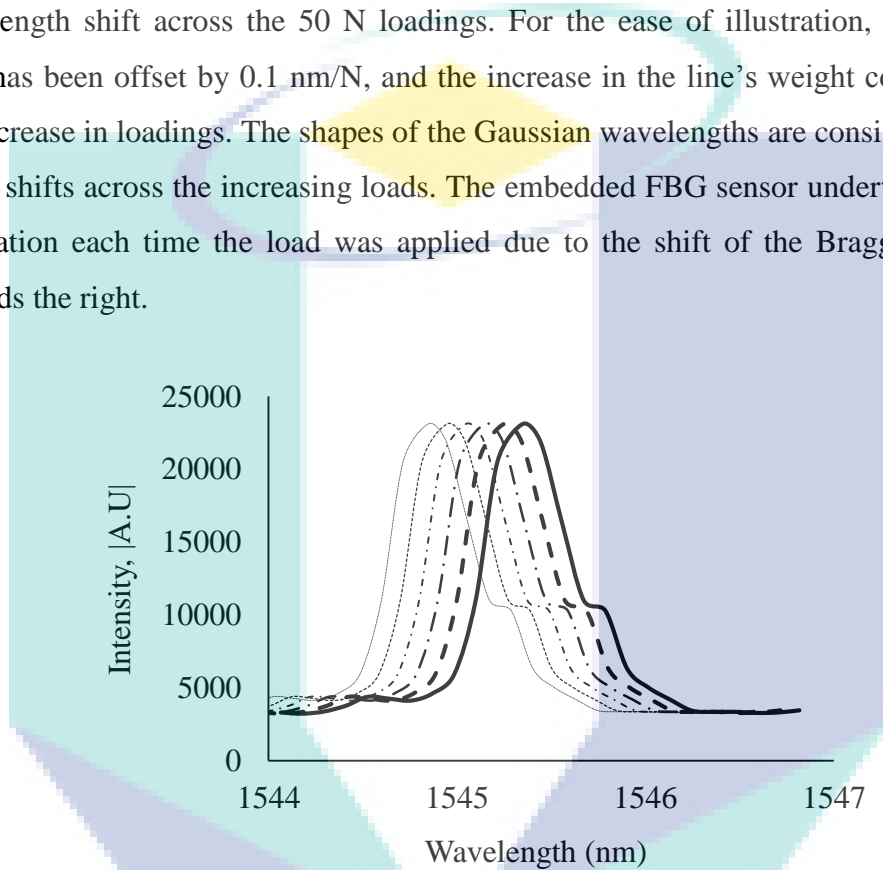
Figure 4.7   Gaussian Bragg wavelength shift across the 50 N loadings and the increase in line's weight corresponding to the increase in loading
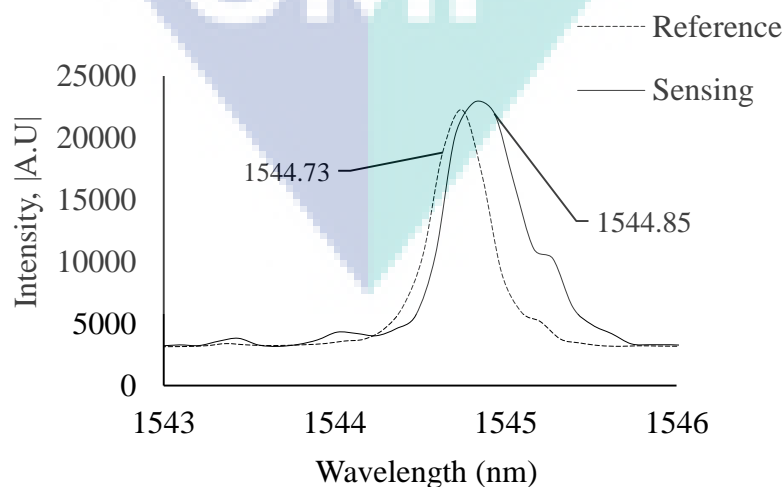
Figure 4.8   Reflected wavelength of the sensing and reference FBG

Figure 4.8 shows the reflected wavelengths of the reference and sensing FBG when both sensors were connected to port 3, as shown in Figure 3.20, while Figure 4.9 shows the mismatched reflected wavelength when the reference FBG was connected to port 2 and viewed from the OSA. It was observed that the intensity of the sensing FBG was about 3.76% higher than the reference FBG. The intensity of the mismatched reflected wavelength shows a good sensitivity of 64.51 |A.U|/N, and a slight sensitivity of peak wavelength shift, recorded at 0.0008 nm/N. Both the intensity and wavelength shift showed good linear increase across from 0 N to 50 N loadings as shown in Figure 4.10, and it could be concluded that the wavelength shift was insensitive to load induced during the intensity demodulation in edge filter interrogation system.
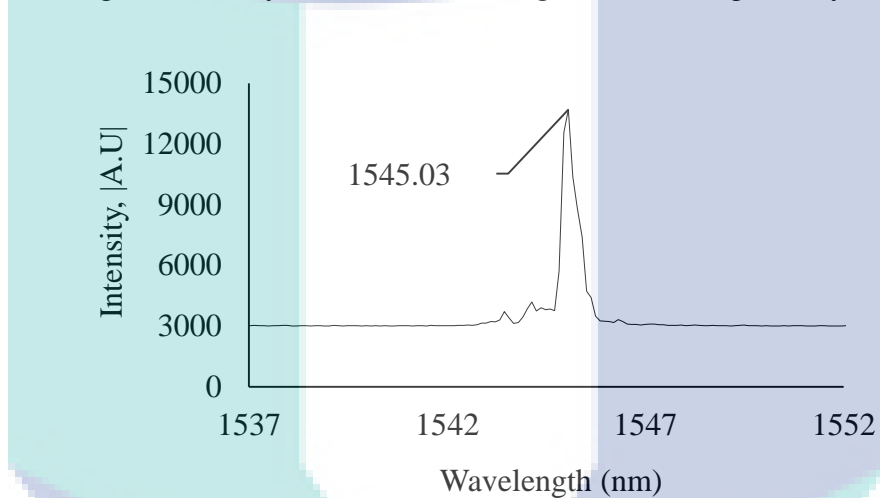
Figure 4.9　　The mismatched reflected wavelength between reference and sensing FBG

For a clear illustration of the increase in intensity amplitude and wavelength shift, a simplified Gaussian Bragg wavelength shift with an offset of 0.1 nm/N was demonstrated in Figure 4.11. From the results, the Bragg wavelength was recorded at an initial value of 1545.03 nm with the minimum intensity of 13880.4 |A.U| in no load condition, which shifted to a maximum wavelength of 1545.07 nm at the maximum 50 N loading, with an upsurge in intensity in waveform where the maximum intensity value was at 17068 |A.U|, as expected.
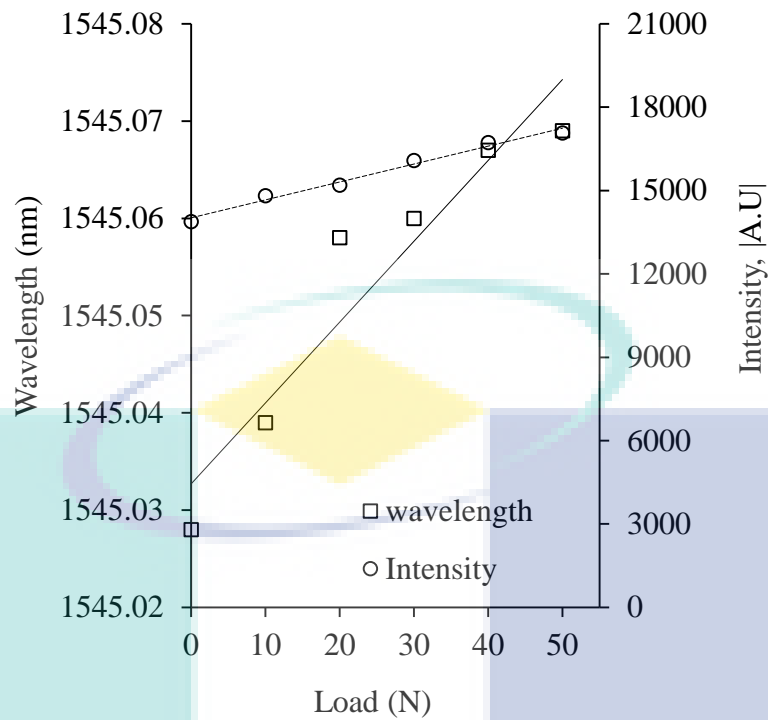
Figure 4.10   Peak wavelength and intensity shift of the mismatched reflected wavelength with the straight lines representing the line of best fit
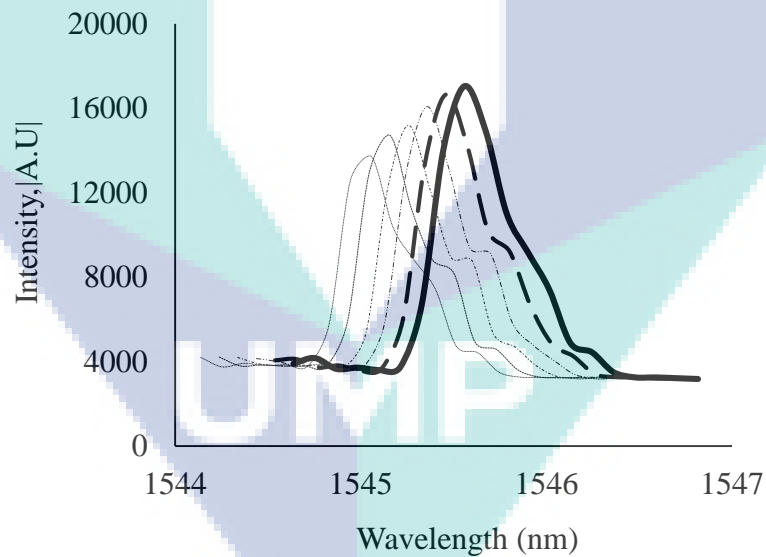
Figure 4.11   Gaussian Bragg wavelength shift of the mismatched reflected wavelength with the increase in line's weight corresponding to the increase in loadings

Lastly, the intensity demodulation was altered to voltage reading with the replacement of OSA with PD. Calibration to convert the voltage response to applied load was carried out by averaging the linear curves of the five repetitions of voltage responses without the voltage normalization algorithm, as shown in Figure 4.12.
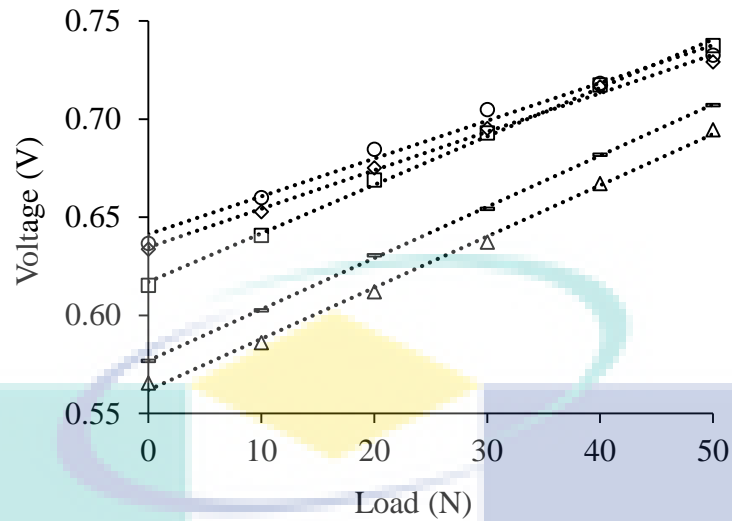
Figure 4.12   The five repetitions of voltage response against load induced without voltage normalization algorithm

The average of the calibrated linear curves was then substituted in MATLAB real-time GUI monitoring system to record the variation in voltage responses as the plate was induced with loadings from 0 N to 50 N as shown in Figure 4.13. Next, by employing the same voltage response, the calibration was carried out by implementing the ratio voltage normalization algorithm, as shown in equation 2.7, into the averaged linear curves, as shown in Figure 4.14.
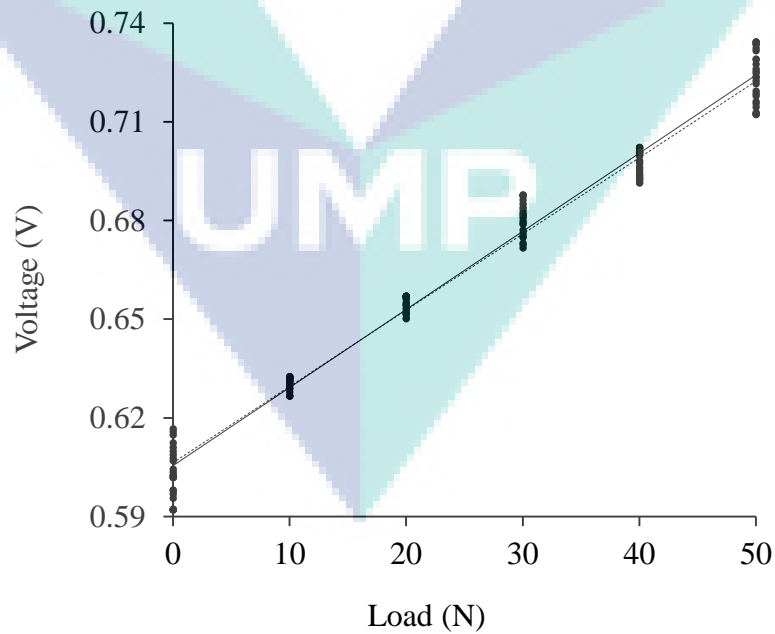
Figure 4.13   The output voltage variations (data points) without voltage normalization algorithm where the solid line is the line of best fit, and the dashed line is the expected voltage obtained from the linearity equation

The voltage normalization algorithm is the ratio of voltage difference due to load induced over the initial voltage acquired by the GUI monitoring system. For every increment of loading, the calibrated linearity equation was based on the ratio of voltage difference instead of voltage change due to the load induced alone. Due to the distinct power of the light source and mismatching condition, the initial voltage readings were not consistent in each operation.
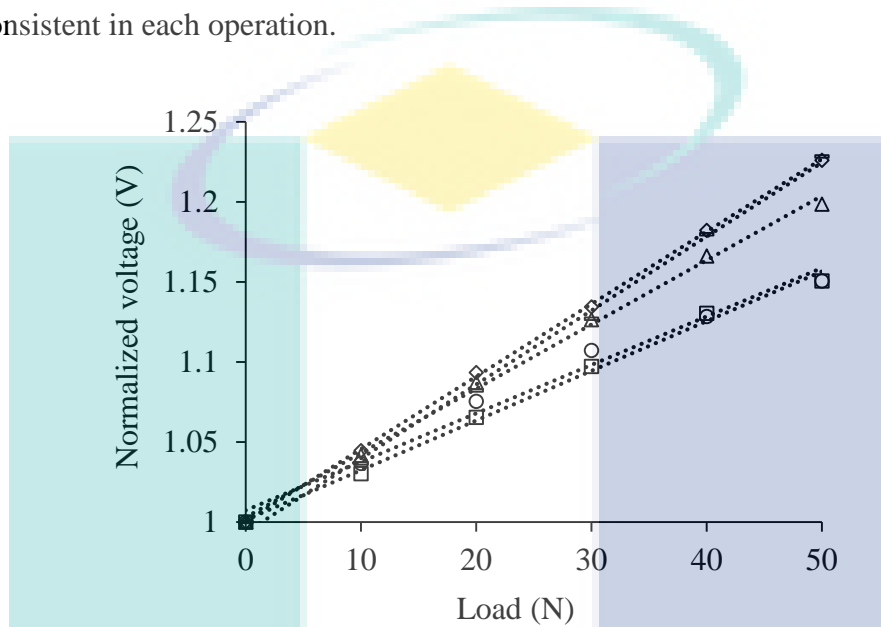
Figure 4.14   The five repetitions of voltage response against load induced with voltage normalization algorithm
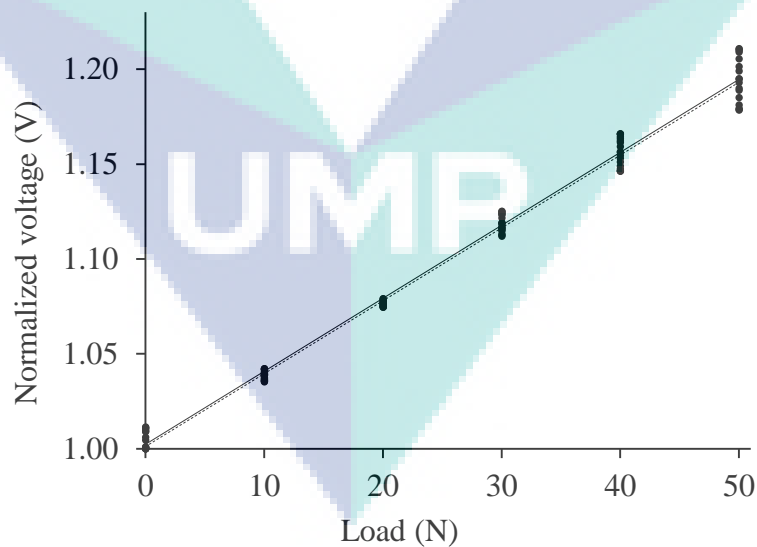
Figure 4.15   The output voltage variations (data points) with voltage normalization algorithm where the solid line is the line of best fit and the dashed line is the expected voltage obtained from the linearity equation

Thus, this ratio voltage normalization algorithm will give a more accurate reading without pre-calibration. The ratio voltage normalization linearity equation was substituted in MATLAB real-time GUI monitoring system and used to record the voltage variation, as shown in Figure 4.15. At the meantime, the voltage data response was reduced by programming a delay of 1 second with the sensitivity recorded at 3.8 mV/N. From the comparison of the five repetitions of voltage responses as shown in Figure 4.12 and Figure 4.14, ratio voltage normalization was undoubtedly decent in organizing a cluttered and scattered data to a well-organized and correlated statistical data. The delay of 1 second had reduced the voltage data points from 26 data/minute to 17 data/minute, which limited the range of voltage variation. On the other hand, the algorithm had increased the sensitivity of the sensing measurement to 3.8 mV/N.

Table 4.3 summarizes the results of the average load, estimated with the average percentage of error obtained from the non-normalized voltage variations shown in Figure 4.13. The highest average percentage of error was estimated at 12.19 % during the 10 N load, and the average percentage of error for the overall load was estimated at 5.35 %. Table 4.4 summarizes the result of the average load estimated for each load, and their average percentage of errors obtained from the normalized voltage variation in Figure 4.15.

Table 4.3   The summarized results of average load estimated and average percentage of error without voltage normalization algorithm (non-normalized)

Load (N)	Average load estimated (N)	Average percentage of error (%)
10	11.22	12.19
20	18.77	6.14
30	30.16	0.55
40	41.82	4.54
50	48.34	3.32
Average percentage of error		5.35

Table 4.4   The summarized results of average load estimated and average percentage of error with voltage normalization algorithm (normalized)

Load (N)	Average load estimated (N)	Average percentage of error (%)
10	9.84	1.65
20	19.76	1.22
30	30.63	2.12
40	40.41	1.02
50	50.44	0.88
Average percentage of error		1.38

The highest average percentage of error was 1.65 % during the 10 N load, and the average percentage of error for the overall load estimated was 1.38 %. Although the overall average percentage of error between non-normalization and normalization do not have much difference, the greatest advantage of the ratio voltage normalization algorithm is the bypass of pre-calibration each time before the operation. Non-normalization voltage response is only accurate for one application and needs to be calibrated each time before use. The replacement of OSA with PD gives the low-cost edge filter interrogation system compatibility with any low-cost electronic data acquisition devices, such as NI-DAQ and programmable logic controller (PLC), which avoids the use of expensive interrogation devices. However, a stable real-time monitoring system is still essential to attain the accurate readings desired. From the results of the experimentation, it was observed that when the Bragg wavelength of the sensing FBG was adjusted to the right of the reference FBG, the voltage output from the PD would increase as the FBG sensor elongated (Chuang, Liao & Ma, 2011).

4.3 Overall Dynamic Strain Sensitivity Test Experimental Results

The dynamic sensitivity of the FBG sensor was performed with the intention to determine the maximum capability of the FBG sensor in capturing the frequency spectrum with the setting as shown in Figure 3.21. From the sensitivity response shown in Figure 4.16, the sensitivity curve shows descending level of responses with the application of increased frequencies.
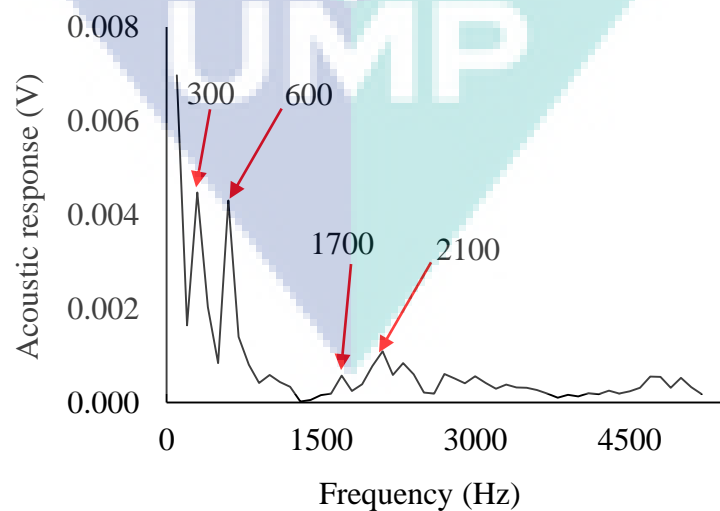
Figure 4.16   The sensitivity response curve of the FBG sensor

From the results, four sharp and pointed response peaks were observed at the frequency values of 300 Hz, 600 Hz, 1700 Hz, and 2100 Hz respectively. The captured frequency spectrum was regarded as the resonance frequency which was the excitation frequency from the source of the shaker approaching the natural frequency of the structure plate. A clear illustration on the normalized power frequency spectrum is shown in Figure 4.17, where the output power from the FBG was normalized with the input power from the accelerometer attached to the shaker. FEA validation from Abaqus analysis, as in Table 4.5, verified that the resonance frequency occurred during modal shape 8, 12, 20, and 21 of the plate's natural frequency with the highest percentage of error at 3.58 %. In general, the overall maximum sensitivity of the FBG sensor was recorded at 5 kHz. The results correlate well with the findings by Campopiano et al. (2009) who experimented on the sensitivity of the FBG hydrophone, where the trend of the sensitivity curve decreased against the increasing frequencies (Campopiano et al., 2009). On the other hand, Saxena et al. (2012) also performed a frequency sensitivity test on the FBG hydrophones, and obtained a maximum sensitivity of around 5.3 kHz, with the presence of three resonance frequencies (Saxena, Guzman & Pflanze, 2012).
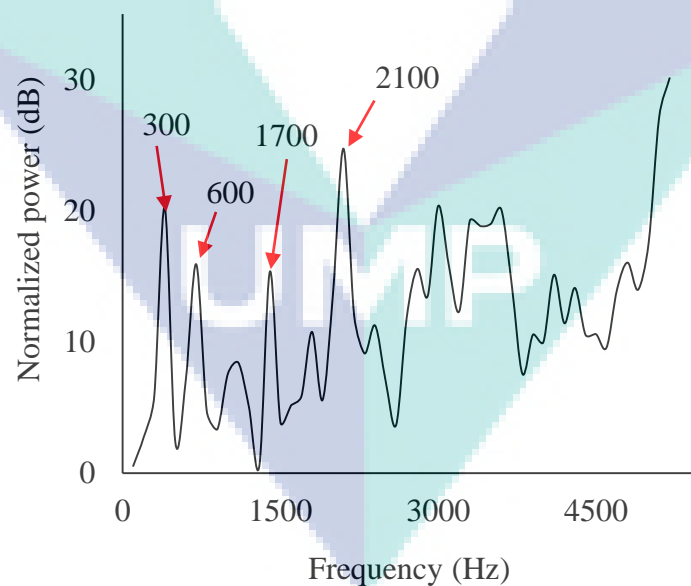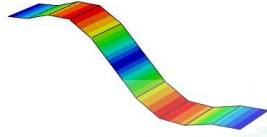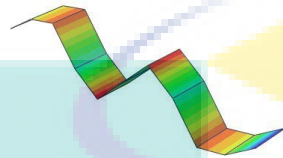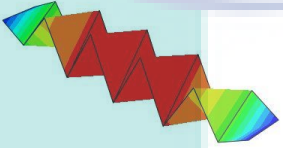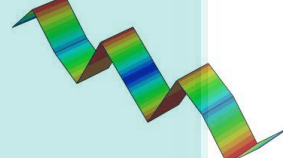
Figure 4.17   The normalized power sensitivity response curve of the FBG sensor

Table 4.5   The natural frequency of the composite plate

Mode shape	FEA simulation	Resonance frequency (Hz)		Percentage error (%)
		FEA	FBG sensor	
8		309	300	2.91
12		613	600	2.12
20		1712.2	1700	0.71
21		2177.9	2100	3.58

4.4 Dynamic Strain Sensing Experimental Results

For the improvement of the dynamic strain sensing monitoring system, a cross-correlation algorithm was employed to determine the time difference between two impact signals, and the time difference was then substituted in the linear source location technique for accurate impact estimation. Cross-correlation method had a poor performance as the significant peak of the signal was submerged in the noise spectrum due to the low signal to noise ratio (SNR), making the peak detection difficult and inaccurate. Thus, an adequate signal to noise ratio (SNR) had to be assigned in order to preserve and sustain the precision of the peak detection.

The performance of the cross-correlation peak detection at particular SNR values was illustrated in Figure 4.18. The sampling point was set 2000 and the sampling frequency is 5000 Hz. From the results, the cross-correlation method did not reflect any peaks at SNR=0 dB.

SNR = 0 dB
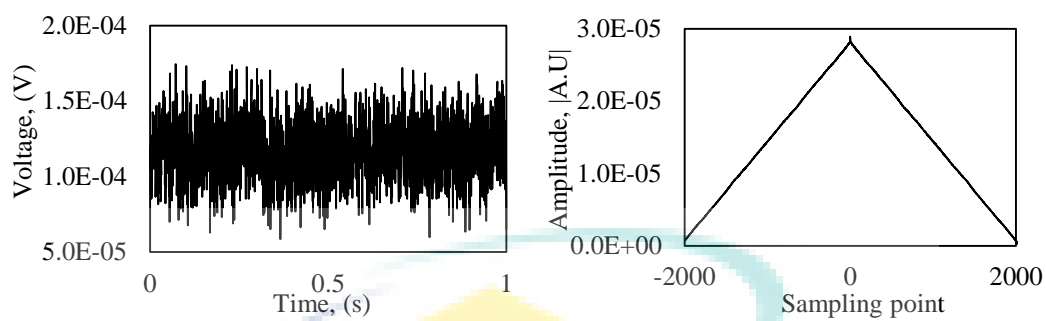
SNR = 10 dB

SNR = 20 dB

SNR = 30 dB

SNR = 40 dB
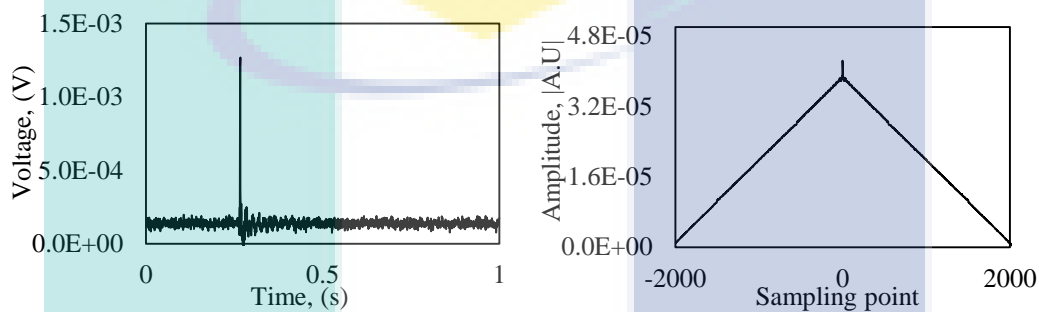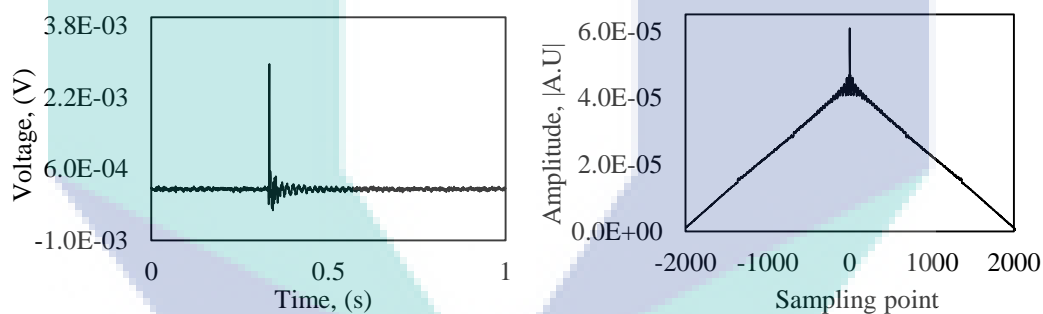
SNR = 50 dB
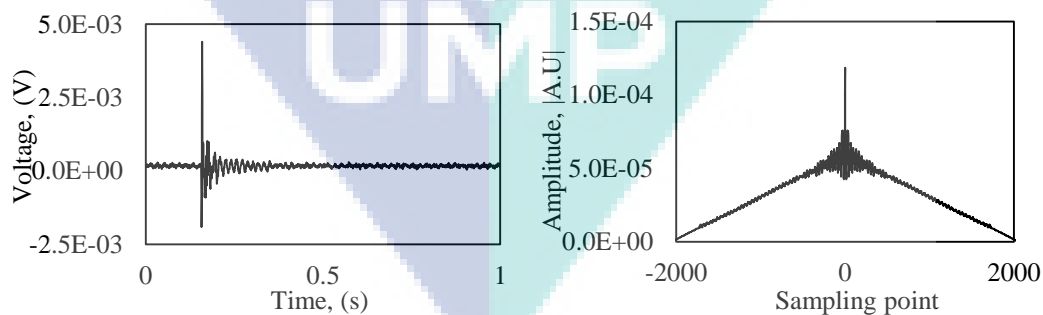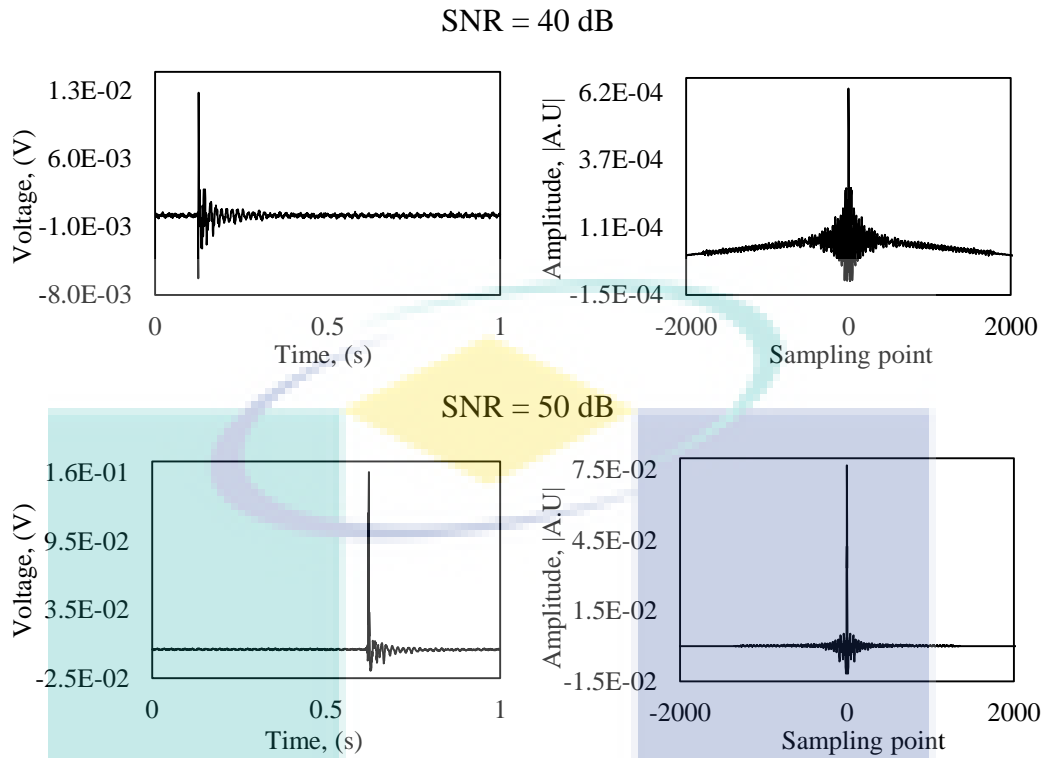
Figure 4.18   The performance of cross-correlation function at certain SNR values where the raw impact signal was illustrated on the left and the cross-correlation function at the right

Thus, the estimation of time delay was unattainable due to the appearance of noise in the background. As the value of SNR started to increase from 10 dB to 50 dB, the pointed peak of the cross-correlation began to emerge. The sharpest and most pointed peak was obtained at the SNR value of 50 dB. At the value of 50 dB, the side lobe of the cross-correlation had been suppressed to reduce the noise spectrum, which resulted in the sharp and pointed peak for accurate estimation of time delay. These results correlate with the findings by Sun et al. (2016) who performed the cross-correlation analysis with the settings of 0 dB SNR to 30 dB SNR, where the sharpest and most pointed peak was achieved at the highest SNR which was 30 dB (Sun et al., 2016). Thus, the SNR value of 50 dB was an adequate setting for the cross-correlation approach in this experimental work.

When an impact was made close to one of the sensor, a clear TOA between signal from FBG 1 and FBG 2 can be observed. Thus, the dispersion of impact signal will be early received by the nearest sensor to the impact source which is FBG 1 followed by FBG 2 and on the contrary when impact was hit at point B. Figure 4.19

illustrate the response of raw impact signal against sampling point when impact was induced at point A and B, respectively.
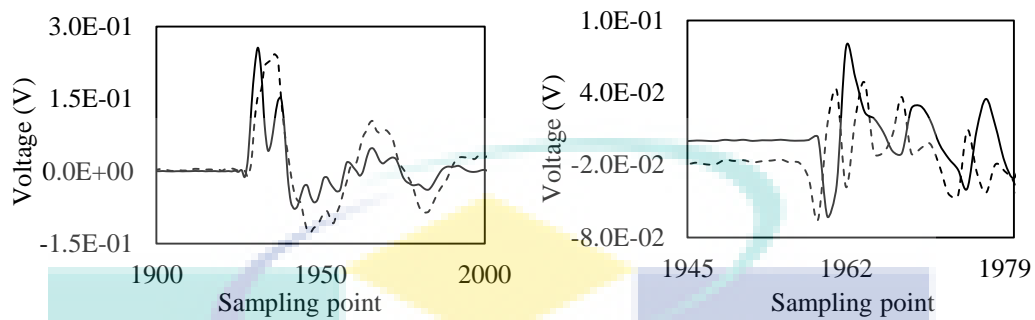
Indication:
Solid line = FBG 1 signal
Dashed line = FBG 2 signal

Figure 4.19   The response of raw impact signal for impact at: (a) Point A (b) Point B

The different in the arrival of time between the two peaks of the signals will be automatically estimated for the samples difference and time delay by cross-correlation function. Here, the cross-correlation function intensifies the highest peak of both the signals at a lag of zero and shift for the estimation of delay.

Figure 4.20 shows the illustration of cross-correlation signals in estimating the delay for all the impact points. For better illustration of the peak estimation, the sampling point of the cross-correlation signals have been reduced to the range of -20 to 20 samples. The blue colour marked indicate the cross-correlation signal when FBG 1 was utilized as the reference sensor while the red colour marked represents the signal when FBG 2 was set as the reference sensor.

(a)

(b)

(c)
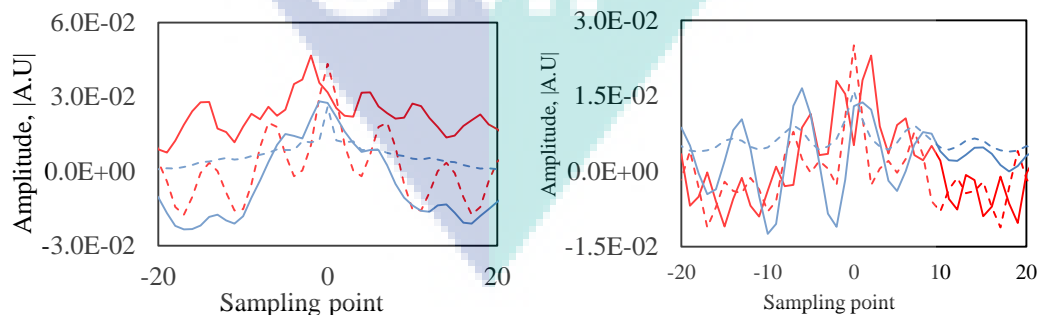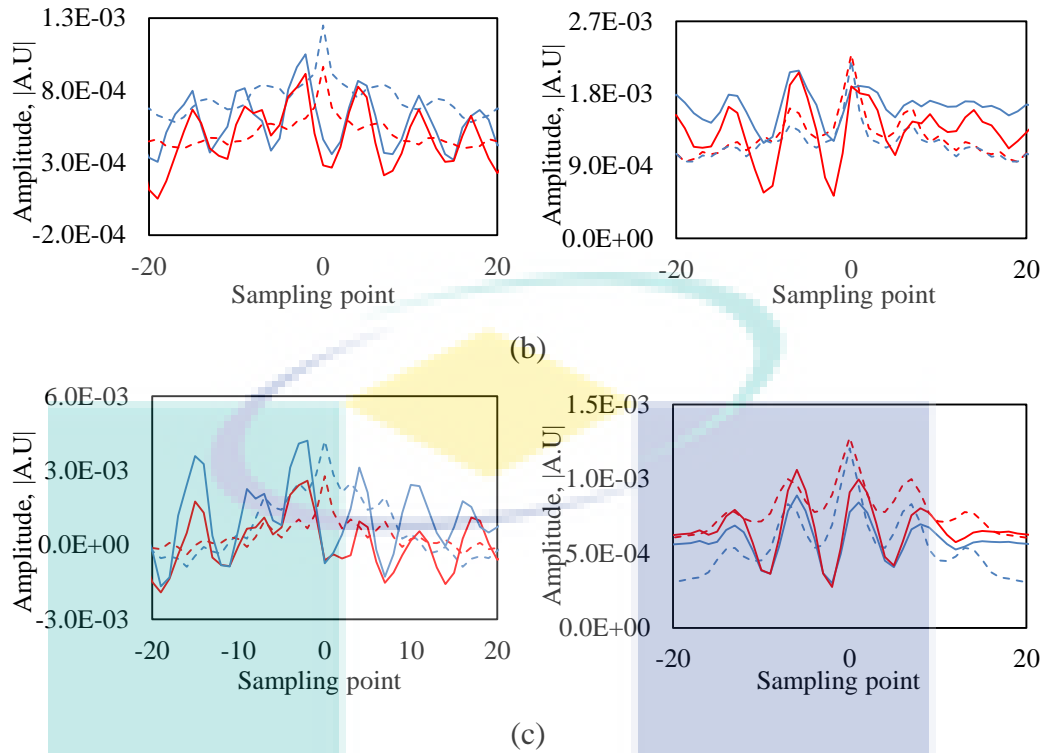
Indication:
Solid line = FBG 1 signal   Blue = FBG 1 as reference
Dashed line = FBG 2 signal   Red = FBG 2 as reference

Figure 4.20   The cross-correlation signals for impact at point: (a) A, J and B, K (b) D and E (c) G and H

From the results, clearly demonstrate that the cross-correlation amplified the peak of the raw signals to a sharp and pointed peak for the shift of delay estimation. In addition, clearly shows that when an impact was hit close to FBG 1, the arrival of the first peak for FBG 2 was certainly subsequent of FBG 1.

For all the trials made, cross-correlation algorithm demonstrating the consistency in estimating the sample difference of the peaks for all the impact points. A clear distinction can be observed for the samples difference and time delay between impact points that are made close to FBG 1 and impacts that are close to FBG 2. Larger samples difference and time delay are estimated for impacts that are made close to FBG 2 (point B, E, H and K) as compared to impacts that are close to FBG 1 (point A, D, G and J). This is due to the distance needed to be propagate by the signal. For instance, when the impact was made at point A, the signals needed to propagate for a distance of 9 cm to be captured by the FBG 1 and 21 cm to reach FBG 2. However, when impact at point B that was made 3 cm close to FBG 2, the signals required to propagate 27 cm in

order to reach FBG 1. This longer distance of propagation consequence in larger estimated time and samples difference. The highest time difference of 1.8 ms and 9 samples difference was estimated for impact at point H while the lowest time difference was 0.2 ms for impact at point G. Table 4.6 shows the summarization of the samples difference and time delay for all the impact points estimated by the cross-correlation algorithm.

Table 4.6   The summarization of the samples difference and time delay for all the impact points

Reference sensor	Impact point	Samples difference, D (samples)	Time difference, Δt (ms)
FBG 1	A	2	0.4
	B	4	0.8
	D	2	0.4
	E	3	0.6
	G	1	0.2
	H	9	1.8
FBG 2	J	3	0.6
	K	6	1.2
	D	2	0.4
	E	5	1.0
	G	2	0.1
	H	7	1.4

The values of the time difference estimation are strongly dependent on the sampling frequency. A high sampling frequency will give a higher resolution with more detail time of arrival whereas a low sampling frequency will give a larger time difference due to signal aliasing phenomena. A very good reliability and consistency were exhibited by the cross-correlation function where all trials for all the impact points permit similar repeatable results.

FBG sensor also illustrate an excellent dynamic strain measuring device in capturing frequency response better than conventional AE sensor due to its dominant working principle and selective directional property. Figure 4.21 shows the comparison of frequency spectrum between FBG and AE sensor at impact point C, for frequency range below 500 Hz and 500 to 1000 Hz. Obviously, the trend of curves from FBG sensor is similar to AE sensor for both the frequency range. However, frequency spectrum picked up by AE sensor has higher amplitude compared to FBG sensor. This phenomenon can be explained from the aspects of sensor attachment of both the sensors itself.
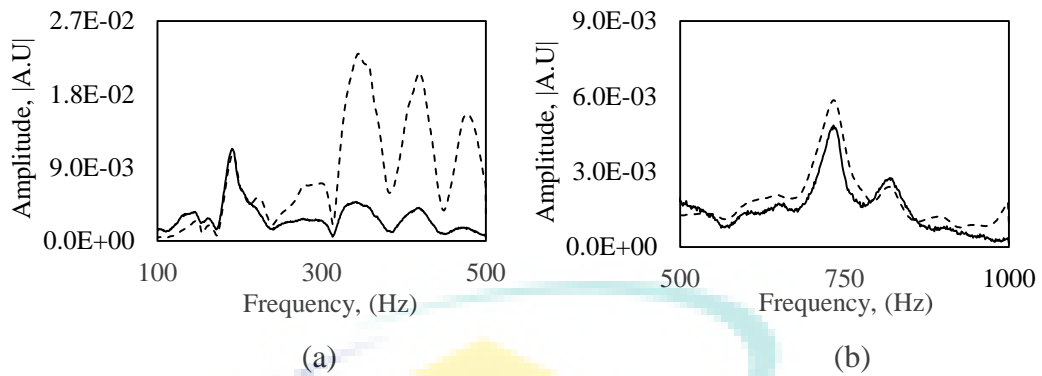
Indication:
Solid line = FBG sensor
Dashed line = AE sensor

Figure 4.21   The comparison of frequency spectrum between FBG and AE sensor at point C for frequency range of: (a) below 500 Hz (b) 500 to 1000 Hz

Surface-attached AE sensor will experience a more turbulent wave propagation as compared to embedded FBG sensor inside the composites. Fu et al. (2014) have performed a study of embedded and unembedded fibre optic acoustic emission sensors (FOAES) in identifying the impact source on carbon fibre reinforced polymer (CFRP) plate (Fu et al., 2014). The outcome of the frequency response results shows that the unembedded FOAES has higher amplitude than the embedded one. Furthermore, in a study by Ling at al. (2006) and Moyo et al. (2005) in comparing the frequency spectrum captured by surface mounted strain gauge and embedded FBG sensor shows that the embedded FBG has smaller amplitude (Ling et al., 2006; Moyo et al., 2005). However, for BVID flaw determination it is crucial for the signal to pass through the internal defect and captured by the sensor positioned as close as possible to the crack for true detection.

When a perpendicular left and right impacts was induced at point F and I, the frequency response picked up by the FBG sensor are exceptionally low in amplitude and barely sensitive. This is due to the selective directional property of the FBG sensor. Since the embedded FBG is in direction parallel to the beam, thus it is more sensitive to transverse and longitudinal wave that are in parallel direction with the sensor as compared to perpendicular wave. However, AE sensor capable in capturing the frequency response significantly without any loss of amplitude. Figure 4.22 shows the frequency response comparison between FBG and AE sensor at impact point F.
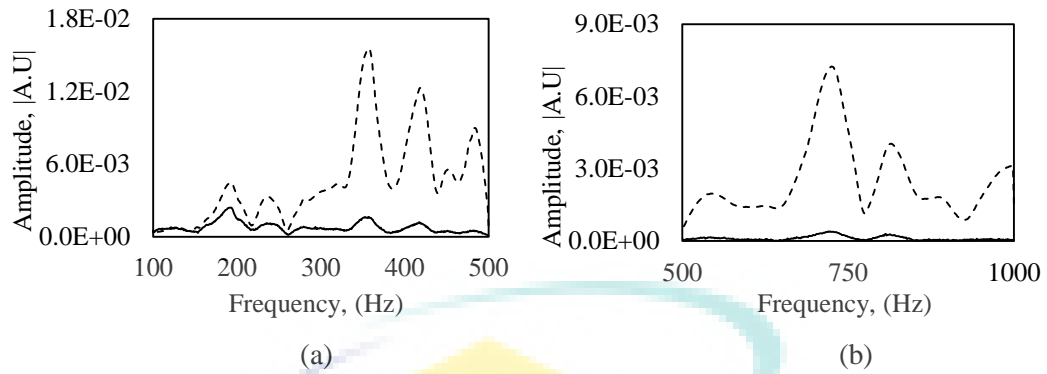
Indication:
Solid line = FBG sensor
Dashed line = AE sensor

Figure 4.22   The comparison of frequency spectrum between FBG and AE sensor at point F for frequency range of: (a) below 500 Hz (b) 500 to 1000 Hz

This due to working principle of the AE sensor that is independent on the direction of wave propagation. In the review by Balaji et al. (2016), the authors performed a study on the capability of transverse and radial pasted orientation of FBG sensor in capturing the elastic wave. The results revealed that different orientation of FBG sensor capturing propagated wave mode differently. The authors also emphasized that due to this certain wave picked by the FBG sensor, it is desirable and useful in detecting defects in structures (Balaji & Sasikumar, 2016).

Figure 4.23 shows the example of three trials of frequency response captured by the FBG sensor for point C and L that are located at the top and bottom surface of the beam which will results in parallel wave propagation when transverse impacts are induced. Point C was hit when FBG 1 was set as reference sensor denoted with blue colour line while point L denoted in red colour was hit when FBG 2 was set as reference sensor. From the overlay, clearly shows the capability of FBG sensor in capturing the frequency response repeatedly and consistently which gives the average frequency value of the first mode as 191.3 Hz, and 347.3 Hz, 415.8 Hz, 736.4 Hz, 837.9 Hz for the second, third, fourth and fifth mode respectively. The frequency response shows a sharp and pointed peak at the normal mode vibration which referred to the mode shape 1, 2, 3, 4 and 5 of the natural frequencies.
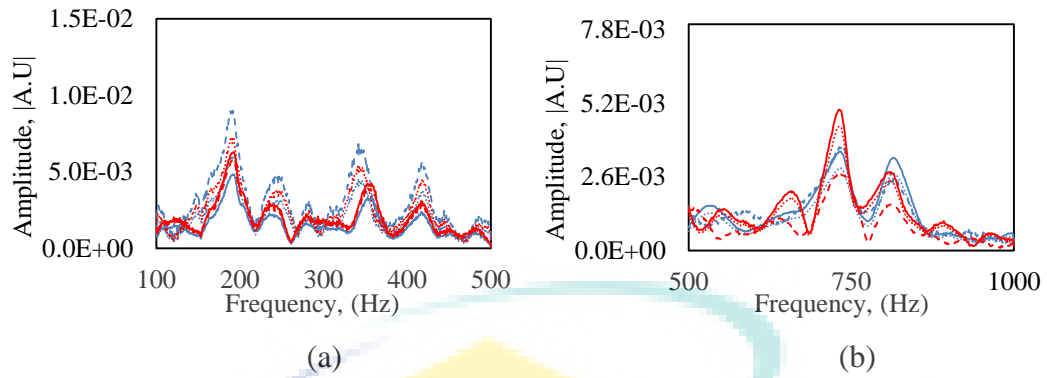
Indication:
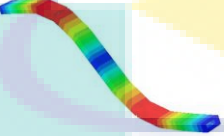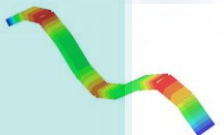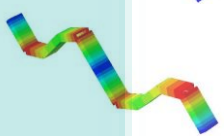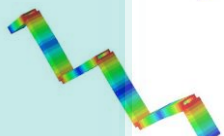
· · · · · · · · · · Trial 1   Blue = FBG 1 as reference

------ Trial 2   Red = FBG 2 as reference

——— Trial 3

Figure 4.23   The overlay of frequency response captured by FBG sensor for impact at point C and L for frequency range of: (a) below 500 Hz (b) 500 to 1000 Hz

Table 4.7 shows the validation with FEA analysis for simulated mode shape and natural frequency values. FEA analysis simulate the first natural frequency value as 187.22 Hz, and 350.46 Hz, 427.02 Hz, 702.31 Hz, 909.16 Hz for the second, third, fourth and fifth mode respectively. From the results, the comparison between FBG sensor with FEA simulation and FBG sensor with conventional AE sensor gave the percentage error which fell within the acceptable range of below 10%. The validation of experimental results for the percentage error of FBG sensor with AE sensor showed a very close natural frequency value, obtained with a percentage error of less than 1%. However, the validation of simulation results for percentage error between FBG sensor with FEA simulation shows the highest percentage of error at 7.84 %. This was due to the ideally fixed, boundary conditions of the FEA simulation that are totally free from any environmental influence. However, the results still fell within the acceptable range below 10%.

In order to estimate the impact location from equation 2.17, the group velocity of the waves, C_g has to be determined. Here, the group velocity was determined from the calculated PACshare Dispersion Curves software, as shown in Figure 4.24. Based on the validation, it was decided that the value of the first mode natural frequency of the beam was based on the experimental results obtained from the FBG sensor, which was 191.3 Hz, and which was used to interpolate the group velocity, C_g at 221.5 ms-1.

Table 4.7   The comparison between FEA analysis, FBG sensor and AE sensor natural frequency values

Mode shape	FEA simulation	Average natural frequency (Hz)			Error (%)	
		FEA	FBG sensor	AE sensor	FBG vs FEA	FBG vs AE
1		187.22	191.3	192.2	2.18	0.47
2		350.46	347.3	346.9	2.63	0.88
3		427.02	415.8	419.5	4.85	0.15
4		702.31	736.4	735.3	7.84	0.21
5		909.16	837.9	839.7	7.84	0.21
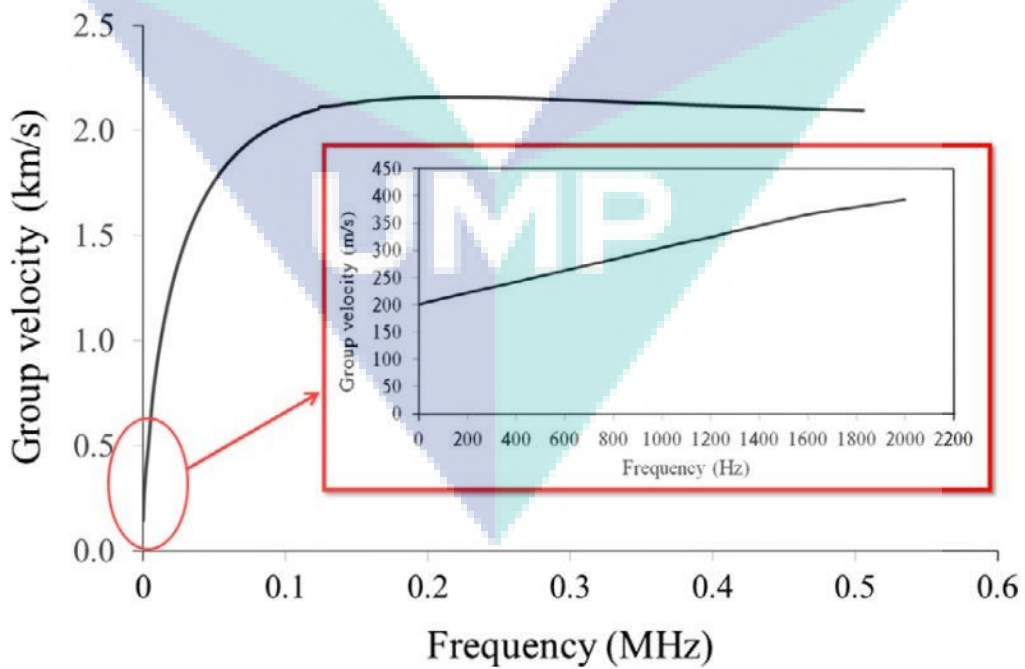
Figure 4.24   The group velocity curve calculated from the PACshare Dispersion Curves

Source: Hafizi et al. (2015).

99

Substitution of C_g, and Δt from cross-correlation into equation 2.16 summarises the linear source impact location as in Table 4.8 Since cross-correlation function estimated a constant time difference for all set of trials, thus a persistently measured distance was obtained for all the impact points. From the results, the estimation of impact points was close to the actual hit when FBG 2 was utilized as reference sensor with the highest relative error of only 1.97 %.

Table 4.8   The summarization of linear source impact location results

Reference sensor	Impact point	Actual (cm)	Estimated (cm)	Absolute error (cm)	Relative error (%)
FBG 1	A	9	10.57	1.57	1.44
	B	27	23.86	3.14	2.47
	D	9	10.57	1.57	1.44
	E	27	21.65	5.35	4.21
	G	9	12.79	3.79	3.48
	H	27	25.07	1.93	1.52
FBG 2	J	9	8.36	0.64	0.59
	K	27	28.29	1.29	1.02
	D	9	10.57	1.57	1.44
	E	27	26.10	0.9	0.71
	G	9	10.57	1.57	1.44
	H	27	29.50	2.50	1.97

A slight greater absolute error was obtained when FBG 1 was set as reference sensor as compared to FBG 2. The highest relative error was 4.21 % with absolute error of 5.35 cm away from the actual distance. All of the actual and estimated distance was measured from the position of FBG 1.

However, the estimation was still close to the actual hit even though top and bottom embedment of the sensors present a difficulty in impact estimation due to different wave propagation. All of the results revealed that it falls in the acceptable range of relative percentage of error which was below 10 %. For a clear illustration of the estimated impacts, an interpretation of all the discrepancies between all the actual points and estimated points are as in Figure 4.25. The triangular marker representing point A, J, D and G while the circular marker representing point B, K, E and H. The actual points are filled with black colour while the estimated point when FBG 1 was utilized as reference sensor are denoted in blue colour. The red colour marker representing the estimated points when FBG 2 was utilized as reference sensor. From the illustration, clearly shows that all the estimated hits were close to the actual

locations. Thus, the results certainly verified that the CC-LSL algorithm capable of estimating the impact location on the linear structure.

▲ Actual (Point A and J)
● Actual (Point B and K)
▲ Estimated (PointA) - FBG 1 as reference
▲ Estimated (Point J) - FBG 2 as reference
● Estimated (Point B) - FBG 1 as reference
● Estimated (Point K) - FBG 2 as reference

(a)

▲ Actual (Point D)
● Actual (Point E)
▲ Estimated (Point D) - FBG 1 as reference
▲ Estimated (Point D) - FBG 2 as reference
● Estimated (Point E) - FBG 1 as reference
● Estimated (Point E) - FBG 2 as reference

(b)

▲ Actual (Point G)
● Actual (Point H)
▲ Estimated (Point G) - FBG 1 as reference
▲ Estimated (Point G) - FBG 2 as reference
● Estimated (Point H) - FBG 1 as reference
● Estimated (Point H) - FBG 2 as reference

(c)

Figure 4.25   The illustration of discrepancies between actual and estimated impact points for: (a) Top and bottom surface (b) Left surface (c) Right surface

For the natural frequency excitation of the composite plate, Figure 4.26 shows the example of three trials for the natural frequency spectrum captured by FBG sensor and AE sensor simultaneously. Obviously, the same outcome as GFRP beam excitation results was obtained.
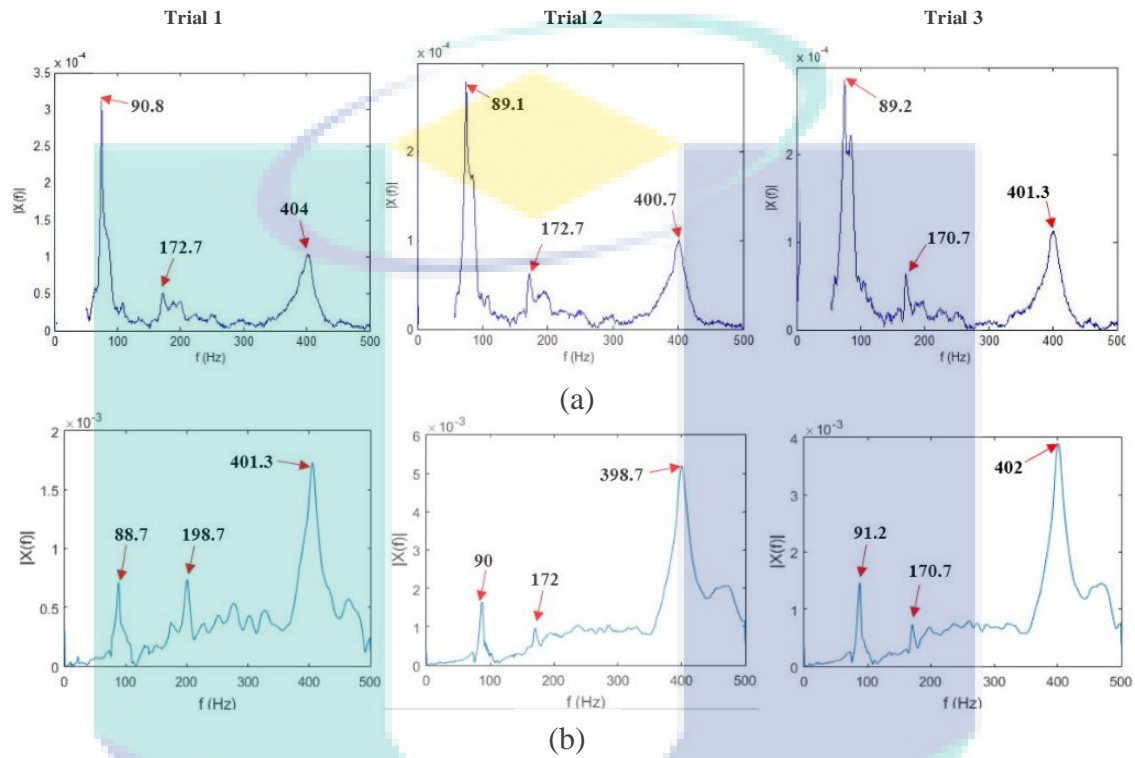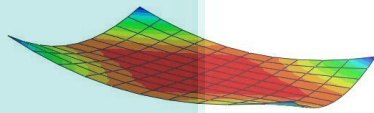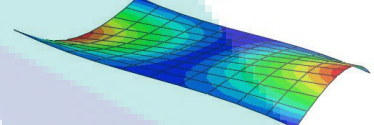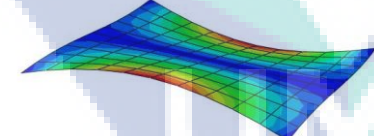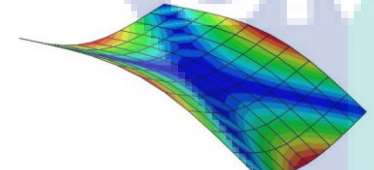
Figure 4.26   The natural frequency spectrum captured by: (a) FBG sensor (b) AE sensor

The frequency spectrum captured by the FBG sensor had the same significant profile as AE sensor. However, the frequency spectrum retrieved by the FBG sensor had a lower amplitude than that of the AE sensor. This is due to the same reason, that AE sensor was surface attached, and prompted the turbulent wave propagation. The experimental natural frequencies obtained by FBG and AE sensors were compared and validated with Abaqus FEA simulation, as summarized in Table 4.9.

Abaqus FEA has simulated 4 mode shapes of flexural wave propagation with the value of 99.5 Hz for the first natural frequency, and 181.02 Hz, 181.02 Hz, 373.81 Hz for the second, third and fourth natural frequency. From the simulation of the mode shapes, the plate underwent flexural propagation at mode shape 1 and mode shape 4, which exerted a natural axial strain on the sensors. This can be further justified from the

high amplitude of the first and last frequency spectrum's peak of both sensors. Kreuzer, in his review about FBG sensors in strain measurement, has stressed that FBG sensors are highly sensitive to lateral forces (Kreuzer, 2006). However, the FBG sensor is also competent in capturing slight twisting mode wave propagation, which is presented in mode shape 3 and mode shape 4, at the natural frequency value of 181.02 Hz, with a very small amplitude. Slight percentage error between FBG sensor and AE sensor was determined at twisting mode wave propagation at the value 4.69 %. The difference between FBG sensor with FEA simulation and FBG sensor with conventional AE sensor, where all of the percentage errors fell within the acceptable range of below 10%.

Table 4.9   The comparison of natural frequency values obtained from Abaqus FEA, FBG sensor and AE sensor for composite plate

Mode shape	FEA simulation	Average natural frequency (Hz)			Error (%)	
		FEA	FBG sensor	AE sensor	FBG vs FEA	FBG vs AE
1		99.5	89.7	89.87	9.85	0.19
2		181.02	172	180.47	5.08	4.69
3		181.02	172	180.47	5.08	4.69
4		373.81	402	400.7	7.54	0.32

The validation of simulation results for percentage error between FBG sensor and FEA simulation showed that the highest percentage error was at 9.85 %. This is due to the ideally fixed boundary conditions of the FEA simulation that are totally free from any environmental influences. However, the results still fell within the acceptable range of below 10%.

4.5   Chapter Summary

The experimental testing that was carried out to prove the proposed solutions had obtained satisfactory results for the improvement of both static strain sensing and dynamic strain sensing. A mesh-grid function which was proposed as a solution to replace the traditional way of viewing the gradual static strain measurement in the form of a spectrum, showed an interactive artificial virtual display of the structure undergoing deflection as the load was induced. The mesh-grid function has also been proven to have the capability of meshing any size and shape of a structure. Voltage normalization algorithm has increased the sensitivity of sensing measurement, from 2.4 mV/N to 3.8 mV/N across the 50 N loadings. Variations of output voltage had reduced from 26 data/minute to 17 data/minute. The main advantage of this method is the bypass of pre-calibration each time before use, with the percentage error of estimation at only 1.38 %.

The time delay of two signals using cross-correlation approach substitute in linear source location technique showed a great combination of an algorithm for low-velocity BVID impact estimation. The two impacts hit at a distance of 10.57 cm and 23.86 cm, estimated by the CC-LSL algorithm at a relative error value of 1.44 % and 2.47 % respectively. FBG sensor has also been proven to be a good dynamic measurement sensor in capturing normal mode flexural wave of a structure, compared to AE sensor. The comparison of natural frequency spectrum between FBG sensor and AE sensor exhibited a similar profile, where all the percentage errors fell within the acceptable range of less than 10 %. The natural frequency value obtained from the experimental results was compared to Abaqus FEA theoretical simulation and it was concluded that it was similar. The FBG sensor utilized in this study had the overall static sensitivity of 1.21 pm/$\mu\varepsilon$, and maximum dynamic sensitivity of 5 kHz.

CHAPTER 5

CONCLUSION

5.1   Conclusion

As introduced in the beginning of the chapter, the findings of this research work are based on three objectives, which are to develop an FBG based static and dynamic interrogation system for real-time composite structure monitoring, to enhance static strain measurement accuracy using mesh-grid function and voltage normalization algorithm, and to develop source location algorithm based on cross-correlation with a linear source location technique for the improvement of dynamic strain sensing. In general, the aim of this research work is to develop an improved FBG-based real-time monitoring system for both static and dynamic strain sensing. In summary, these three objectives have been achieved.

The first objective has demonstrated that two composite specimens embedded with FBG sensors in the shape of a plate and a beam were fabricated. The most economical and low-cost edge filter interrogation system was preferred and developed to monitor the static and dynamic strain condition of the composite structures. In the meantime, the monitoring system was coded with algorithm and function in MATLAB GUI, that function fully in real-time, and sensing information was retrieved instantly, making the FBG-based monitoring system efficient, and it could be operated by a less-skilled end user.

The second objective was achieved, where the mesh-grid function had successfully refurbished the typical way of representing the static strain deformation of a structure in the form of signal spectrum. The mesh-grid function represents the instant deformation of the structure under strain, by mapping the structure in an artificial virtual display. On the other hand, the voltage normalization algorithm had shown its

prominence in scaling down the output voltage variations due to high power light source. The normalization method had increased the accuracy of the FBG in static strain sensing and eliminate the necessity of pre-calibration each time before the operation.

For the objective of improving the dynamic strain sensing monitoring system, the integration of cross-correlation approach with linear source location technique testified that the CC-LSL algorithm was adequate and consistent in estimating impact location close to actual impact with percentage error of less than 10 %. This algorithm is applicable to linear structures such as rods, pipes, beams and struts on truss bridges. Moreover, natural frequency excitation had affirmed that FBG sensor is excellent in retrieving normal mode flexural wave propagation of the structure.

5.2   Future Work and Recommendations

Several suggestions and recommendations which can be considered as future work in order to bring these research findings to its level best. For the improvement in static strain sensing utilizing mesh-grid function, only a single FBG sensor was embedded at the centre of the plate, which allowed the strain mapping only at a single point. This approach is inadequate to monitor large structures in real-life application. Thus, multiplexed grating on a single fibre optic sensor, distributed at several positions of the structure will enable the strain monitoring to be implemented throughout the whole structure, and not limited to only a single position.

Although this experimental work was carried out at a controlled room temperature, the implementation in the real-life situation is far more challenging with possibly more extreme temperature condition. Thus, temperature compensation has to be considered to differentiate if the Bragg grating elongation is due to the change of temperature or strain alone. Several amendments can be made, such as contrasting the strain sensing FBG with a reference FBG, or using a temperature compensated algorithm.

On the other hand, for the dynamic strain sensing, several improvements can be made on the cross-correlation approach, particularly on the suppression of noise and sharpening of the peak for accuracy in delay estimation. Improved techniques to filter the noise through filter analysis method, such as wavelet domain, Hilbert-Huang transform, phase transform (PHAT), ROTH filter (ROTH), ECKART filter (ECKART)

and other techniques can be implemented. For a more advanced impact localization method, multiple simultaneous impacts detection can be implemented.

Lastly, it is hoped that with sufficient financial support and opportunity given, a field test on real-life engineering structure such as monitoring of the bridge deflection due to heavy traffic, excessive aircraft wing deformation during in-flight, railway deformation monitoring, bird strike on composite aircraft, and impact hit on civil construction can be implemented for this research findings to be applied out of laboratory testing. However, all in all, with the current results, it is well-proven that the proposed solutions are capable of overcoming the drawbacks of the current FBG-based monitoring system, as mentioned in the earlier chapter.
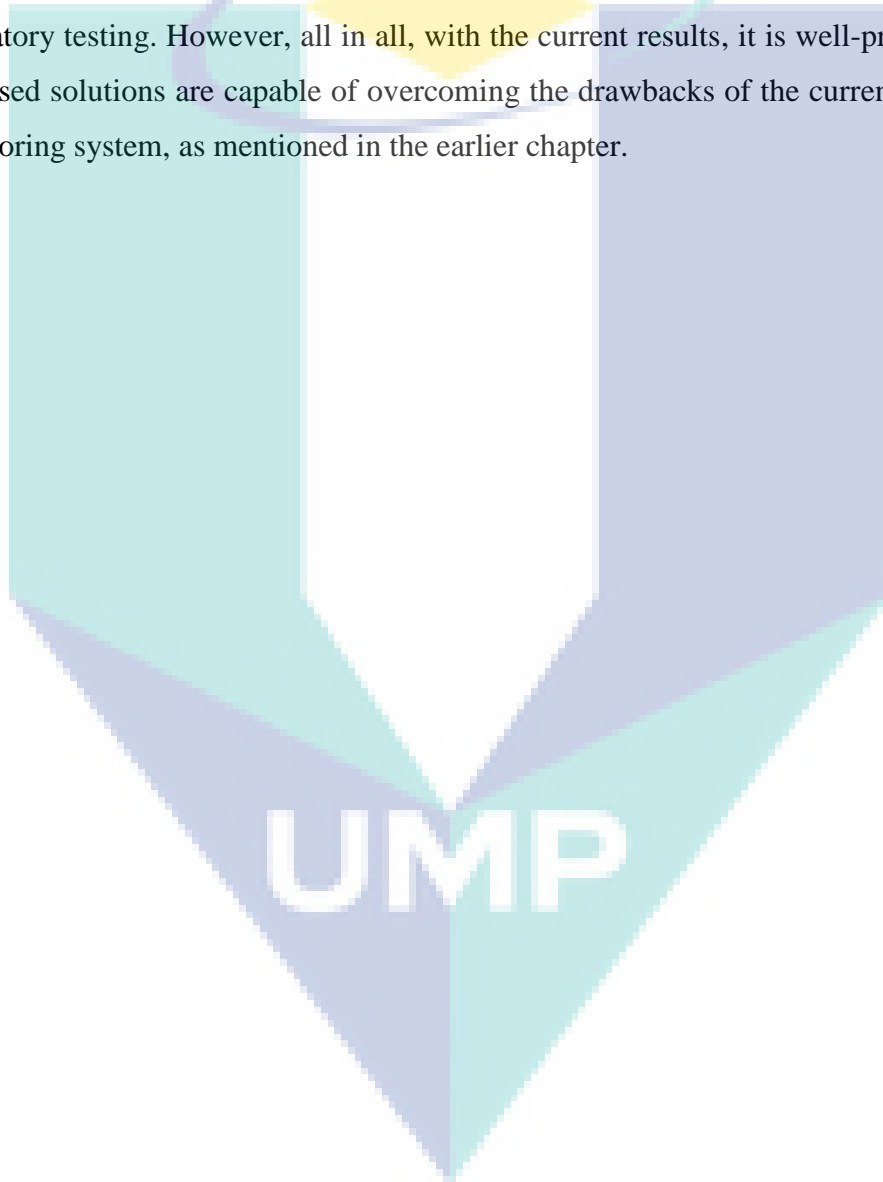
REFERENCES

Akhras, G. (2012). Smart NDE systems – Applications in aerospace and perspectives.

Alfredo, L., Chiesura, G., Luyckx, G., Degrieck, J., Kaufmann, M., & Vanlanduit, S. (2015). Dynamic strain measurements on automotive and aeronautic composite components by means of embedded fiber Bragg grating sensors. *Sensors, 15*(10), 27174-27174.

Aljets, D., Chong, A., Wilcox, S., & Holford, K. (2010). Acoustic emission source location in plate-like structures using a closely arranged triangular sensor array. *Journal of Acoustic Emission, 28*, 85-98.

Allwood, G., Wild, G., Lubansky, A., & Hinckley, S. (2015). A highly sensitive fiber Bragg grating diaphragm pressure transducer. *Optical Fiber Technology, 25*, 25-32.

Anderson, E. H., & Sater, J. M. (2007, 2007). *Smart structures product implementation award: A review of the first ten years.* Paper presented at the The 14th International Symposium on: Smart Structures and Materials & Nondestructive Evaluation and Health Monitoring.

Askins, C. G., Putnam, M. A., & Friebele, E. J. (1995). *Instrumentation for interrogating many element fiber bragg grating arrays.* Paper presented at the Smart Structures & Materials' 95, San Diego, CA, United States.

Bahrampour, A. R., Tofighi, S., Bathaee, M., & Farman, F. (2012). Optical fiber interferometers and their applications *Interferometry-Research and Applications in Science and Technology*: InTech.

Baker, A. A. (2004). *Composite materials for aircraft structures*: AIAA.

Bakis, C., Bank, L. C., Brown, V., Cosenza, E., Davalos, J. F., Lesko, J. J., . . . Triantafillou, T. C. (2002). Fiber-reinforced polymer composites for construction state-of-the-art review. *Journal of Composites for Construction, 6*(2), 73-87.

Balaji, R., & Sasikumar, M. (2016). Structural health monitoring (SHM) system for polymer composites: A review. *Indian Journal of Science and Technology; Volume 9, Issue 41, November 2016*.

Bao, P., Yuan, M., Dong, S., Song, H., & Xue, J. (2013). Fiber Bragg grating sensor fatigue crack real-time monitoring based on spectrum cross-correlation analysis. *Journal of Sound and Vibration, 332*(1), 43-57.

Bram, V. H., Lee, G., Bosman, E., Missinne, J., Kalathimekkad, S., Maskery, O., . . . Van Steenberge, G. (2012). Ultra small integrated optical fiber sensing system. *Sensors, 12*(9), 12052-12069.

Brondsted, P., Lilholt, H., & Lystrup, A. (2005). Composite materials for wind power turbine blades. *Annual Review of Materials Research, 35*(1), 505-538.

Brown, J. (1997). *Characterization of MSC/NASTRAN & MSC/ABAQUS elements for turbine engine blade frequency analysis.* Paper presented at the In Proc. MSC Aerospace Users' Conference.

Busquin, P. (2001). European aeronautics: A vision for 2020

Cai, J., Qiu, L., Yuan, S., Liu, P., Liang, D., & Shi, L. (2012). Structural health monitoring for composite materials.

Campbell, F. C. (2010). *Structural composite materials*: ASM international.

Campopiano, S., Cutolo, A., Cusano, A., Giordano, M., Parente, G., Lanza, G., & Laudati, A. (2009). Underwater acoustic sensors based on fiber Bragg gratings. *Sensors, 9*(6), 4446-4454.

Caucheteur, C., Chah, K., Lhommé, F., Blondel, M., & Mégret, P. (2004). Autocorrelation demodulation technique for fiber Bragg grating sensor. *IEEE Photonics Technology Letters, 16*(10), 2320-2322.

Cazzulani, G., Cinquemani, S., & Comolli, L. (2012, 2012). *Enhancing active vibration control performances in a smart structure by using fiber Bragg gratings sensors.* Paper presented at the SPIE Smart Structures and Materials+ Nondestructive Evaluation and Health Monitoring.

Chan, T. H. T., Yu, L., Tam, H. Y., Ni, Y. Q., Liu, S. Y., Chung, W. H., & Cheng, L. K. (2006). Fiber Bragg grating sensors for structural health monitoring of Tsing Ma bridge: Background and experimental observation. *Engineering Structures, 28*(5), 648-659.

Chandrashekhar, M., & Ganguli, R. (2016). Damage assessment of composite plate structures with material and measurement uncertainty. *Mechanical Systems and Signal Processing, 75*, 75-93.

Chen, W., & Dong, X. (2012). Modification of the wavelength-strain coefficient of FBG for the prediction of steel bar corrosion embedded in concrete. *Optical Fiber Technology, 18*(1), 47-50.

Cheng, W. C., & Ni, J. C. (2009). Feasibility study of applying SOFO optical fiber sensor to segment of shield tunnel. *Tunnelling and Underground Space Technology, 24*(3), 331-349.

Chuang, K. C., Liao, H. T., & Ma, C. C. (2011). Dynamic sensing performance of a point-wise fiber Bragg grating displacement measurement system integrated in an active structural control system. *Sensors, 11*(12), 11605-11628.

Chudoba, R., Sharei, E., & Scholzen, A. (2016). A strain hardening microplane damage model for thin walled textile reinforced concrete shells, calibration procedure, and experimental validation. *Composite Structures, 152*, 913-928.

Chung, W., & Kang, D. (2008). Full-scale test of a concrete box girder using FBG sensing system. *Engineering Structures, 30*(3), 643-652.

Ciang, C. C., Lee, B. H., & Bang, H. J. (2008). Structural health monitoring for a wind turbine system: A review of damage detection methods. *Measurement Science and Technology, 19*(12), 122001-122001.

Comanici, M. I., Chen, L. R., Kung, P., & Wang, L. (2011). *Measurement of dynamic strain using a fiber Bragg grating-based laser sensor system.* Paper presented at the 2011 ICO International Conference on Information Photonics.

Costa, B. J. A., & Figueiras, J. A. (2012a). Evaluation of a strain monitoring system for existing steel railway bridges. *Journal of Constructional Steel Research, 72*, 179-191.

Costa, B. J. A., & Figueiras, J. A. (2012b). Fiber optic based monitoring system applied to a centenary metallic arch bridge: Design and installation. *Engineering Structures, 44*, 271-280.

Culshaw, B., & Kersey, A. (2008). Fiber-optic sensing: A historical perspective. *Journal of lightwave technology, 26*(9), 1064-1078.

Cusano, A., Cutolo, A., & Albert, J. (2011). *Fiber Bragg grating sensors: Recent advancements, industrial applications and market exploitation*: Bentham Science Publishers.

Cvijetic, M. (2004). *Optical transmission systems engineering*: Artech House.

Dai, Y., Li, P., Liu, Y., Asundi, A., & Leng, J. (2014). Integrated real-time monitoring system for strain/temperature distribution based on simultaneous wavelength and time division multiplexing technique. *Optics and Lasers in Engineering, 59*, 19-24.

de Moura, M. F. S. F., & Goncalves, J. P. M. (2004). Modelling the interaction between matrix cracking and delamination in carbon-epoxy laminates under low velocity impact. *Composites Science and Technology, 64*(7-8), 1021-1027.

Deng, W., Peng, W., Zhang, Y., Qiu, B., & Xue, H. (2012). A brief review of the application and problems in ultrasonic fatigue testing. *AASRI Procedia, 2*, 127-133.

Donaldson, S. L., & Miracle, D. B. (2001). ASM handbook composites (Vol. 21, pp. 1100): ASM International.

Ezbiri, A., Kanellopoulos, S., & Handerek, V. (1998). High resolution instrumentation system for fibre-Bragg grating aerospace sensors. *Optics communications, 150*(1), 43-48.

Fernandes, R. L., de Moura, M. F. S. F., & Moreira, R. D. F. (2016). Effect of moisture on pure mode I and II fracture behaviour of composite bonded joints. *International Journal of Adhesion and Adhesives, 68*, 30-38.

Fillinger, L., Sutin, A., & Sedunov, A. (2009). Cross-correlation of ship noise for water traffic monitoring. 158th Meeting Lay Language Papers.

Filograno, M. L., Barrios, A. R., Herraez, M. G., Corredera, P., Lopez, S. M., Plaza, M. R., & Alguacil, A. A. (2012, 2010). *Real time monitoring of railway traffic using fiber Bragg grating sensors*. Paper presented at the 2010 Joint Rail Conference.

Frieden, J., Cugnoni, J., Botsis, J., & Gmur, T. (2012). Low energy impact damage monitoring of composites using dynamic strain signals from FBG sensors-Part I: Impact detection and localization. *Composite Structures, 94*(2), 438-445.

Frieden, J., Cugnoni, J., Botsis, J., Gmur, T., & Coric, D. (2010). High-speed internal strain measurements in composite structures under dynamic load using embedded FBG sensors. *Composite Structures, 92*(8), 1905-1912.

Fu, T., Liu, Y., Lau, K. T., & Leng, J. (2014). Impact source identification in a carbon fiber reinforced polymer plate by using embedded fiber optic acoustic emission sensors. *Composites Part B: Engineering, 66*, 420-429.

Gilewski, W., & Zawadzka, A. A. S. (2015). On possible applications of smart structures controlled by self-stress. *Archives of Civil and Mechanical Engineering, 15*(2), 469-478.

Glisic, B., & Inaudi, D. (2008). *Fibre optic methods for structural health monitoring*: John Wiley & Sons.

Gu, Y., & Liu, G.-R. (2001). A meshless local Petrov-Galerkin (MLPG) method for free and forced vibration analyses for solids. *Computational Mechanics, 27*(3), 188-198.

Guo, H., Xiao, G., Mrad, N., & Yao, J. (2011). Fiber optic sensors for structural health monitoring of air platforms. *Sensors, 11*(4), 3687-3687.

Hafizi, Z. M. (2014). *The applications of near infra-red fibre Bragg grating sensors for wave propagation based structural health monitoring of thin laminated composite plates.*

Hafizi, Z. M., Epaarachchi, J., & Lau, K. T. (2015). Impact location determination on thin laminated composite plates using an NIR-FBG sensor system. *Measurement, 61*, 51-57.

Hai, N. D., Mutsuyoshi, H., Asamoto, S., & Matsui, T. (2010). Structural behavior of hybrid FRP composite I-beam. *Construction and Building Materials, 24*(6), 956-969.

Hayes, J., & Works, V. D. V. (2002). Understanding wavelengths in fiber optics: The Fiber Optic Association.

Henderson, P. J., Webb, D. J., Jackson, D. A., Zhang, L., & Bennion, I. (1999). *Highly multiplexed grating sensors for temperature referenced quasi-static measurements of strain in concrete bridges*.

Henke, R. (2016). Advisory council for aviation research and innovation in Europe.

Huang, C., Jing, W., Liu, K., Zhang, Y., & Peng, G. (2007). Demodulation of fiber Bragg grating sensor using cross-correlation algorithm. *IEEE Photonics Technology Letters, 19*(9/12), 707.

Huang, W., Zhang, W., Zhen, T., Zhang, F., & Li, F. (2014). A cross-correlation method in wavelet domain for demodulation of FBG-FP static strain sensors. *IEEE Photonics Technology Letters, 26*(16), 1597-1600.

Hull, D., & Clyne, T. W. (1996). An introduction to composite materials: Cambridge University Press.

Iacoviello, F., Reis, L., Fonte, M., Freitas, M., Infante, V., & Gholizadeh, S. (2016). A review of non-destructive testing methods of composite materials. *Procedia Structural Integrity, 1*, 50-57.

Ianniello, J. (1982). Time delay estimation via cross-correlation in the presence of large estimation errors. *IEEE Transactions on Acoustics, Speech, and Signal Processing, 30*(6), 998-1003.

Ioffe, S., & Szegedy, C. (2015). Batch normalization: Accelerating deep network training by reducing internal covariate shift. *In International Conference on Machine Learning*, 448-456.

James, S. W., Tatam, R. P., Fuller, S. R., & Crompton, C. (1999). Monitoring transient strains on a gun barrel using fibre Bragg-grating sensors. *Measurement Science and Technology, 10*(2), 63-63.

Jian, Z., & Hong, Z. (2009). *Matched FBG application research on dynamic sensing and demodulation.* Paper presented at the Photonics and Optoelectronics, 2009. SOPO 2009. Symposium on.

Jiang, M., Lu, S., Sui, Q., Dong, H., Sai, Y., & Jia, L. (2015). Low velocity impact localization on CFRP based on FBG sensors and ELM algorithm. *IEEE Sensors Journal, 15*(8), 4451-4456.

Jiang, M., Sai, Y., Geng, X., Sui, Q., Liu, X., & Jia, L. (2016). Development of an FBG sensor srray for multi-impact source localization on CFRP structures. *Sensors, 16*(10), 1770-1770.

Jim, J. (2014). End to end system design.

Jones, R. M. (1998). Mechanics of composite materials: Taylor & Francis Inc.

Kahandawa, G. C. (2012). *Monitoring damage in advanced composite structures using embedded fibre optic sensors.*

Kahandawa, G. C., Epaarachchi, J., Wang, H., Followell, D., & Birt, P. (2013). Use of fixed wavelength fibre Bragg grating (FBG) filters to capture time domain data from the distorted spectrum of an embedded FBG sensor to estimate strain with an artificial neural network. *Sensors and Actuators A: Physical, 194*, 1-7.

Kahandawa, G. C., Epaarachchi, J., Wang, H., & Lau, K. T. (2012). Use of FBG sensors for SHM in aerospace structures. *Photonic Sensors, 2*(3), 203-214.

Kavitha, S., Joseph Daniel, R., & Sumangala, K. (2016). High performance MEMS accelerometers for concrete SHM applications and comparison with COTS accelerometers. *Mechanical Systems and Signal Processing, 66*(Supplement C), 410-424.

Keller, T. (2003). *Use of fibre reinforced polymers in bridge construction*: International Association for Bridge and Structural Engineering.

Kersey, A. D., Berkoff, T. A., & Morey, W. W. (1993). Multiplexed fiber Bragg grating strain sensor system with a fiber Fabry-Perot wavelength filter. *Optics letters, 18*(16), 1370-1372.

Kesavan, K., Ravisankar, K., Senthil, R., & Farvaze, A. K. (2013). Experimental studies on performance of reinforced concrete beam strengthened with CFRP under cyclic loading using FBG array. *Measurement, 46*(10), 3855-3862.

Khan, M. T. I., Sunichi, N., & Hasan, M. (2014). Structural damage localization by linear technique of acoustic emission. *Open Journal of Fluid Dynamics, 4*(05), 425.

Kim, C.-Y., Jung, D.-S., Kim, N.-S., Kwon, S.-D., & Feng, M. Q. (2003). Effect of vehicle weight on natural frequencies of bridges measured from traffic-induced vibration. *Earthquake Engineering and Engineering Vibration, 2*(1), 109-115.

Kinet, D., Megret, P., Goossen, K., Qiu, L., Heider, D., & Caucheteur, C. (2014). Fiber Bragg grating sensors toward structural health monitoring in composite materials: Challenges and solutions. *Sensors, 14*(4), 7394-7394.

Kirkby, E., de Oliveira, R., Michaud, V., & Manson, J. A. (2011). Impact localisation with FBG for a self-healing carbon fibre composite structure. *Composite Structures, 94*(1), 8-14.

Kreuzer, M. (2006). Strain measurement with fiber Bragg grating sensors.

Kroeger, T. (2014). Thermographic inspection of composites. *Reinforced Plastics, 58*(4), 42-43.

Lamberti, A., Vanlanduit, S., De Pauw, B., & Berghmans, F. (2014). A novel fast phase correlation algorithm for peak wavelength detection of fiber Bragg grating sensors. *Optics express, 22*(6), 7099-7112.

Lau, K. T. (2003). Fibre-optic sensors and smart composites for concrete applications. *Magazine of concrete Research, 55*(1), 19-34.

Lau, K. T., Yuan, L., Li, M. Z., Wu, J., & Chung, H. W. (2001). Strain monitoring in FRP laminates and concrete beams using FBG sensors. *Composite Structures, 51*(1), 9-20.

Lee, Jeong, Y., Yin, S., Ruffin, P. B., & Yu, F. T. S. (2008). Interrogation techniques for fiber grating sensors and the theory of fiber gratings. *Fiber Optic Sensors. Taylor & Francis*, 253-331.

Lee, S. C. J. (2009). *Discrete multitone modulation for short range optical communications.* (Phd), Eindhoven University of Technology.

Lee, S. K., & Park, J. H. (2011). *Source localization for multiple impacts based on elastodynamics and wavelet analysis.* Paper presented at the Advances in Mechanical Engineering.

Li, L., Zhang, D., Liu, H., Guo, Y., & Zhu, F. (2014). Design of an enhanced sensitivity FBG strain sensor and application in highway bridge engineering. *Photonic Sensors, 4*(2), 162-167.

Li, Y., Liu, W., Feng, Y., & Zhang, H. (2012). Ultrasonic embedding of nickel-coated fiber Bragg grating in aluminum and associated sensing characteristics. *Optical Fiber Technology, 18*(1), 7-13.

Lim, J. H., Jang, H. S., Lee, K. S., Kim, J. C., & Lee, B. H. (2004). Mach-zehnder interferometer formed in a photonic crystal fiber based on a pair of long-period fiber gratings. *Optics Letters, 29*(4), 346-348.

Ling, H. Y., Lau, K. T., Cheng, L., & Jin, W. (2006). Viability of using an embedded FBG sensor in a composite structure for dynamic strain measurement. *Measurement, 39*(4), 328-334.

Liu, P. F., Liao, B. B., Jia, L. Y., & Peng, X. Q. (2016). Finite element analysis of dynamic progressive failure of carbon fiber composite laminates under low velocity impact. *Composite Structures, 149*, 408-422.

Liu, Q., He, Z., & Tokunaga, T. (2015). Sensing the earth crustal deformation with nano-strain resolution fiber-optic sensors. *Optics Express, 23*(11), A428-A436.

Lu, S., Jiang, M., Sui, Q., Sai, Y., & Jia, L. (2015). Low velocity impact localization system of CFRP using fiber Bragg grating sensors. *Optical Fiber Technology, 21*, 13-19.

Lubin, G. (2013). *Handbook of composites*: Springer Science & Business Media.

Luyckx, G., Voet, E., Lammens, N., & Degrieck, J. (2011). Strain measurements of composite laminates with embedded fibre Bragg gratings: Criticism and opportunities for research. *Sensors, 11*(1), 384-384.

Ma, J., Zhao, M., Huang, X., Bae, H., Chen, Y., & Yu, M. (2016). Low cost, high performance white-light fiber-optic hydrophone system with a trackable working point. *Optics Express, 24*(17), 19008-19019.

Ma, P., Wang, X., Ma, Y., Zhou, P., & Liu, Z. (2014). Analysis of multi-wavelength active coherent polarization beam combining system. *Optics Express, 22*(13), 16538-16551.

MacChesney, J. (2006). Fibe optics: The basics of fiber optic cable

Machida, A., & Uomoto, T. (1997). *Recommendation for design and construction of concrete structures using continuous fiber reinforcing materials* (Vol. 23).

Majumder, M., Gangopadhyay, T. K., Chakraborty, A. K., Dasgupta, K., & Bhattacharya, D. K. (2008). Fibre Bragg gratings in structural health monitoring - Present status and applications. *Sensors and Actuators A: Physical, 147*(1), 150-164.

Mangalgiri, P. (1999). Composite materials for aerospace applications. *Bulletin of Materials Science, 22*(3), 657-664.

Mike, J., Senior, F., & Micrel, I. (2007). Running ethernet over plastic optical fiber. http://www.embedded.com/print/4009951

Mininni, M., Gabriele, S., Lopes, H., & Araujo, d. S. J. V. (2016). Damage identification in beams using speckle shearography and an optimal spatial sampling. *Mechanical Systems and Signal Processing, 79*, 47-64.

Moon, Y. S., Lee, S. K., Shin, K., & Lee, Y. S. (2011). Identification of multiple impacts on a plate using the time-frequency analysis and the Kalman filter. *Journal of Intelligent Material Systems and Structures, 22*(12), 1283-1291.

Moyo, P., Brownjohn, J. M. W., Suresh, R., & Tjin, S. C. (2005). Development of fiber Bragg grating sensors for monitoring civil infrastructure. *Engineering Structures, 27*(12), 1828-1834.

National Instruments. (2011). Overview of fiber optic sensing technologies. http://www.ni.com/white-paper/12953/en/

National Instruments. (2016). FBG optical sensing: A new alternative for challenging strain measurements.

Nishizaki, I. (2009). Life-cycle cost assessment for FRP structures. *Proceedings of US-Japan Workshop on Life Cycle Assessment of Sustainable Infrastructure Materials*.

Orifici, A. C., Herszberg, I., & Thomson, R. S. (2008). Review of methodologies for composite material modelling incorporating failure. *Composite Structures, 86*(1-3), 194-210.

Papantoniou, A., Rigas, G., & Alexopoulos, N. D. (2011). Assessment of the strain monitoring reliability of fiber Bragg grating sensor (FBGs) in advanced composite structures. *Composite Structures, 93*(9), 2163-2172.

Park, J. M., Lee, S. I., Kwon, O. Y., Choi, H. S., & Lee, J. H. (2003). Comparison of nondestructive microfailure evaluation of fiber-optic Bragg grating and acoustic emission piezoelectric sensors using fragmentation test. *Composites Part A: Applied Science and Manufacturing, 34*(3), 203-216.

Pelz, C. R., Molly, K. M., Bagby, G., & Sears, R. C. (2008). Global rank invariant set normalization (GRSN) to reduce systematic distortions in microarray data. *BMC bioinformatics, 9*(1), 1-1.

Pereira, G., Frias, C., Faria, H., Frazao, O., & Marques, A. T. (2013). On the improvement of strain measurements with FBG sensors embedded in unidirectional composites. *Polymer Testing, 32*(1), 99-105.

Pilkey, W. D. (2005). *Formulas for stress, strain, and structural matrices*: Wiley.

Qapo, M., Dirar, S., & Jemaa, Y. (2016). Finite element parametric study of reinforced concrete beams shear-strengthened with embedded FRP bars. *Composite Structures, 149*, 93-105.

Qingwen, L., Tokunaga, T., & He, Z. (2011). Ultra high resolution large dynamic range optical fiber static strain sensor using Pound Drever Hall technique. *Optics letters, 36*(20), 4044-4046.

Raffaella, D. S. (2015). Fibre optic sensors for structural health monitoring of aircraft composite structures: Recent advances and applications. *Sensors, 15*(8), 18666-18666.

Raffaella, D. S., & Donati, L. (2013). Strain monitoring with embedded fiber Bragg gratings in advanced composite structures for nautical applications. *Measurement, 46*(7), 2118-2126.

Raffaella, D. S., Donati, L., Troiani, E., & Proli, P. (2014). Evaluation of bending strain measurements in a composite sailboat bowsprit with embedded fibre Bragg gratings. *Measurement, 54*, 106-117.

Raffaella, D. S., & Scalise, L. (2004). A novel fiber optic sensor for multiple and simultaneous measurement of vibration velocity. *Review of scientific instruments, 75*(6), 1952-1958.

Ramakrishnan, M., Rajan, G., Semenova, Y., Boczkowska, A., Domanski, A., Wolinski, T., & Farrell, G. (2013). Measurement of thermal elongation induced strain of a composite material using a polarization maintaining photonic crystal fiber sensor. *Sensors and Actuators A: Physical, 190*, 44-51.

Ramakrishnan, M., Rajan, G., Semenova, Y., & Farrell, G. (2016). Overview of fiber optic sensor technologies for strain/temperature sensing applications in composite materials. *Sensors, 16*(1), 99-99.

Ramakrishnan, M., Rajan, G., Semenova, Y., Lesiak, P., Domanski, A., Wolinski, T., . . . Farrell, G. (2011). The influence of thermal expansion of a composite material on embedded polarimetric sensors. *Smart Materials and Structures, 20*(12), 125002-125002.

Rao, Y. J. (1999). Recent progress in applications of in-fibre Bragg grating sensors. *Optics and Lasers in Engineering, 31*(4), 297-324.

Ray, B. C. (2006). Temperature effect during humid ageing on interfaces of glass and carbon fibers reinforced epoxy composites. *Journal of Colloid and Interface Science, 298*(1), 111-117.

Reddy, J. N. (2004). *Mechanics of laminated composite plates and shells: Theory and analysis*: CRC press.

Ren, L., Jia, Z. G., Li, H. N., & Song, G. (2014). Design and experimental study on FBG hoop-strain sensor in pipeline monitoring. *Optical Fiber Technology, 20*(1), 15-23.

Rezayat, A., Pauw, B. D., Lamberti, A., El-Kafafy, M., Nassiri, V., Ertveldt, J., . . . Guillaume, P. (2016). Reconstruction of impacts on a composite plate using fiber Bragg gratings (FBG) and inverse methods. *Composite Structures, 149*, 1-10.

Ribeiro, F., Possetti, G. R. C., Fabris, J. L., & Muller, M. (2013). *Smart optical fiber sensor for impact localization on planar structures.* Paper presented at the International Microwave Optoelectronics Conference (IMOC).

Roberts, T. (2011). The carbon fiber industry worldwide 2011-2020. *Materials Technology Publications, Watford, 6*, 29-29.

Rodrigues, C., Cavadas, F., Felix, C., & Figueiras, J. (2012). FBG based strain monitoring in the rehabilitation of a centenary metallic bridge. *Engineering Structures, 44*, 281-290.

Rodrigues, C., Felix, C., Lage, A., & Figueiras, J. (2010). Development of a long-term monitoring system based on FBG sensors applied to concrete bridges. *Engineering Structures, 32*(8), 1993-2002.

Roveri, N., Carcaterra, A., & Sestieri, A. (2015). Real-time monitoring of railway infrastructures using fibre Bragg grating sensors. *Mechanical Systems and Signal Processing, 60–61*, 14-28.

Saleh, B. E., & Teich, M. C. (2014). Fiber optics. *Fundamentals of Photonics*, 272-309.

Sarasini, F., & Santulli, C. (2014). Non-destructive testing (NDT) of natural fibre composites: Acoustic emission technique. *Natural Fibre Composites*, 273-302.

Saxena, I. F., Guzman, N., & Pflanze, S. (2012). *Frequency response comparison of two FBG based hydrophones.*

Sboner, A., Karpikov, A., Chen, G., Smith, M., Dawn, M., Freeman, L. C., . . . Gerstein, M. B. (2009). Robust linear model normalization to reduce technical variability in functional protein microarrays. *Journal of proteome research, 8*(12), 5451-5464.

Seung, H. Y., Kim, K. B., Oh, H. G., & Kang, J. S. (2013). Non-contact detection of impact damage in CFRP composites using millimeter wave reflection and considering carbon fiber direction. *NDT & E International, 57*, 45-51.

Shehata, E., & Mufti, A. (2005). The "Manitoba" GFRP bridge deck system. *International Institute for FRP in Construction, 2*(1).

Shen, W., Yan, R., Xu, L., Tang, G., & Chen, X. (2015). Application study on FBG sensor applied to hull structural health monitoring. *Optik - International Journal for Light and Electron Optics, 126*(17), 1499-1504.

Si, L., & Baier, H. (2015). Real-time impact visualization inspection of aerospace composite structures with distributed sensors. *Sensors, 15*(7), 16536-16556.

Smith, S. (2016, 28 April 2016). Smart structures in the construction industry: A market and technology forecast - 2016 to 2025. Retrieved 8th Jan, 2017, from http://www.prnewswire.com/news-releases/smart-structures-in-the-construction-industry-a-market-and-technology-forecast--2016-to-2025-300259621.html

Stephens, R., Plew, R., & Jones, A. D. (2008). *Sams teach yourself SQL in 24 hours*: Pearson Education.

Sun, H. M., Jia, R. S., Du, Q. Q., & Fu, Y. (2016). Cross-correlation analysis and time delay estimation of a homologous micro-seismic signal based on the Hilbert-Huang transform. *Computers & Geosciences, 91*, 98-104.

Takashima, S., Asanuma, H., & Niitsuma, H. (2004). A water flowmeter using dual fiber Bragg grating sensors and cross-correlation technique. *Sensors and Actuators A: Physical, 116*(1), 66-74.

Tan, K. T., Watanabe, N., & Iwahori, Y. (2011). X-ray radiography and micro-computed tomography examination of damage characteristics in stitched composites subjected to impact loading. *Composites Part B: Engineering, 42*(4), 874-884.

Truong, B. T., Larbi, A. S., & Limam, A. (2016). Numerical modelling of reinforced concrete beams repaired by TRC composites. *Composite Structures, 152*, 779-790.

Tsuda, H. (2005). Ultrasound and damage detection in CFRP using fiber Bragg grating sensors. *Composites Science and Technology, 66*(5), 676-683.

Uno, N., & Kitayama, N. (2003). Design, fabrication and erection of the pedestrian bridge in the road-park of Ikei-Tairagawa in Okinawa. *IHI Engineering Review, 36*(2), 35-39.

Vignesh, K. S., Praveen, K. A., & Prabhu, N. (2012). Emerging trends of hybridized composites. *International Journal of Engineering & Science Research, 2*(12).

Vinson, J. R., & Sierakowski, R. L. (2012). *The behavior of structures composed of composite materials* (Vol. 5): Springer Science & Business Media.

Walker, W. F., & Trahey, G. E. (1995). A fundamental limit on delay estimation using partially correlated speckle signals. *IEEE Transactions on Ultrasonics, Ferroelectrics, and Frequency Control, 42*(2), 301-308.

Wang, L., & Wei, Y. (2016). Revised normalized difference nitrogen index (NDNI) for estimating canopy nitrogen concentration in wetlands. *Optik - International Journal for Light and Electron Optics, 127*(19), 7676-7688.

Webb, D. J., Surowiec, J., Sweeney, M., Jackson, D. A., Gavrilov, L. R., Hand, J. W., . . . Bennion, I. (1996). *Miniature fiber optic ultrasonic probe.* Paper presented at the SPIE's 1996 International Symposium on Optical Science, Engineering, and Instrumentation.

Wenzhu, H., Zhen, T., Zhang, W., Zhang, F., & Li, F. (2015). A high resolution demodulation algorithm for FBG-FP static strain sensors based on the Hilbert transform and cross third order cumulant. *Sensors, 15*(5), 9928.

Wild, G., & Hinckley, S. (2010). *Optical fibre Bragg gratings for acoustic sensors.* Paper presented at the Proc. 20th International Congress on Acoustics.

Yang, N. (2011). Optical sensing changes rules for military structural measurements. *The Journal of Military Electronics & Computing*.

Yehia, S., Douba, A., Abdullahi, O., & Farrag, S. (2016). Mechanical and durability evaluation of fiber reinforced self compacting concrete. *Construction and Building Materials, 121*, 120-133.

Yin, G., Dai, Y., Karanja, J., & Dai, J. (2015). Optimization design for medium-high frequency FBG accelerometer with different eigenfrequency and sensitivity. *Sensors and Actuators A: Physical, 235*, 311-316.

Yuan, L. B., Zhou, L. M., & Wu, J. S. (2000). Fiber optic temperature sensor with duplex Michleson interferometric technique. *Sensors and Actuators A: Physical, 86*(1-2), 2-7.

Zawadzka, A. S. (2014). Active control of smart tensegrity structures. *2014, 60*(4), 18-18.

Zhang, J., & Zhao, H. (2009). *Matched FBG application research on dynamic sensing and demodulation.* Paper presented at the Photonics and Optoelectronics, 2009. SOPO 2009. Symposium on.

Zhou, K., & Wu, Z. Y. (2017). Strain gauge placement optimization for structural performance assessment. *Engineering Structures, 141*(Supplement C), 184-197.

Zhou, W., Dong, X., Ni, K., Chan, C. C., & Shum, P. (2010). Temperature insensitive accelerometer based on a strain chirped FBG. *Sensors and Actuators A: Physical, 157*(1), 15-18.

Zhu, Y. K., Tian, G. Y., Lu, R. S., & Zhang, H. (2011). A review of optical NDT technologies. *Sensors (Basel, Switzerland), 11*(8), 7773-7798.

Zoltek. (2016). Carbon Fibre : How it is made? (Vol. 2016).

Zou, H., Liang, D., & Zeng, J. (2012). Dynamic strain measurement using two wavelength matched fiber Bragg grating sensors interrogated by a cascaded long period fiber grating. *Optics and Lasers in Engineering, 50*(2), 199-203.
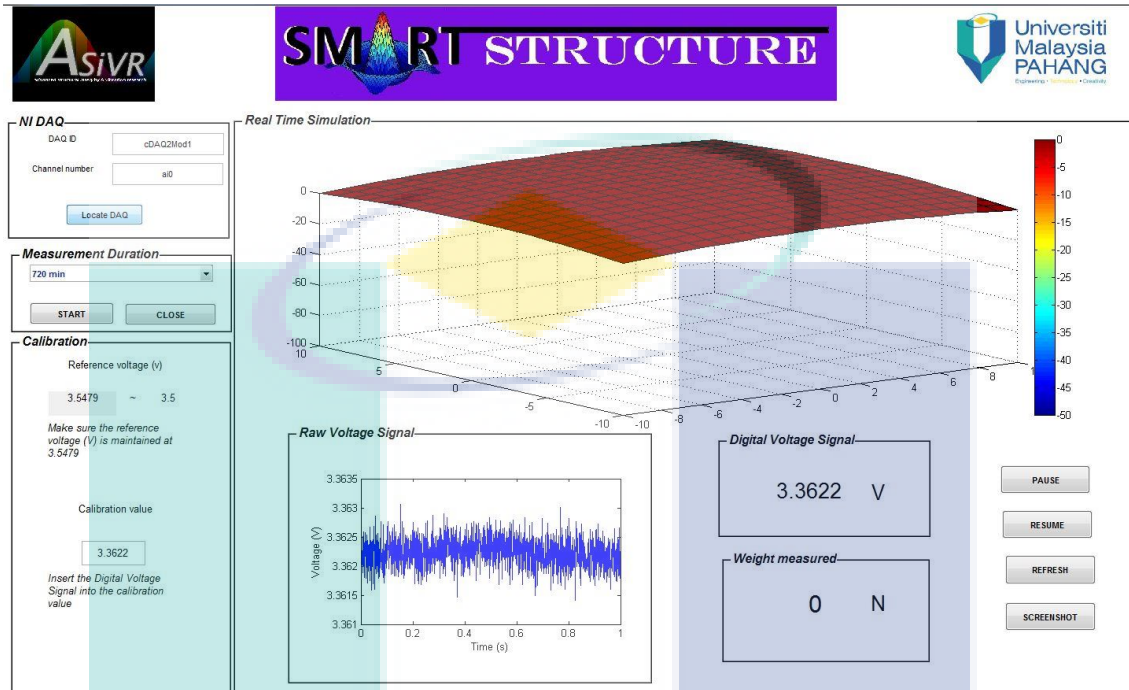
```
function varargout =
SmartStructure(varargin)
% SMARTSTRUCTURE MATLAB code for
SmartStructure.fig
%      SMARTSTRUCTURE, by itself,
creates a new SMARTSTRUCTURE or raises
the existing
%      singleton*.
%
%      H = SMARTSTRUCTURE returns the
handle to a new SMARTSTRUCTURE or the
handle to
%      the existing singleton*.
%
%
SMARTSTRUCTURE('CALLBACK',hObject,eventD
ata,handles,...) calls the local
%      function named CALLBACK in
SMARTSTRUCTURE.M with the given input
arguments.
%
%
SMARTSTRUCTURE('Property','Value',...)
creates a new SMARTSTRUCTURE or raises
the
%      existing singleton*.  Starting
from the left, property value pairs are
%      applied to the GUI before
SmartStructure_OpeningFcn gets called.
An
%      unrecognized property name or
invalid value makes property application
%      stop.  All inputs are passed to
SmartStructure_OpeningFcn via varargin.
%
%      *See GUI Options on GUIDE's Tools
menu.  Choose "GUI allows only one
%      instance to run (singleton)".
%
% See also: GUIDE, GUIDATA, GUIHANDLES
% Edit the above text to modify the
response to help SmartStructure
```

```
% Last Modified by GUIDE v2.5 30-May-
2016 14:32:43
% Begin initialization code - DO NOT
EDIT
gui_Singleton = 1;
gui_State = struct('gui_Name',
mfilename, ...
                   'gui_Singleton',
gui_Singleton, ...
                   'gui_OpeningFcn',
@SmartStructure_OpeningFcn, ...
                   'gui_OutputFcn',
@SmartStructure_OutputFcn, ...
                   'gui_LayoutFcn',  []
, ...
                   'gui_Callback',
[]);
if nargin && ischar(varargin{1})
   gui_State.gui_Callback =
str2func(varargin{1});
end
if nargout
   [varargout{1:nargout}] =
gui_mainfcn(gui_State, varargin{:});
else
   gui_mainfcn(gui_State, varargin{:});
end
% End initialization code - DO NOT EDIT
 % --- Executes just before
SmartStructure is made visible.
function
SmartStructure_OpeningFcn(hObject,
eventdata, handles, varargin)
% This function has no output args, see
OutputFcn.
% hObject    handle to figure
% eventdata  reserved - to be defined in
a future version of MATLAB
% handles    structure with handles and
user data (see GUIDATA)
% varargin   command line arguments to
SmartStructure (see VARARGIN)
```

```matlab
% Choose default command line output for
SmartStructure
handles.output = hObject;
% Update handles structure
guidata(hObject, handles);
% UIWAIT makes SmartStructure wait for
user response (see UIRESUME)
% uiwait(handles.figure1);
ASIVR=imread('logoASIVR.jpg');
handles.ASIVR=ASIVR;
axes(handles.logoASIVR);
imshow(ASIVR);
UMP=imread('UMP.jpeg');
handles.UMP=UMP;
axes(handles.logoUMP);
imshow(UMP);
ProgLogo=imread('SmartStrucLogo.jpg');
handles.ProgLogo=ProgLogo;
axes(handles.logoProg);
imshow(ProgLogo);
% --- Outputs from this function are
returned to the command line.
function varargout =
SmartStructure_OutputFcn(hObject,
eventdata, handles)
% varargout  cell array for returning
output args (see VARARGOUT);
% hObject    handle to figure
% eventdata  reserved - to be defined in
a future version of MATLAB
% handles    structure with handles and
user data (see GUIDATA)
% Get default command line output from
handles structure
varargout{1} = handles.output;
% --- Executes on selection change in
MeasurementDuration.
function
MeasurementDuration_Callback(hObject,
eventdata, handles)
% hObject    handle to
MeasurementDuration (see GCBO)
% eventdata  reserved - to be defined in
a future version of MATLAB
% handles    structure with handles and
user data (see GUIDATA)
% Hints: contents =
cellstr(get(hObject,'String')) returns
MeasurementDuration contents as cell
array
%        contents{get(hObject,'Value')}
returns selected item from
MeasurementDuration
str=get(hObject,'String');
val=get(hObject,'Value');
%Set current data to selected data set
switch str{val}
    case '15 min'
        handles.iterationNum=900;
    case '30 min'
        handles.iterationNum=1800;
    case '60 min'
        handles.iterationNum=3600;
    case '720 min'
        handles.iterationNum=43200;
end
guidata(hObject,handles);
% --- Executes during object creation,
after setting all properties.
function
MeasurementDuration_CreateFcn(hObject,
eventdata, handles)
% hObject    handle to
MeasurementDuration (see GCBO)
% eventdata  reserved - to be defined in
a future version of MATLAB

% handles    empty - handles not created
until after all CreateFcns called
% Hint: popupmenu controls usually have
a white background on Windows.
%       See ISPC and COMPUTER.
if ispc &&
isequal(get(hObject,'BackgroundColor'),
get(0,'defaultUicontrolBackgroundColor')
)

set(hObject,'BackgroundColor','white');
end
function edit5_Callback(hObject,
eventdata, handles)
% hObject    handle to edit5 (see GCBO)
% eventdata  reserved - to be defined in
a future version of MATLAB
% handles    structure with handles and
user data (see GUIDATA)
% Hints: get(hObject,'String') returns
contents of edit5 as text
%
str2double(get(hObject,'String'))
returns contents of edit5 as a double
% --- Executes during object creation,
after setting all properties.
function edit5_CreateFcn(hObject,
eventdata, handles)
% hObject    handle to edit5 (see GCBO)
% eventdata  reserved - to be defined in
a future version of MATLAB
% handles    empty - handles not created
until after all CreateFcns called
% Hint: edit controls usually have a
white background on Windows.
%       See ISPC and COMPUTER.
if ispc &&
isequal(get(hObject,'BackgroundColor'),
get(0,'defaultUicontrolBackgroundColor')
)

set(hObject,'BackgroundColor','white');
end
function edit4_Callback(hObject,
eventdata, handles)
% hObject    handle to edit4 (see GCBO)
% eventdata  reserved - to be defined in
a future version of MATLAB
% handles    structure with handles and
user data (see GUIDATA)
% Hints: get(hObject,'String') returns
contents of edit4 as text
%
str2double(get(hObject,'String'))
returns contents of edit4 as a double
% --- Executes during object creation,
after setting all properties.
function edit4_CreateFcn(hObject,
eventdata, handles)
% hObject    handle to edit4 (see GCBO)
% eventdata  reserved - to be defined in
a future version of MATLAB
% handles    empty - handles not created
until after all CreateFcns called
% Hint: edit controls usually have a
white background on Windows.
%       See ISPC and COMPUTER.
if ispc &&
isequal(get(hObject,'BackgroundColor'),
get(0,'defaultUicontrolBackgroundColor')
)

set(hObject,'BackgroundColor','white');
end
% --- Executes on button press in
pushbutton3.
```

```matlab
function pushbutton3_Callback(hObject,
eventdata, handles)
% hObject    handle to pushbutton3 (see
GCBO)
% eventdata  reserved - to be defined in
a future version of MATLAB
% handles    structure with handles and
user data (see GUIDATA)
hdaq=daq.getDevices;
if~isempty(hdaq)
    msgbox(sprintf('%s Device
Located',hdaq.Description),'Modal')
    hdaq
    handles.hdaq = hdaq;
    set(handles.edit5,'string',hdaq.ID)
else
    errordlg('No DAQ Device Found.')
    set(handles.edit5,'string','No ID
Found')
end
guidata(hObject,handles)
function edit7_Callback(hObject,
eventdata, handles)
% hObject    handle to edit7 (see GCBO)
% eventdata  reserved - to be defined in
a future version of MATLAB
% handles    structure with handles and
user data (see GUIDATA)
% Hints: get(hObject,'String') returns
contents of edit7 as text
%
str2double(get(hObject,'String'))
returns contents of edit7 as a double
% --- Executes during object creation,
after setting all properties.
function edit7_CreateFcn(hObject,
eventdata, handles)
% hObject    handle to edit7 (see GCBO)
% eventdata  reserved - to be defined in
a future version of MATLAB
% handles    empty - handles not created
until after all CreateFcns called
% Hint: edit controls usually have a
white background on Windows.
%        See ISPC and COMPUTER.
if ispc &&
isequal(get(hObject,'BackgroundColor'),
get(0,'defaultUicontrolBackgroundColor')
)

set(hObject,'BackgroundColor','white');
end
% --- Executes on button press in
StartPushButton.
function
StartPushButton_Callback(hObject,
eventdata, handles)
% hObject    handle to StartPushButton
(see GCBO)
% eventdata  reserved - to be defined in
a future version of MATLAB
% handles    structure with handles and
user data (see GUIDATA)
n=handles.iterationNum;
ID=get(handles.edit5,'String');
Channel=get(handles.edit7,'String');
s=daq.createSession('ni');
s.addAnalogInputChannel(ID,Channel,'Volt
age');
%s.Channels(1).Sensitivity=0.09;
for i=1:1:n;
    [data,time]=s.startForeground;
    p=mean(data);

a=str2double(get(handles.edit4,'String')
);
    answer=a-3.5479;
    calibrate=p-answer;
    u=str2num(sprintf('%.4f',p));

i=str2num(sprintf('%.4f',calibrate));
    set(handles.text29,'String',i);

w=str2num(sprintf('%.1f',calibrate));
    l=(100*(w))-350;
    e=str2num(sprintf('%.1f',l));
    set(handles.text22,'String',e);
    axes(handles.axes4)
    [x,y]=meshgrid(-10:10,-10:10);
    r=sqrt(x.^2+y.^2);
    c=(w-3.55).*(r.^2-200);
    surf(x,y,c)
    colorbar;

set(handles.axes4,'Color','w','XColor','
k','YColor','k');
    axis([-10 10 -10 10 -100 0]);
    caxis([-50 0]);
    axes(handles.axes9)
    plot(time,data);
    xlabel(handles.axes9,'Time (s)');
    ylabel(handles.axes9,'Voltage (V)');
    %axis([0 1 3.5 4])
    set(handles.text12,'String',u);
    set(handles.text19,'String',w);
end
% --- Executes on button press in
ClosePushBtton.
function
ClosePushBtton_Callback(hObject,
eventdata, handles)
% hObject    handle to ClosePushBtton
(see GCBO)
% eventdata  reserved - to be defined in
a future version of MATLAB
% handles    structure with handles and
user data (see GUIDATA)
cl = questdlg('EXIT the program
?','EXIT',...
            'Yes','No','No');
switch cl
    case 'Yes'
        close();
        clear all;
        return;
    case 'No'
        quit cancel;
end
% -------------------------------------
----------------------------
function
uipushtool1_ClickedCallback(hObject,
eventdata, handles)
% hObject    handle to uipushtool1 (see
GCBO)
% eventdata  reserved - to be defined in
a future version of MATLAB
% handles    structure with handles and
user data (see GUIDATA)
screenshot = getframe(gcf);
[jpegfile, path2jpeg] =
uiputfile('.tif');
FileName = fullfile(path2jpeg,
jpegfile);
imwrite (screenshot.cdata, FileName,
'tif');
% -------------------------------------
----------------------------
function
uipushtool5_ClickedCallback(hObject,
eventdata, handles)
% hObject    handle to uipushtool5 (see
GCBO)
```

121

```
% eventdata  reserved - to be defined in
a future version of MATLAB
% handles    structure with handles and
user data (see GUIDATA)
uiwait(gcbf)
% ------------------------------------
------------------------------
function
uipushtool6_ClickedCallback(hObject,
eventdata, handles)
```

```
% hObject    handle to uipushtool6 (see
GCBO)
% eventdata  reserved - to be defined in
a future version of MATLAB
% handles    structure with handles and
user data (see GUIDATA)
uiresume (gcbf)
```

```
% eventdata  reserved - to be defined in
a future version of MATLAB
% handles    structure with handles and
user data (see GUIDATA)
uiwait(gcbf)
```

```
% hObject    handle to uipushtool6 (see
```

```
function varargout = untitled(varargin)
% UNTITLED MATLAB code for untitled.fig
%      UNTITLED, by itself, creates a
new UNTITLED or raises the existing
%      singleton*.
%
%      H = UNTITLED returns the handle
to a new UNTITLED or the handle to
%      the existing singleton*.
%
%
UNTITLED('CALLBACK',hObject,eventData,ha
ndles,...) calls the local
%      function named CALLBACK in
UNTITLED.M with the given input
arguments.
%
%      UNTITLED('Property','Value',...)
creates a new UNTITLED or raises the
%      existing singleton*.  Starting
from the left, property value pairs are
%      applied to the GUI before
untitled_OpeningFcn gets called.  An
%      unrecognized property name or
invalid value makes property application
%      stop.  All inputs are passed to
untitled_OpeningFcn via varargin.
%
%      *See GUI Options on GUIDE's Tools
menu.  Choose "GUI allows only one
%      instance to run (singleton)".
%
% See also: GUIDE, GUIDATA, GUIHANDLES
% Edit the above text to modify the
response to help untitled
% Last Modified by GUIDE v2.5 01-Jun-
2016 16:58:11
% Begin initialization code - DO NOT
EDIT
gui_Singleton = 1;
gui_State = struct('gui_Name',
mfilename, ...
                'gui_Singleton',
gui_Singleton, ...
                'gui_OpeningFcn',
@untitled_OpeningFcn, ...
                'gui_OutputFcn',
@untitled_OutputFcn, ...
                'gui_LayoutFcn',  []
, ...
                'gui_Callback',
[]);
if nargin && ischar(varargin{1})
    gui_State.gui_Callback =
str2func(varargin{1});
end
if nargout
    [varargout{1:nargout}] =
gui_mainfcn(gui_State, varargin{:});
else
    gui_mainfcn(gui_State, varargin{:});
end
% End initialization code - DO NOT EDIT
% --- Executes just before untitled is
made visible.
function untitled_OpeningFcn(hObject,
eventdata, handles, varargin)
% This function has no output args, see
OutputFcn.
% hObject    handle to figure
% eventdata  reserved - to be defined in
a future version of MATLAB
% handles    structure with handles and
user data (see GUIDATA)
% varargin   command line arguments to
untitled (see VARARGIN)
% Choose default command line output for
untitled
handles.output = hObject;
% Update handles structure
guidata(hObject, handles);
% UIWAIT makes untitled wait for user
response (see UIRESUME)
% uiwait(handles.figure1);
% --- Outputs from this function are
returned to the command line.
function varargout =
untitled_OutputFcn(hObject, eventdata,
handles)
% varargout  cell array for returning
output args (see VARARGOUT);
% hObject    handle to figure
```
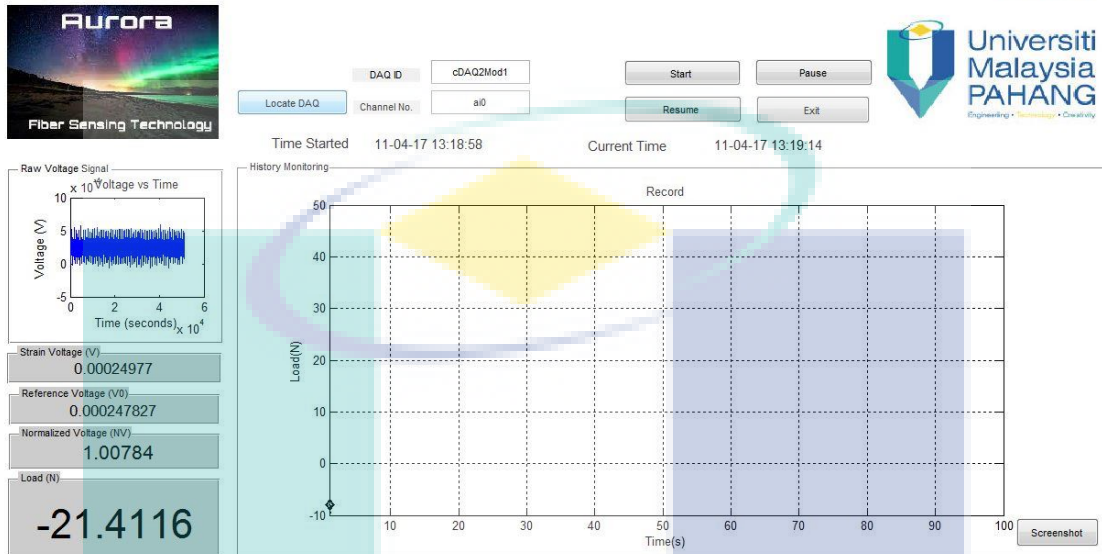
```matlab
% eventdata  reserved - to be defined in
a future version of MATLAB
% handles    structure with handles and
user data (see GUIDATA)
% Get default command line output from
handles structure
varargout{1} = handles.output;
axes(handles.axes1);
imshow('Aurora.jpg');
axes(handles.axes4);
imshow('UMP.jpeg');
t=datestr(clock,'dd-mm-yy HH:MM:SS');
set(handles.text10,'String',t,'FontSize'
,11);
% creating the timer object, so that
live mode is possible
timer_obj = timer(...
    'StartFcn',
@user_timer_start, ...          %
start function
    'TimerFcn',
{@user_timer_update, hObject}, ...  %
timer function, has to specific the
handle to the GUI,
    'StopFcn',
@user_timer_stop, ...            %
stop function
    'ErrorFcn',        @user_timer_err,
...              % error function
    'ExecutionMode',    'fixedRate', ...
%
    'Period',          0.1, ...
% updates every xx seconds
    'TasksToExecute',   inf, ...
    'BusyMode',        'drop');
% save the timer object as application
data
setappdata(hObject, 'timer_obj',
timer_obj);               % need to
save it because we need to stop and
delete it when quit
start(timer_obj);
% UIWAIT makes myClock wait for user
response (see UIRESUME)
% uiwait(handles.figure1);
% --- Outputs from this function are
returned to the command line.
function varargout =
myClock_OutputFcn(hObject, eventdata,
handles)
% varargout  cell array for returning
output args (see VARARGOUT);
% hObject    handle to figure
% eventdata  reserved - to be defined in
a future version of MATLAB
% handles    structure with handles and
user data (see GUIDATA)
% Get default command line output from
handles structure
varargout{1} = handles.output;
function user_timer_update(src,evt,
fig_handle)
handles = guihandles(fig_handle);
set(handles.text11, 'string',
datestr(now, 'dd-mm-yy
HH:MM:SS'),'FontSize',11);
function user_timer_start(src, evt)
disp('Timer started!');
function user_timer_stop(src, evt)
disp('Timer stop');
function user_timer_err(src, evt)
disp('Timer error');
% --- Executes when user attempts to
close figure1.
function
figure1_CloseRequestFcn(hObject,
eventdata, handles)

% hObject    handle to figure1 (see
GCBO)
% eventdata  reserved - to be defined in
a future version of MATLAB
% handles    structure with handles and
user data (see GUIDATA)
% Hint: delete(hObject) closes the
figure
stop(getappdata(hObject, 'timer_obj'));
delete(getappdata(hObject,
'timer_obj'));
delete(hObject);
% --- Executes on button press in
pushbutton2.
function pushbutton2_Callback(hObject,
eventdata, handles)
% hObject    handon2 (see GCBO)
% eventdata  reserved - to be defined in
a future verle to pushbuttsion of MATLAB
% handles    structure with handles and
user data (see GUIDATA)
ID=get(handles.edit2,'String');
Channel=get(handles.edit3,'String');
s=daq.createSession('ni');
s.Rate=256000;
s.addAnalogInputChannel(ID,Channel,'Volt
age');
k=0;
i=1;
n=0;
while k<100
    [data,time]=s.startForeground;
    axes(handles.axes5);
    plot(data);
        set(get(handles.axes5,
'XLabel'), 'String', 'Time (seconds)');
        set(get(handles.axes5,
'YLabel'), 'String', 'Voltage (V)');
        set(get(handles.axes5, 'Title'),
'String', 'Voltage vs Time');
        p=mean(data);
set(handles.text12,'String',p,'FontSize'
,13);
        if k<1;
set(handles.text19,'string',p,'FontSize'
,13);
        end
a=str2double(get(handles.text19,'String'
));
        k=p/a;
set(handles.text18,'String',k,'FontSize'
,16);
        y=((k-0.9954)/-0.0581)*100% -
1.325;
set(handles.text13,'String',y,'FontSize'
,33);
        if(n <=100)
        b(i)=y ;
        i=i+1;
        set(gcf,'color','white');
        drawnow;
        axes(handles.axes8);
        plot(b,'-.dk','linewidth',1.8),
axis([1 100 -100 300])
        grid on;
        title('Record')
        xlabel('Time(s)');
        ylabel('Load(N)');
        n = n + 1;
        pause(1.0);
        end
        %filename = 'testdata.xlsx';
```
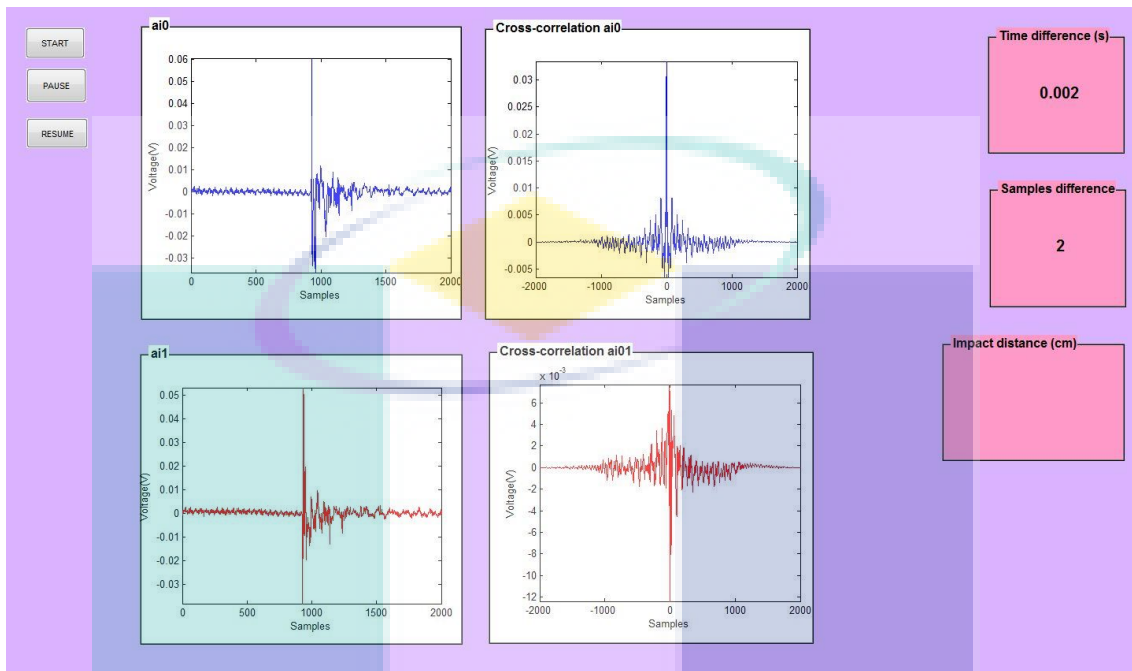
```matlab
        %A = [y];
        %xlswrite(filename,A)
        k=k+1;
end
% --- Executes on button press in
pushbutton3.
function pushbutton3_Callback(hObject,
eventdata, handles)
% hObject    handle to pushbutton3 (see
GCBO)
% eventdata  reserved - to be defined in
a future version of MATLAB
% handles    structure with handles and
user data (see GUIDATA)
cl = questdlg('Do you want to
EXIT?','EXIT',...
           'Yes','No','No');
switch cl
    case 'Yes'
        close();
        clear all;
        return;
    case 'No'
        quit cancel;
end
% --- Executes on button press in
pushbutton4.
function pushbutton4_Callback(hObject,
eventdata, handles)
% hObject    handle to pushbutton4 (see
GCBO)
% eventdata  reserved - to be defined in
a future version of MATLAB
% handles    structure with handles and
user data (see GUIDATA)
hdaq=daq.getDevices;
if~isempty(hdaq)
    msgbox(sprintf('%s Device
Located',hdaq.Description),'Modal')
    hdaq
    handles.hdaq = hdaq;

    set(handles.edit2,'string',hdaq.ID)
else
    errordlg('No DAQ Device Found.')
    set(handles.edit2,'string','No
Device Found')
end
guidata(hObject,handles)
function edit2_Callback(hObject,
eventdata, handles)
% hObject    handle to edit2 (see GCBO)
% eventdata  reserved - to be defined in
a future version of MATLAB
% handles    structure with handles and
user data (see GUIDATA)
% Hints: get(hObject,'String') returns
contents of edit2 as text
%
str2double(get(hObject,'String'))
returns contents of edit2 as a double
% --- Executes during object creation,
after setting all properties.
function edit2_CreateFcn(hObject,
eventdata, handles)
% hObject    handle to edit2 (see GCBO)
% eventdata  reserved - to be defined in
a future version of MATLAB
% handles    empty - handles not created
until after all CreateFcns called
% Hint: edit controls usually have a
white background on Windows.
%       See ISPC and COMPUTER.
if ispc &&
isequal(get(hObject,'BackgroundColor'),
get(0,'defaultUicontrolBackgroundColor')
)
set(hObject,'BackgroundColor','white');
end
function edit3_Callback(hObject,
eventdata, handles)
% hObject    handle to edit3 (see GCBO)
% eventdata  reserved - to be defined in
a future version of MATLAB
% handles    structure with handles and
user data (see GUIDATA)
% Hints: get(hObject,'String') returns
contents of edit3 as text
%
str2double(get(hObject,'String'))
returns contents of edit3 as a double
% --- Executes during object creation,
after setting all properties.
function edit3_CreateFcn(hObject,
eventdata, handles)
% hObject    handle to edit3 (see GCBO)
% eventdata  reserved - to be defined in
a future version of MATLAB
% handles    empty - handles not created
until after all CreateFcns called
% Hint: edit controls usually have a
white background on Windows.
%       See ISPC and COMPUTER.
if ispc &&
isequal(get(hObject,'BackgroundColor'),
get(0,'defaultUicontrolBackgroundColor')
)
set(hObject,'BackgroundColor','white');
end
% --- Executes on button press in
pushbutton5.
function pushbutton5_Callback(hObject,
eventdata, handles)
% hObject    handle to pushbutton5 (see
GCBO)
% eventdata  reserved - to be defined in
a future version of MATLAB
% handles    structure with handles and
user data (see GUIDATA)
screenshot = getframe(gcf);
[jpegfile, path2jpeg] =
uiputfile('.jpeg');
FileName = fullfile(path2jpeg,
jpegfile);
imwrite (screenshot.cdata, FileName,
'jpg');
% --- Executes on button press in
pushbutton6.
function pushbutton6_Callback(hObject,
eventdata, handles)
% hObject    handle to pushbutton6 (see
GCBO)
% eventdata  reserved - to be defined in
a future version of MATLAB
% handles    structure with handles and
user data (see GUIDATA)
uiresume(gcbf)
% --- Executes on button press in
pushbutton7.
function pushbutton7_Callback(hObject,
eventdata, handles)
% hObject    handle to pushbutton7 (see
GCBO)
% eventdata  reserved - to be defined in
a future version of MATLAB
% handles    structure with handles and
user data (see GUIDATA)
uiwait(gcbf)
```

```
function varargout = untitled(varargin)
% UNTITLED MATLAB code for untitled.fig
%      UNTITLED, by itself, creates a
new UNTITLED or raises the existing
%      singleton*.
%
%      H = UNTITLED returns the handle
to a new UNTITLED or the handle to
%      the existing singleton*.
%
%
UNTITLED('CALLBACK',hObject,eventData,ha
ndles,...) calls the local
%      function named CALLBACK in
UNTITLED.M with the given input
arguments.
%
%      UNTITLED('Property','Value',...)
creates a new UNTITLED or raises the
%      existing singleton*.  Starting
from the left, property value pairs are
%      applied to the GUI before
untitled_OpeningFcn gets called.  An
%      unrecognized property name or
invalid value makes property application
%      stop.  All inputs are passed to
untitled_OpeningFcn via varargin.
%
%      *See GUI Options on GUIDE's Tools
menu.  Choose "GUI allows only one
%      instance to run (singleton)".
%
% See also: GUIDE, GUIDATA, GUIHANDLES
% Edit the above text to modify the
response to help untitled
% Last Modified by GUIDE v2.5 01-Aug-
2016 16:13:40
% Begin initialization code - DO NOT
EDIT
gui_Singleton = 1;
gui_State = struct('gui_Name',
mfilename, ...
                   'gui_Singleton',
gui_Singleton, ...
                   'gui_OpeningFcn',
@untitled_OpeningFcn, ...
                   'gui_OutputFcn',
@untitled_OutputFcn, ...
                   'gui_LayoutFcn',  []
, ...
                   'gui_Callback',
[]);
if nargin && ischar(varargin{1})
    gui_State.gui_Callback =
str2func(varargin{1});
end
if nargout
    [varargout{1:nargout}] =
gui_mainfcn(gui_State, varargin{:});
else
    gui_mainfcn(gui_State, varargin{:});
end
% End initialization code - DO NOT EDIT
% --- Executes just before untitled is
made visible.
function untitled_OpeningFcn(hObject,
eventdata, handles, varargin)
% This function has no output args, see
OutputFcn.
% hObject    handle to figure
% eventdata  reserved - to be defined in
a future version of MATLAB
% handles    structure with handles and
user data (see GUIDATA)
% varargin   command line arguments to
untitled (see VARARGIN)
% Choose default command line output for
untitled
handles.output = hObject;
% Update handles structure
guidata(hObject, handles);
% UIWAIT makes untitled wait for user
response (see UIRESUME)
% uiwait(handles.figure1);
```

```matlab
% --- Outputs from this function are
returned to the command line.
function varargout =
untitled_OutputFcn(hObject, eventdata,
handles)
% varargout  cell array for returning
output args (see VARARGOUT);
% hObject    handle to figure
% eventdata  reserved - to be defined in
a future version of MATLAB
% handles    structure with handles and
user data (see GUIDATA)
% Get default command line output from
handles structure
varargout{1} = handles.output;
% --- Executes on button press in
pushbutton1.
function pushbutton1_Callback(hObject,
eventdata, handles)
% hObject    handle to pushbutton1 (see
GCBO)
% eventdata  reserved - to be defined in
a future version of MATLAB
% handles    structure with handles and
user data (see GUIDATA)
s = daq.createSession('ni');
s.Rate=2000;
ch =
addAnalogInputChannel(s,'cDAQ2Mod1',0,'V
oltage');
c=addAnalogInputChannel(s,'cDAQ2Mod1',1,
'Voltage');
ch.Coupling = 'AC';
c.Coupling='AC';
for n=1:10000000;
    [data,time]=s.startForeground;
    axes(handles.axes1);
    plot((data(:,1)),'Color','b');
    xlabel('Samples');
    ylabel('Voltage(V)');
    axis([0 2000 -inf inf])
    axes(handles.axes2);
    plot((data(:,2)),'Color','r');
    xlabel('Samples');
    ylabel('Voltage(V)');
    axis([0 2000 -inf inf])
    Fs=1000;
```

```matlab
    [acor,lag] = xcorr(data);
    [~,I] = max(abs(acor));
    lagDiff = lag(I)
    timeDiff = lagDiff/Fs
    axes(handles.axes10);

plot((lag(1,:)),(acor(:,1)),'Color','b')
;
    xlabel('Samples');
    ylabel('Voltage(V)');
    axis([-2000 2000 -inf inf])
    axes(handles.axes12);

plot((lag(1,:)),(acor(:,2)),'Color','r')
;
    xlabel('Samples');
    ylabel('Voltage(V)');
    axis([-2000 2000 -inf inf])
set(handles.text3,'String',abs(timeDiff)
);
set(handles.text5,'String',abs(lagDiff))
;
save('test.mat')
end
% --- Executes on button press in
pushbutton3.
function pushbutton3_Callback(hObject,
eventdata, handles)
% hObject    handle to pushbutton3 (see
GCBO)
% eventdata  reserved - to be defined in
a future version of MATLAB
% handles    structure with handles and
user data (see GUIDATA)
uiwait(gcbf)
% --- Executes on button press in
pushbutton4.
function pushbutton4_Callback(hObject,
eventdata, handles)
% hObject    handle to pushbutton4 (see
GCBO)
% eventdata  reserved - to be defined in
a future version of MATLAB
% handles    structure with handles and
user data (see GUIDATA)
uiresume (gcbf)
```

127

```matlab
function varargout = untitled(varargin)
% UNTITLED MATLAB code for untitled.fig
%      UNTITLED, by itself, creates a
new UNTITLED or raises the existing
%      singleton*.
%
%      H = UNTITLED returns the handle
to a new UNTITLED or the handle to
%      the existing singleton*.
%
%
UNTITLED('CALLBACK',hObject,eventData,ha
ndles,...) calls the local
%      function named CALLBACK in
UNTITLED.M with the given input
arguments.
%
%      UNTITLED('Property','Value',...)
creates a new UNTITLED or raises the
%      existing singleton*.  Starting
from the left, property value pairs are
%      applied to the GUI before
untitled_OpeningFcn gets called.  An
%      unrecognized property name or
invalid value makes property application
%      stop.  All inputs are passed to
untitled_OpeningFcn via varargin.
%
%      *See GUI Options on GUIDE's Tools
menu.  Choose "GUI allows only one
%      instance to run (singleton)".
%
% See also: GUIDE, GUIDATA, GUIHANDLES
% Edit the above text to modify the
response to help untitled
% Last Modified by GUIDE v2.5 01-Aug-
2016 16:13:40
% Begin initialization code - DO NOT
EDIT
gui_Singleton = 1;
gui_State = struct('gui_Name',
mfilename, ...
                   'gui_Singleton',
gui_Singleton, ...
                   'gui_OpeningFcn',
@untitled_OpeningFcn, ...
                   'gui_OutputFcn',
@untitled_OutputFcn, ...
                   'gui_LayoutFcn',  []
, ...
                   'gui_Callback',
[]);
if nargin && ischar(varargin{1})
    gui_State.gui_Callback =
str2func(varargin{1});
end

if nargout
    [varargout{1:nargout}] =
gui_mainfcn(gui_State, varargin{:});
else
    gui_mainfcn(gui_State, varargin{:});
end
% End initialization code - DO NOT EDIT
% --- Executes just before untitled is
made visible.
function untitled_OpeningFcn(hObject,
eventdata, handles, varargin)
% This function has no output args, see
OutputFcn.
% hObject    handle to figure
% eventdata  reserved - to be defined in
a future version of MATLAB
% handles    structure with handles and
user data (see GUIDATA)
% varargin   command line arguments to
untitled (see VARARGIN)
% Choose default command line output for
untitled
handles.output = hObject;
% Update handles structure
guidata(hObject, handles);
% UIWAIT makes untitled wait for user
response (see UIRESUME)
% uiwait(handles.figure1);
```

```matlab
% --- Outputs from this function are
returned to the command line.
function varargout =
untitled_OutputFcn(hObject, eventdata,
handles)
% varargout  cell array for returning
output args (see VARARGOUT);
% hObject    handle to figure
% eventdata  reserved - to be defined in
a future version of MATLAB
% handles    structure with handles and
user data (see GUIDATA)
% Get default command line output from
handles structure
varargout{1} = handles.output;
% --- Executes on button press in
pushbutton1.
function pushbutton1_Callback(hObject,
eventdata, handles)
% hObject    handle to pushbutton1 (see
GCBO)
% eventdata  reserved - to be defined in
a future version of MATLAB
% handles    structure with handles and
user data (see GUIDATA)
s = daq.createSession('ni');
s.Rate=10000;
ch =
addAnalogInputChannel(s,'cDAQ2Mod1',0,'V
oltage');
c=addAnalogInputChannel(s,'cDAQ2Mod1',1,
'Voltage');
ch.Coupling = 'AC';
c.Coupling='AC';
for n=1:10000000;
    [data,time]=s.startForeground;
    axes(handles.axes1);
    plot((data(:,1)),'Color','b');
    xlabel('Samples');
    ylabel('Voltage(V)');
    axis([0 10000 -inf inf])
    axes(handles.axes2);
    plot((data(:,2)),'Color','r');
    xlabel('Samples');
    ylabel('Voltage(V)');
    axis([0 10000 -inf inf])
    Fs=10000;
Y=fft((data(:,1)));
L=10000;
P2 = abs(Y/L);
P1 = P2(1:L/2+1);
P1(2:end-1) = 2*P1(2:end-1);
f = Fs*(0:(L/2))/L;
axes(handles.axes10);
plot(f,P1,'Color','b');
%axis([500 5000 -inf inf])
xlabel('f (Hz)');
ylabel('|X(f)|');
Y=fft((data(:,2)));
L=1500;
P2 = abs(Y/L);
P3 = P2(1:L/2+1);
P3(2:end-1) = 2*P3(2:end-1);
w = Fs*(0:(L/2))/L;
axes(handles.axes12);
plot(w,P3,'Color','r');
xlabel('f (Hz)');
ylabel('|X(f)|');
save('test.mat')
end
% --- Executes on button press in
pushbutton3.
function pushbutton3_Callback(hObject,
eventdata, handles)
% hObject    handle to pushbutton3 (see
GCBO)
% eventdata  reserved - to be defined in
a future version of MATLAB
% handles    structure with handles and
user data (see GUIDATA)
uiwait(gcbf)
% --- Executes on button press in
pushbutton4.
function pushbutton4_Callback(hObject,
eventdata, handles)
% hObject    handle to pushbutton4 (see
GCBO)
% eventdata  reserved - to be defined in
a future version of MATLAB
% handles    structure with handles and
user data (see GUIDATA)
uiresume (gcbf)
```

GANTT CHART

		YEAR 1												YEAR 2											
SEMESTER		1							2					3							4				
MONTH		FEB	MAC	APR	MAY	JUN	JUL	AUG	SEP	OCT	NOV	DEC	JAN	FEB	MAC	APR	MAY	JUN	JUL	AUG	SEP	OCT	NOV	DEC	JAN
Literature review																									
Materials and consumable purchase																									
Specimen fabrication and preparation																									
Specimen analysis																									
Algorithm development																									
Graphic user interface (GUI) development																									
Experimentation																									
Data collection and analysis																									
Thesis writing																									
MILESTONES - TASK TO BE COMPLETED WITHIN 2 YEARS																									
Proposal defend																									
Draft thesis submission																									
Viva-voce presentation																									
Publications																									